Inaugural Dissertation zur Erlangung des
Doktorgrades der Naturwissenschaften
der Justus-Liebig Universität Gießen
(Fachbereich Physik)

SUPER-FRS. THE NEXT GENERATION EXOTIC NUCLEAR BEAM FACILITY AT GSI

vorgelegt von
Vladimir N. Chichkine
geboren in St.-Petersburg

Gießen, Juni 2003

Gutachter: Prof. Dr. Hans Geissel
Prof. Dr. Volker Metag

ZUSAMMENFASSUNG

Energiereiche Strahlen exotischer Kerne oberhalb der Coulomb Barriere haben in der Kernphysik eine neue Dimension eröffnet. Deshalb gibt es weltweit große Anstrengungen, die sich auf den Aufbau von neuen leistungsfähigen Anlagen mit exotischen Kernstrahlen konzentrieren. Drastische Steigerung der Strahlintensitäten der exotischen Nuklide, um in unbekannte Bereiche der Nuklidkarte vordringen zu können und das Erreichen von höherer Präzision sind die wichtigsten Ziele dabei. Diesen Herausforderungen stellt sich die GSI mit ihrem internationalen Zukunftsprojekt, in dem der Super-FRS mit den Ionenspeicherringen wichtige Bestandteile sind.

Die ionenoptischen Berechnungen des neuen supraleitenden Fragmentseparators (Super-FRS) sind ein Hauptziel dieser Arbeit. Der Super-FRS zeichnet sich durch eine hohe Phasenraumakzeptanz von $\varepsilon_x = \varepsilon_y = 40\ \pi$ mm mrad und einer Impulsakzeptanz von $dp/p = \pm 2.5\%$ aus. Damit ist es möglich, neben der Fragmentation von Projektilstrahlen insbesondere auch die Spaltung von Uranstrahlen als Produktionsmethode zur Erzeugung extrem neutronenreicher Nuklide einzusetzen. Die Transmission von Projektilfragmenten durch den Super-FRS ist nahe 100% und die von Uran-Spaltfragmenten 40-50%. Diese Transmission für Spaltfragmente ist mehr als eine Größenordnung höher als sie jetzt am FRS für leichte Kerne (^{78}Ni) erreicht wurde. Die maximale magnetische Steifigkeit des Super-FRS beträgt 20 Tm, dies entspricht einem U^{92+} Strahl mit einer Energie von 1.5 A GeV. Die maximale Strahlenergie ist so gewählt, um auch die schwersten Fragmente völlig ionisiert nach dem Produktionstarget analysieren zu können. Die ionenoptische Impulsauflösung an der dispersiven Mittelebene des Super-FRS beträgt 1500 bei einem Strahlfleck von 1 mm und der oben angegebenen Phasenraumakzeptanz. Dies garantiert die geforderte Isotopenreinheit in der Separation und ermöglicht auch den Betrieb des Super-FRS als hochauflösendes Spektrometer.

Das Separationsprinzip des Super-FRS beruht auf der sogenannten $B\rho-\Delta E-B\rho$ Methode. Hierbei wird eine zweifache Analyse der Ionen nach ihrer magnetischen Steifigkeit mit dem Energieverlust in einem speziell geformten Materieblock (Energy Degrader) kombiniert, der zwischen den beiden Analysestufen in einer dispersiven Fokalebene angeordnet ist. Beim Super-FRS sind zwei solche Stufen hintereinander geschaltet, wobei jede Stufe mit einem Energy Degrader ausgestattet ist. Diese Kaskadenanordnung erlaubt den Untergrund effizient zu unterdrücken und isotopenreine Nuklidstrahlen bereitzustellen. Beide Separatorstufen (Pre- and Main Separator) sind im Standardbetrieb achromatische Systeme. Dies erlaubt eine Ortsabbildung des Fragmentstrahles vom Target zum Endfokus, die unabhängig von der großen Impulsverteilung der Fragmente ist. In einem solchen System kann die beste räumliche Trennung der Isotope erreicht werden.

Aufgrund der hohen Winkel- und Impulsakzeptanz des Separators spielt die Korrektur der Abbildungsfehler des ionenoptischen Systems eine große Rolle. Der Super-FRS ist deshalb nicht nur mit Hexapol-Korrekturelementen ausgestattet, wie dies beim FRS der Fall ist, sondern zusätzlich auch mit Oktupol-Korrekturelementen. Die Korrekturmagnete können als Oberflächenspulen ausgeführt werden, die den Quadrupolfeldern überlagert werden.

Ähnlich wie am FRS erprobt, wird der Super-FRS mit drei Zweigen die verschiedenen Experimentanordnungen versorgen. Die ionenoptischen Berechnungen dieser Experimentierzweige unter der Einbeziehung der Targetregion waren ein weiterer Schwerpunkt dieser Arbeit. Die Strahlfleckgröße bestimmt direkt die erreichbare Isotopentrennung und auch die Transmission. Es ist vorgesehen das Fokussierungssystem, bestehend aus supraleitenden Linsen, so flexibel zu gestalten, dass es sowohl mit dem neuen Beschleuniger als auch dem jetzigen SIS18 Beschleuniger bedient werden kann.

Die Gesamtkonzeption des Super-FRS basiert auf den Erfahrungen aus dem Experimentbetrieb mit dem FRS. Vorteilhaft für einige notwendige Neuentwicklungen am Super-FRS ist, dass diese direkt am jetzigen FRS-System schon erprobt werden können. Verschiedene neue Betriebsarten und die dabei auftretenden Bildfehler wurden in dedizierten Experimenten im Rahmen dieser Arbeit unter-

sucht. Besonders interessant war der Einsatz von gepulsten kurzbrennweitigen Linsen, die zum Aufbau eines Strahlkondensor Systems verwendet werden können.

Contents

Chapter 1

Introduction

The success of the present exotic nuclear beam facilities has motivated the development of new projects and plans for next generation facilities worldwide. Of special interest are facilities which can provide beams of rare isotopes with kinematic energies beyond the Coulomb barrier [1], [2]. This allows carrying out nuclear reaction experiments with exotic nuclei that have been possible only with stable nuclei in the past.

The new accelerator facility planned at GSI [3] will provide primary beams of all stable isotopes from hydrogen to uranium at intensities that are a factor of 100 to 1000 higher than presently available at GSI. It consists of a 100/200 Tm double-ring synchrotron (SIS100/200) and a system of associated storage rings for beam accumulation, cooling, phase-space optimization as well as various other experimental areas (Fig. 1.1).

The new SUPERconducting FRagment Separator (Super-FRS) will accept a much larger phase space compared with the present FRagment Separator (FRS). Together with the increased primary beam intensity, this will result in an overall gain of secondary beam intensities by a factor up to 10000. The maximum beam energies of radioactive species will be unparalleled by any other existing or planned facility. Altogether, this will allow sensitive experiments with secondary beam species far away from stability. The expected production rates of these nuclei are given in Fig. 1.2.

In pioneering experiments using the FRS it became clear that fission of uranium is an indispensable source of very neutron-rich medium mass nuclei [5]. Thus, a pertinent feature of the Super-FRS will be the ability to collect projectile-fission fragments with the same efficiency as achieved at present for projectile-fragmentation products.

The Super-FRS will serve three different experimental areas dedicated to specific experimental requirements:

1) a High-Energy Branch to perform high-energy reaction studies;

2) a Ring Branch for high precision mass, lifetime and scattering experiments

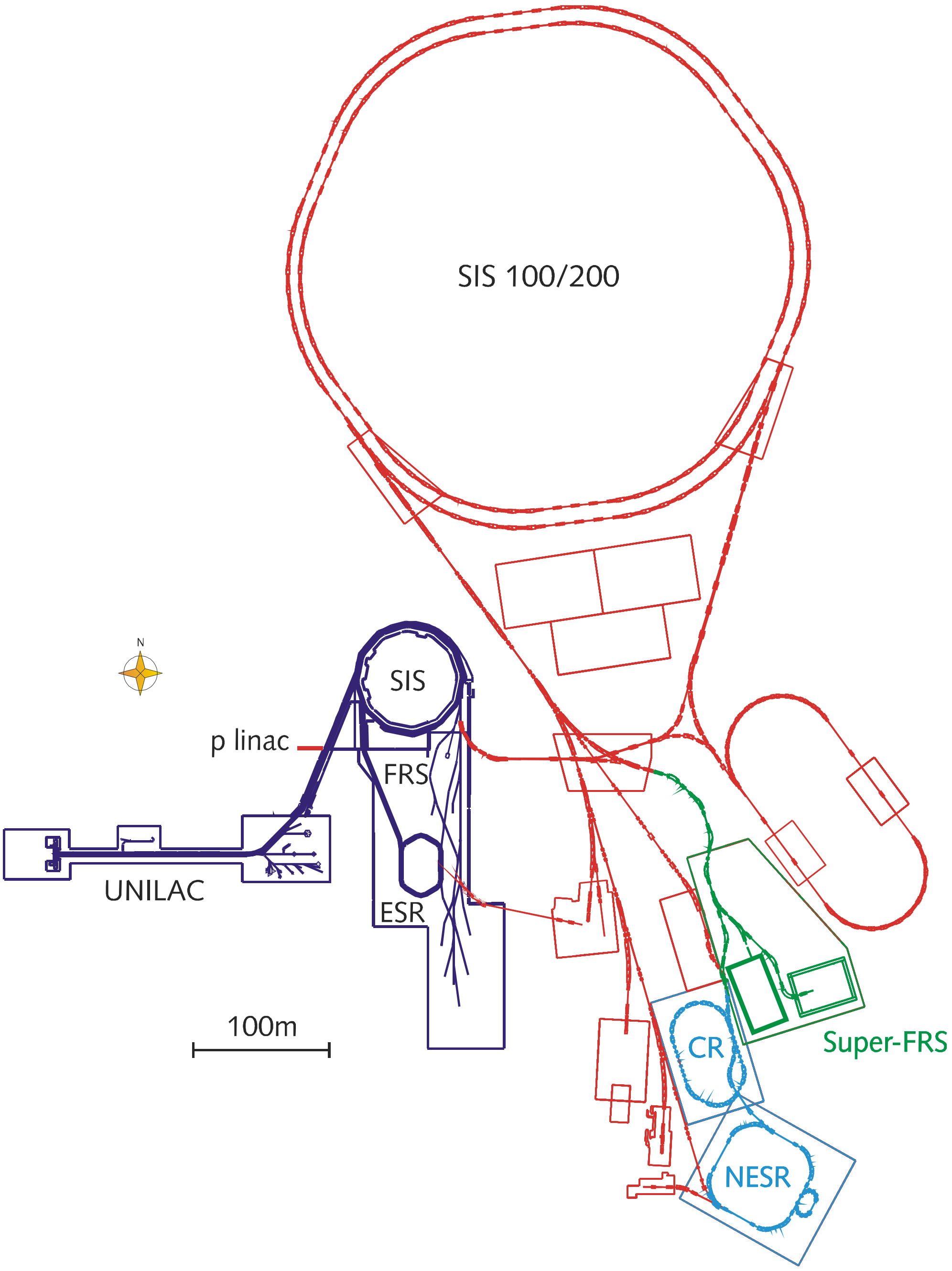

Figure 1.1: The existing GSI facility (dark blue) with the linear accelerator UNILAC, the heavy-ion synchrotron SIS18, the fragment separator FRS and the experimental storage ring ESR; and the new project (red) with the double-ring synchrotron SIS100/200, the super-conducting fragment separator Super-FRS, the collector ring CR, the new experimental storage ring NESR and several experimental stations [3]. The present UNILAC/SIS18 complex serves as the injector for the new double-ring synchrotron.

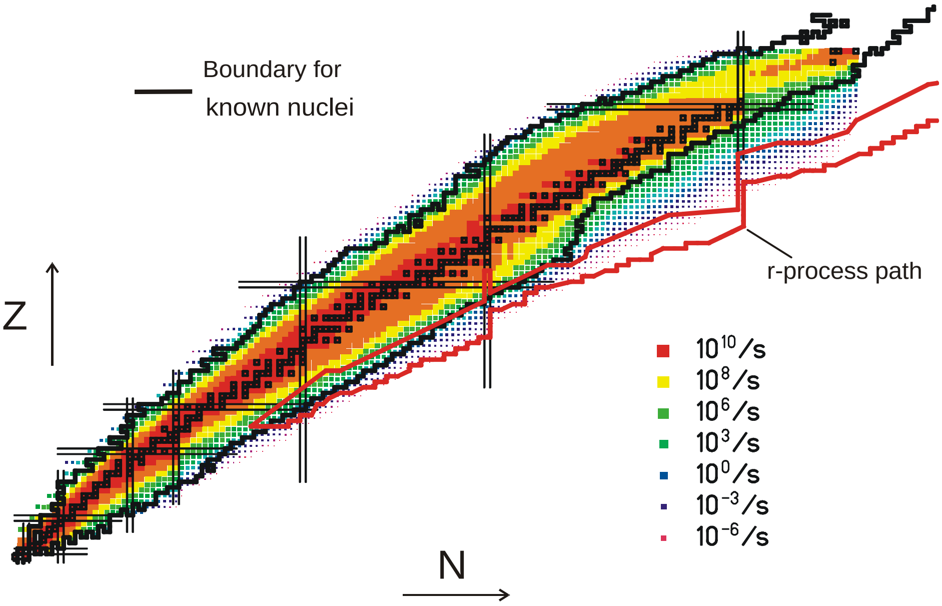

Figure 1.2: Predicted production rates (for nuclei with half-lifes larger than 100 ns) at the proposed new GSI facility [3]. Stable nuclei (black symbols), closed shells (double lines), and the limits of known nuclei are indicated. At the new facility, hitherto unexplored parts of the r-process path (red lines indicate the boarder) will become accessible, in particular around the closed neutron shells N = 82, N = 126 and even beyond.

with stored and cooled ions;

3) a Low-Energy Branch to perform implantation and spectroscopy experiments. The latter one incorporates an Energy Buncher stage, which allows efficiently to stop beams in solid or gaseous materials with strongly compressed range distribution.

This work is dedicated to the design and the characterization of the proposed Super-FRS. The first part gives an introduction to the ion optics as far as it is related to fragment separator problems. Also the interaction of ion beams with matter and the production mechanism of the exotic nuclei will be described. The second part of the work describes in details the design of the Super-FRS together with the transport beam line SIS100/200 to the Super-FRS target, which provides the operating conditions for the new separator. Also the influence of higher-order aberrations and the way to correct them will be discussed. In many aspects the existing FRS can be used as a test facility for the Super-FRS and gives the opportunity to investigate basic concepts experimentally. Several experiments at the FRS were done in the framework of this PhD and the results are presented at suitable positions of the work.

Chapter 2

1^{st} order ion optics of fragment separators

2.1 Motion of charged particles in electromagnetic fields

The motion of charged particles in electrostatic and magnetic fields is described by the Lorentz equation

$$\vec{F} = \frac{d\vec{p}}{dt} = Qe(\vec{E} + \vec{v} \times \vec{B}); \tag{2.1}$$

where Qe is the charge, $\vec{p}$ is the momentum and $\vec{v}$ is the velocity of the particle. $\vec{E}$ and $\vec{B}$ are the electrostatic and magnetic field flux densities respectively.

One of alternative descriptions of the motion of charged particles in electromagnetic fields uses Hamilton's variational principle. It states that the trajectory along which a particle moves from point P_1 to point P_2 is distinguished from all other possible paths by the fact that the line integral

$$S = \int L(x, y, z, \frac{dx}{dt}, \frac{dy}{dt}, \frac{dz}{dt})dt = \int L(\vec{r}, \vec{v}, t)dt \tag{2.2}$$

must be minimized. Here S - is the action and L is the so-called Lagrange function, which must be chosen such, that the final result is identical to Eq.(2.1) and it is a function of the particle position $\vec{r}$ and velocity $\vec{v}$ at the time t.

For an infinitely small variation in the flight path,

$$r \rightarrow r + \Delta r; \qquad v \rightarrow v + \Delta v \tag{2.3}$$

the variation δW of Eq. (2.2) is

$$\delta S = \delta \int_{t_1}^{t_2} L dt = \int_{t_1}^{t_2} \left(\frac{\partial L}{\partial \vec{r}} \delta \vec{r} + \frac{\partial L}{\partial \vec{v}} \delta \vec{v} \right) dt. \tag{2.4}$$

Let us postulate now that $\delta S = 0$ then the real trajectory is that one for which S takes up a minimal value.

The simplest procedure to obtain L is to assume [6]

$$L = m_0 c^2 \left[1 - \sqrt{1 - (v/c)^2} \right] - (Qe)V + (Qe)\vec{v}\,\vec{A} \tag{2.5}$$

where V is the electrostatic potential and $\vec{A}$ the magnetic vector potential at the point of interest, m_0 - is the relativistic mass of the particle which is equal to γm_{00}, where the m_{00} is the rest mass of the particle. From this vector potential the magnetic flux density is calculated as

$$\vec{B} = \vec{\nabla} \times \vec{A};$$

which represents the magnetic field strength by the relation $\vec{H} = \vec{B}/\mu\mu_0$. The corresponding electrostatic field strength $\vec{E}$ is calculated from the electrostatic potential V and the variation of the magnetic vector $\vec{A}$ as

$$\vec{E} = -\mathrm{grad}V - d\vec{A}/dt;$$

according to Maxwell's equations. Introducing the assumed Lagrange function L of Eq. (2.5) into Eq. (2.4), we find

$$-(Qe)\mathrm{grad}V + (Qe)\vec{v} \cup [\vec{\nabla} \times \vec{A}] = \frac{d}{dt}\left(\frac{m_0 \vec{v}}{\sqrt{1 - (v/c)^2}} + (Qe)\vec{A} \right); \tag{2.6}$$

which is identical to Eq. (2.1), so that it may be accepted that L of Eq. (2.5) is correct.

2.2 Method of 1^{st} order transfer matrices

For geometric light optics it has been customary since the time of Newton to use a trigonometric formulation for all equations of motion. However, this method has been replaced in many cases by the use of transfer matrices ([6], [7]). For simple optical systems the use of transfer matrices has no particular advantage. For complex systems, on the other hand, it offers essential simplicity and clarity.

First it is necessary to introduce the coordinate system in which the particle motion will be described. In ion optics the motion of a particle is described in relative coordinates to a reference particle which defines the optical axis of motion.

In this sense the following six dimensional coordinate system is used here:

$$\begin{aligned} & x; \\ a = {} & p_x/p_z; \\ & y; \\ b = {} & p_y/p_z; \\ t = {} & l/v; \\ \delta = {} & \frac{B\rho - B_0\rho_0}{B_0\rho_0}; \end{aligned} \tag{2.7}$$

where x and y are deviations of the particle from the trajectory of the reference particle (optical axis); p_x, p_y and p_z are the momentum of the particle in the respective directions; a and b are the angles of inclination to the optical axis; t is the time of flight of the reference particle; l is the path length and v is the velocity of the particle. $B\rho$ and $B_0\rho_0$ are the magnetic rigidities of an arbitrary particle and the reference particle, respectively. Thus, a particle beam in any point may be described by the position vector

$$\vec{r} = (r_1; r_{2;}; r_3; r_4; r_5; r_6) = (x; a; y; b; t; \delta): \tag{2.8}$$

Along with the position vector, we introduce the profile plane. A profile plane is defined as a plane that is perpendicular to the optical axis, and positioned along the path of the reference particle. Thus, the transfer matrix brings a ray from the initial profile plane to the final as

$$\vec{r}^{\,(f)} = T\,\vec{r}^{\,(i)}: \tag{2.9}$$

The 6×6 transfer matrix, T, of a system consisting of focusing and dispersive elements has the general form: [7]

$$T = \begin{bmatrix} (x;x) & (x;a) & (x;y) & (x;b) & (x;t) & (x;\delta) \\ (a;x) & (a;a) & (a;y) & (a;b) & (a;t) & (a;\delta) \\ (y;x) & (y;a) & (y;y) & (y;b) & (y;t) & (y;\delta) \\ (b;x) & (b;a) & (b;y) & (b;b) & (b;t) & (b;\delta) \\ (t;x) & (t;a) & (t;y) & (t;b) & (t;t) & (t;\delta) \\ (\delta;x) & (\delta;a) & (\delta;y) & (\delta;b) & (\delta;t) & (\delta;\delta) \end{bmatrix} \tag{2.10}$$

For systems which do not change the magnetic rigidity of the beam we can make some simplifications in the transfer matrix description:

$$(\delta;\delta) = 1 \qquad \text{and all other} \qquad (\delta; \ldots) = 0: \tag{2.11}$$

As a consequence of Liouville's theorem [1] the matrix has a unit determinant, and further since the coordinates in x and y are not coupled we can set

$$(x,y) = (x,b) = (b,x) = (y,x) = (a,y) = (a,b) = (b,a) = (y,a) = 0 \tag{2.12}$$

the phase space volumes are constant in x and y subspaces and corresponding coefficients in the transfer matrix with unite x and y coefficients are equal zero. Finally, for the transfer matrix T we have two decoupled matrices T_x and T_y:

$$T_x = \begin{pmatrix} (x,x) & (x,a) & 0 & (x,\delta) \\ (a,x) & (a,a) & 0 & (a,\delta) \\ (t,x) & (t,a) & 1 & (t,\delta) \\ 0 & 0 & 0 & 1 \end{pmatrix}, \tag{2.13}$$

$$T_y = \begin{pmatrix} (y,y) & (y,b) \\ (b,y) & (b,b) \end{pmatrix} \tag{2.14}$$

assuming that only the x-direction has the dispersive elements.

2.2.1 The field-free region

For any field-free region the deviation of any ray from the optic axis (see Fig. 2.1) can be described by

$$x_2(z_2) = x_1 + (z_2 - z_1)\tan\alpha_1 \tag{2.15}$$

in the one dimensional case. This is true since the inclination stays constant in the field-free region such that

$$a(z) = \tan\alpha(z) = \tan\alpha_1. \tag{2.16}$$

Using the matrix notation, we can rewrite Eqs. 2.15 and 2.16 describing the motion of rays over the drift length $l = z_2 - z_1$ as

$$\begin{pmatrix} x_2 \\ \tan\alpha_2 \end{pmatrix} = \begin{pmatrix} 1 & l \\ 0 & 1 \end{pmatrix} \begin{pmatrix} x_1 \\ \tan\alpha_1 \end{pmatrix} \tag{2.17}$$

or using the coordinates, described before

$$\begin{pmatrix} x_2 \\ a_2 \end{pmatrix} = \begin{pmatrix} 1 & l \\ 0 & 1 \end{pmatrix} \begin{pmatrix} x_1 \\ a_1 \end{pmatrix} \tag{2.18}$$

The same relation between the initial and final parameters will be valid for the y and b coordinates.

---

[1] Liouville's theorem states that under the action of forces which can be derived from a Hamiltonian, the motion of a group of particles is such that the local density of the representative points in the appropriate phase space remains everywhere constant.

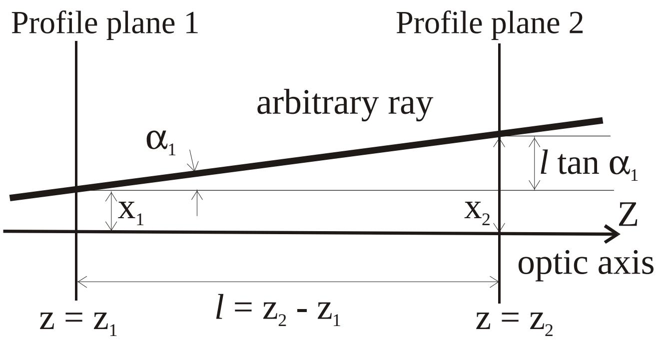

Figure 2.1: Deviation of an arbitrary ray from the optical axis in a field free region.

2.2.2 The sector magnet

A reference particle of momentum $p_0 = m_0\gamma v_0$ and charge (Qe) (see Fig. 2.2)moves in a field with a magnetic flux density B_0 on a circle of radius ρ_0 according the equation

$$B_0\rho_0 = m_0\gamma v_0/(Qe). \tag{2.19}$$

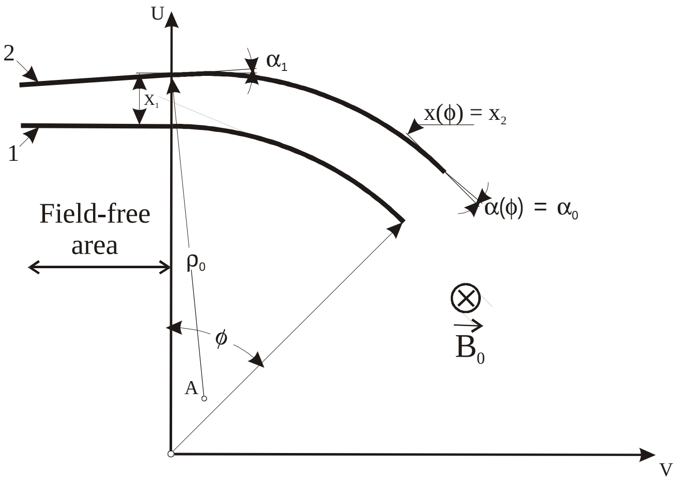

Figure 2.2: The circular optical axis and an arbitrary trajectory of equal radius in a magnetic field $\vec{B}$.

In the u, v coordinate system of Fig 2.2, this optic axis is given as $u^2 + v^2 = \rho_0^2$. The trajectories of a beam of all other particles are then described relative to this optical axis.

Let us assume an arbitrary particle with the same magnetic rigidity $B_0\rho_0 = m_0\gamma v_0/(Qe)$, which does not move along the optic axis but along a paraxial trajectory of equal radius of curvature. Assuming that in the u,v-coordinate system, the center of this circle is at point $A(u,v) = A\,[x_1 + \rho_0(1 - \cos\alpha_1), \rho_0\sin\alpha_1]$ in Fig 2.2, we find the coordinates of a point on this trajectory to be

$$[u - x_1 - \rho_0(1 - \cos\alpha_1)]^2 + [v - \rho_0\sin\alpha_1]^2 = \rho_0^2 \tag{2.20}$$

Here, x_1 and α_1 denote the lateral deviation and the angle of inclination of the paraxial trajectory under consideration relative to the optic axis at $u = 0$. With $x_1 \ll \rho_0$ and $\alpha_1 \ll 1$, all terms higher then first order in x_1/ρ_0 and α_1 may be dropped in a power series expansion of Eq.(2.20), yielding

$$u^2 - 2x_1u + v^2 - 2\rho_0 v\alpha_1 \approx \rho_0^2. \tag{2.21}$$

A beam normally contains particles of different magnetic rigidities $B\rho = B\rho_0(1 + \delta)$. For a constant magnetic flux density, B_0, these particles move along trajectories of different radii of curvature ρ_0 and ρ where we assume

$$\rho = \rho_0(1 + \delta). \tag{2.22}$$

Thus, Eq. 2.20 reads $(u - x_1 - \rho_0 + \rho\cos\alpha_1)^2 + (v - \rho\sin\alpha)^2 = \rho^2$, or keeping only terms of first order in x_1, α_1, δ, then

$$u^2 - 2x_1u + v^2 - 2\rho_0\alpha_1(1 + \delta)v \approx \rho_0^2(1 + 2\delta). \tag{2.23}$$

Since ultimately we need to know the distance x between the paraxial trajectory and the circular optical axis for any angle of deflection ϕ, we shall express the coordinates u and v of a point of the paraxial trajectory as

$$\begin{aligned} u &= [\rho_0 + x(\phi)]\cos\phi, && (2.24)\\ v &= [\rho_0 + x(\phi)]\sin\phi. && (2.25) \end{aligned}$$

Assuming that $u^2 + v^2 - \rho_0^2 \approx 2x(\phi)\rho_0\alpha_1$ and $u \approx \rho_0\cos\phi$, $v \approx \rho_0\sin\phi$ we have

$$\begin{aligned} x(\phi) &= x_1\cos\phi + \rho_0\alpha_1\sin\phi + \rho_0\delta(1 - \cos\phi) + \ldots, && (2.26)\\ \alpha(\phi) &= -(x_1/\rho_0)\sin\phi + \alpha_1\cos\phi + \delta\sin\phi + \ldots, && (2.27) \end{aligned}$$

where $\alpha_1(\phi) \approx dx(\phi)/d(\rho_0\phi) \ll 1$. Since the magnetic field does not change the momentum or the charge of the particle, δ stays constant while the particle moves from profile plane 1 to profile 2. This equation system can also be written as the 3×3 transfer matrix

$$\begin{pmatrix} x_2 \\ \alpha_2 \\ \delta \end{pmatrix} = \begin{pmatrix} c_x & s_x & d_x \\ -s_x/\rho_0^2 & c_x & s_x/\rho_0 \\ 0 & 0 & 1 \end{pmatrix} \begin{pmatrix} x_1 \\ \alpha_1 \\ \delta \end{pmatrix}, \tag{2.28}$$

$$c_x = \cos\phi, \qquad s_x = \rho_0\sin\phi, \qquad d_x = \rho_0(1 - \cos\phi). \tag{2.29}$$

The particle with the magnetic rigidity $B\rho = B\rho_0(1+\delta)$ will be separated from the optical axis at the focal plane of a sector magnet by a distance $(x|\delta)\delta$. The term $(x|\delta)$ is generally referred to as the dispersion, D.

$$D = (x|\delta). \tag{2.30}$$

In order to separate particles of different magnetic rigidities from each other, the distance $(x|\delta)\delta$ must be larger than the width of the image $2x_0(x|x)$. Thus, the minimum resolvable δ is referred to as the resolution, at the image focal plane ($(x|a)=0$) defined by

$$\delta_{min} = \frac{(x|x)}{(x|\delta)}2x_0. \tag{2.31}$$

The reciprocal of this smallest resolvable δ is also known as the resolving power, defined by

$$R = \frac{1}{\delta_{min}} = \frac{D}{2x_0(x|x)}. \tag{2.32}$$

To show the relationship between the resolving power and the area of illumination of the magnet let us assume a homogeneous single-sector-field spectrometer. This kind of system may be arranged as shown in Fig 2.3, where particles with angles $\pm\alpha_0$ originate from an object point of size $2x_0$. The corresponding trajectories in this sector field are found by applying a position vector $X_0 = (0;\alpha_0;0)$ to Eq. 2.28

$$\begin{pmatrix} x_2 \\ \alpha_2 \\ \delta \end{pmatrix} = \begin{pmatrix} c_x & s_x & d_x \\ -s_x/\rho_0^2 & c_x & s_x/\rho_0 \\ 0 & 0 & 1 \end{pmatrix} \begin{pmatrix} 1 & l_1 & 0 \\ 0 & 1 & 0 \\ 0 & 0 & 1 \end{pmatrix} \begin{pmatrix} 0 \\ \alpha_0 \\ 0 \end{pmatrix}; \tag{2.33}$$

where l_1 is the length of initial field-free region. The X_2 position vector describes the particle in any point inside the magnet. Thus, after the magnetic field we find

$$x_2 = \pm(c_x l_1 + s_x)\alpha_0. \tag{2.34}$$

Consequently, the illuminated area A_α is found to be $2\int x_2 d(\rho_0\phi)$, or

$$A_\alpha = 2\int_0^{\rho_0\phi}(c_x l_1 + s_x)\alpha_0 d(\rho_0\phi) = 2(d_x\rho_0 + s_x l_1)\alpha_0. \tag{2.35}$$

or

$$A_\alpha = 2[D + (a|\delta)l_1]\rho_0\alpha_0. \tag{2.36}$$

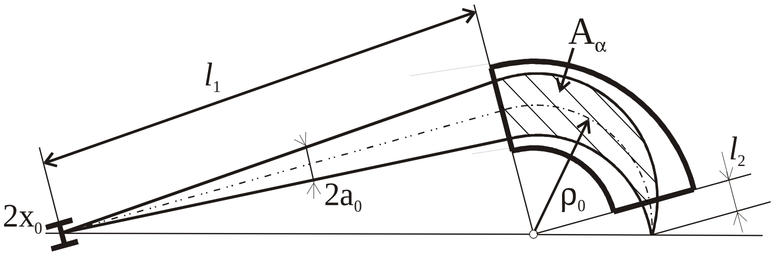

Figure 2.3: The single sector field with bundles of particles that started at the center of the object point under maximal angles $\pm\alpha_0$.

Generally, describing the whole optical system in Fig. 2.3 the dispersion at the focal plane placed downstream from the magnet with the field-free region of length l_2 is

$$D = (x|\delta) + l_2(a|\delta). \tag{2.37}$$

And the dispersion of the reversed optical system is

$$\overleftarrow{D} = (x|\delta) + l_1(a|\delta). \tag{2.38}$$

According [8] and [9] this $\overleftarrow{D} = -R2x_0$, so that Eq.(2.36) becomes

$$2x_0 2a_0 R = A_\alpha/\rho_0. \tag{2.39}$$

The result shows that the area A_α divided by ρ_0 is proportional to the resolving power. Since A_α increases with the square of the size of an instrument, the ratio A_α/ρ_0 increases linearly.

2.2.3 The quadrupole lens

A quadrupole lens is an element in which a charged particle traversing that element experiences a bend towards or away from the optical axis. The bend angle is proportional to the distance of this particle from the optical axis.

The ideal quadrupole consists of four hyperbolic shaped pole faces or electrodes (see Fig. 2.4a). Quadrupole lenses are focusing in one plane and defocusing in the other that is perpendicular. Usually several such lenses must be combined for a useful lens system.

For a magnetic quadrupole of aperture $2G_0$ (see Fig. 2.4a), the scalar magnetic potential is

$$V_B(x, y) = g_B xy, \tag{2.40}$$

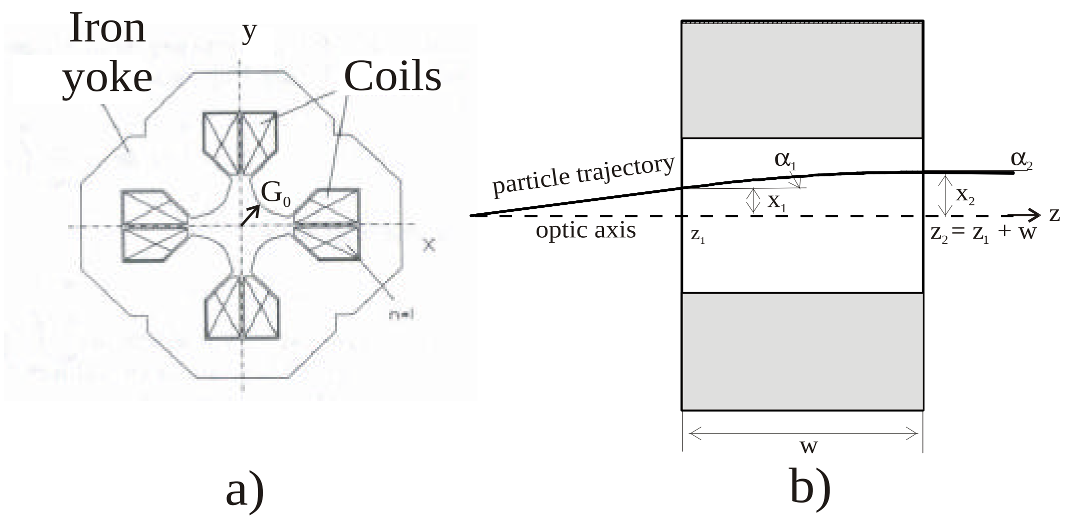

Figure 2.4: a) Schematic view of an iron dominated magnetic quadrupole with the aperture of $2G_0$ in xy plane; b) Trajectory of a charged particle moving through a quadrupole lens of length w.

were g_B is the magnetic field gradient. With $\vec{B} = -\,\mathrm{grad}V_B$, neglecting the fringe field effects, the components of the magnetic flux density $\vec{B}$ then are obtained as

$$
\begin{aligned}
B_x(x;y) &= -\partial V_B/\partial x = -g_B y; && (2.41)\\
B_y(x;y) &= -\partial V_B/\partial y = -g_B x; && (2.42)\\
B_z(x;y) &= 0; && (2.43)
\end{aligned}
$$

yielding constant flux density gradients along the x and y axes. At the pole tips, that is, at $x_T = \pm y_T = \pm G_0/\sqrt{2}$, the magnetic flux density is $B_T = \sqrt{B_x^2 + B_y^2} = \pm G_0 g_B$. Thus, one can describe g_B as

$$g_B = -B_T/G_0: \tag{2.44}$$

With $B_z = 0$, the equations of motion (Eq.2.1) for particles of mass m, charge (Qe), and velocity $\vec{v}$ is found as

$$
\begin{aligned}
m\frac{d^2x}{dt^2} &= -(Qe)v_z g_B x; && (2.45)\\
m\frac{d^2y}{dt^2} &= (Qe)v_z g_B y; && (2.46)
\end{aligned}
$$

or $\frac{d^2x}{dt^2} = -k^2x$, and $\frac{d^2y}{dt^2} = k^2y$, where $k^2 = g_B(Qe)/mv_z$.

For $k^2 > 0$, these differential equations are satisfied by

$$x(z) = c_1 \cos(kz) + d_1 \sin(kz); \tag{2.47}$$

$$y(z) = c_2 \cosh(kz) + d_2 \sinh(kz); \tag{2.48}$$

with undetermined coefficients $c_1; c_2; d_1; d_2$. This solution is periodic in the xz plane and diverges in yz plane. The angles of inclination $\alpha(z)$, $\beta(z)$ can be found from relations $\tan\alpha(z) = dx/dz$ and $\tan\beta(z) = dy/dz$.

If the positions and the angles of inclination of a particle are known at the entrance of the quadrupole (at $z = z_1$ in Fig. 2.4b), we can determine the coefficients $c_1; c_2; d_1; d_2$. Thus, the particle trajectories are given as

$$x(z) = x_1 \cos(kz) + (\tan\alpha_1/k) \sin(kz); \tag{2.49}$$

$$\tan\alpha(z) = -x_1 k \sin(kz) + \tan\alpha_1 \cos(kz); \tag{2.50}$$

$$y(z) = y_1 \cosh(kz) + \tan(\beta_1/k) \sinh(kz); \tag{2.51}$$

$$\tan\beta(z) = y_1 k \sinh(kz) + \tan\beta_1 \cosh(kz): \tag{2.52}$$

Choosing the quantity z to be the length w of the quadrupole, as indicated in Fig. 2.4 these equations can be written in the form of transfer matrices as $\vec{X}_2 = T_x \vec{X}_1$ for the x - direction as

$$\begin{pmatrix} x_2 \\ a_2 \end{pmatrix} = \begin{pmatrix} \cos(kw) & k^{-1} \sin(kw) \\ -k \sin(kw) & \cos(kw) \end{pmatrix} \begin{pmatrix} x_1 \\ a_1 \end{pmatrix} \tag{2.53}$$

2.3 Particle beams and phase space

2.3.1 Phase space areas of particle beams

As described before, the individual particle trajectories are determined for optical systems by solving the Lorentz equation. In order to obtain solutions of this equation it is necessary to know the particle position $(x; y; z)$ as well as the particle momentum $(p_x; p_y; p_z)$ at any given time. Knowing this initial position of a particle in the 6-dimensional so-called 'phase space', it is possible to determine all future positions.

Here we don't describe the trajectory of a single particle but the motion of an ensemble of particles. The most interesting property of the motion of such an ensemble of particles in phase space is described by Liouville's theorem. According to this theorem, a cloud of particles, that at a time t_1 fills a certain volume in phase space may change its shape at a later time t but not the magnitude of this volume.

We assume the particle source, which is extended over a distance $\pm x_1$, as illustrated in Fig. 2.5, emitting charged particles from each point of the source with angles of inclination $\pm\alpha_1$. We shall look only at those particles which pass through

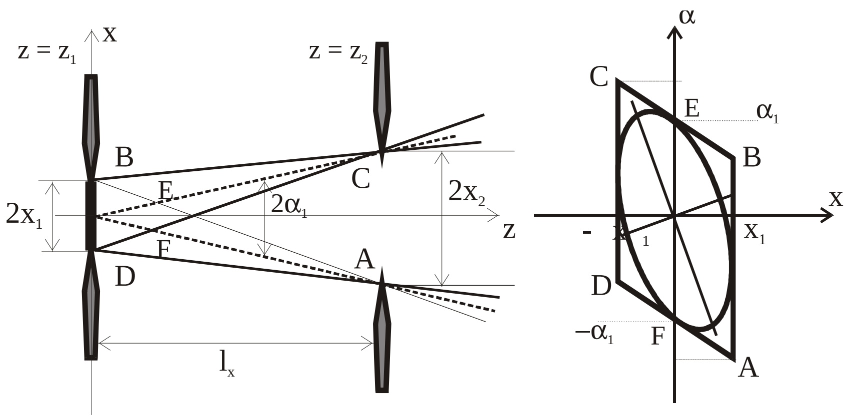

Figure 2.5: Particle trajectories limited by a source of diameter $2x_1$ and diaphragm of diameter $2x_2$ placed at a distance l_x downstream from the source. Also shown is the corresponding parallelogram like $(x; a)$ phase space area (including the inscribed phase space ellipse) of the ensemble of trajectories at $z = z_1$:

an aperture, extending over $§x_2 = §d$, placed at a distance $l_x = z_2$ ¡ z_1 downstream from the object. The size of the object as well as the size of this aperture, the so called "entrance pupil", determines the size of the phase space area occupied by the particle beam at $z = z_1$: Checking the phase space positions of the trajectories A, B, C, D at $z = z_1$, we find this phase space area to be that of a parallelogram of magnitudes

$$A_x = 4" = 4(x_1 a_1): \qquad (2.54)$$

Here, $§®_1$ ¼ $§ \tan a_1 = §d = l_x$ corresponds to the maximum angle under which a particle that started at the center of the object can still pass through the entrance pupil.

In the following we will consider not the parallelogram-like phase space area but the area which is enclosed by the ellipse inscribed within the parallelogram of Fig. 2.5. The area of this ellipse is

$$A_x = ¼"_x = ¼(x_1 a_1); \qquad (2.55)$$

and thus is smaller by a factor of ¼=4 to the area of the corresponding parallelogram.

Assume the upright ellipse phase space area which is defined by its main half-axis x_0 and a_0. The trajectories A an B (see Fig. 2.5) are described by

$$x_{An} = (x_n j x_0) x_0 \text{ ¡ } (x_n j a_0) a_0; \qquad (2.56)$$

$$x_{Bn} = (x_n j x_0) x_0 + (x_n j a_0) a_0: \qquad (2.57)$$

The absolute value of the larger of these two expressions is directly proportional to the magnitude of the envelope $\overline{R}_n = x_{max}(z_n)$ along the particle trajectory at z_n:

$$\overline{R}_{xn} = j(x_n j x_0) j x_0 + j(x_n j a_0) j a_0: \tag{2.58}$$

Analogously, we find the magnitude $S_{xn} = a_{max}(z_n) = \sin ®_{max}(z_n)$, where $®_{max}$ is maximum angle of inclination of the trajectory of the particle beam at z_n:

$$\overline{S}_{xn} = j(a_n j x_0) j x_0 + j(a_n j a_0) j a_0 \tag{2.59}$$

2.3.2 Twiss parameters

In the case of an elliptical phase space area, the beam envelope is formed by different trajectories for each position z_n:[6]

Consider an ellipse as in Fig. 2.6 with minor and major axes of lengths l_a and l_b: In the $\overline{x}$, $\overline{a}$ - coordinate system that coincides with these axes the ellipse is described by

$$µ\frac{\overline{x}}{l_a}¶^2 + µ\frac{\overline{a}}{l_b}¶^2 = 1: \tag{2.60}$$

In an $x; a$ - coordinate system rotated by an angle $µ$ with respect to the $\overline{x}$, $\overline{a}$ coordinates, this ellipse of area $¼"_x = ¼ l_a l_b$ is described by

$$x^2 °_T + 2xa®_T + a^2 ¯_T = "_x; \tag{2.61}$$

where $®_T$, $¯_T$, $°_T$ are the so-called Twiss parameters [10], which read explicitly,

$$\begin{aligned} ®_T &= (l_a = l_b \ ¡ \ l_b = l_a) \sin µ \cos µ; \qquad (2.62) \\ ¯_T &= (l_b = l_a) \sin^2 µ + (l_a = l_b) \cos^2 µ; \qquad (2.63) \\ °_T &= (l_a = l_b) \sin^2 µ + (l_b = l_a) \cos^2 µ: \qquad (2.64) \end{aligned}$$

Combining these relations, we find for any value of $µ$;

$$¯_T °_T \ ¡ \ ®_T^2 = 1: \tag{2.65}$$

Also note that for known Twiss parameters $®_T$, $¯_T$, $°_T$; the inclination of the phase-space ellipse is found from simple trigonometry as

$$\tan 2µ = \frac{2®_T}{°_T \ ¡ \ ¯_T}: \tag{2.66}$$

The n dimensional phase-space ellipse can also be described by the so-called $n£n$ sigma matrix, which will totally define the size and orientation of the ellipse [11]. For

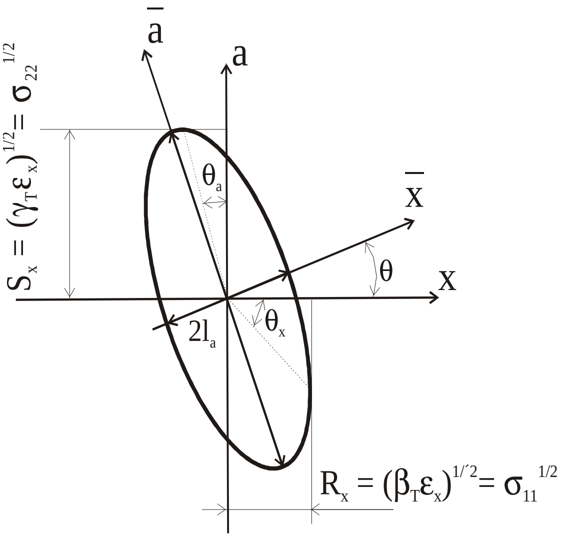

Figure 2.6: A phase space ellipse with minor and major axes of lengths l_a and l_b: x; a- and $\bar{x}$, $\bar{a}$-coordinate systems rotated relative to each other by an angle θ; R_x is the maximal x value and S_x is the maximal a value of any trajectory of the particle beam.

the two dimensional case (as it is drawn in Fig. 2.6). The relationship between the sigma matrix and the Twiss parameters is

$$\sigma = \begin{pmatrix} \sigma_{11} & \sigma_{21} \\ \sigma_{12} & \sigma_{22} \end{pmatrix} = \varepsilon \begin{pmatrix} \beta_T & -\alpha_T \\ -\alpha_T & \gamma_T \end{pmatrix} ; \qquad (2.67)$$

so, the determinant of the sigma matrix is unity and $|\sigma| = \varepsilon_x$.

The sigma-matrix concept characterizes the behavior of an ensemble of particles in contrast to the conventional matrix formalism, where only the coordinates of individual particles are transformed via matrix multiplications. The method to describe the transmission characteristics of a beam is particularly simple if the phase space volume can be approximated by a multidimensional ellipsoid with Gaussian intensity distributions of the single coordinates. The transformation of a beam matrix $\sigma(1)$ [12] by an ion-optical system, characterized by a matrix T, is the canonical matrix transformation:

$$\sigma(2) = T\sigma(1)T^T \qquad (2.68)$$

where T^T is the transposed matrix of T.

2.4 Complex systems

2.4.1 Example 1: Beam Rotator

In some cases it is of interest to rotate the beam around its optical axis so that x and y are exchanged and, for instance, a vertical dispersion of some sector field is turned into a horizontal dispersion. This goal can be certainly be achieved by passing a particle beam through the bore of a solenoid; however, it is also can be realized by a quadrupole multiplet, as was shown in ref. [13].

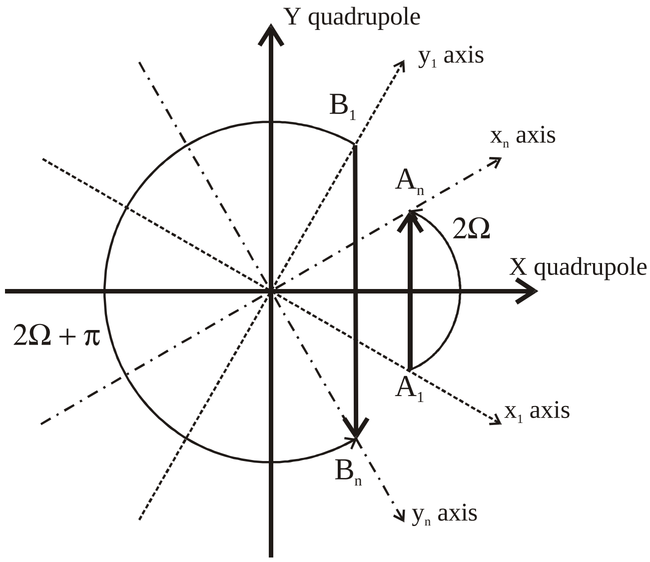

Figure 2.7: A quadrupole multiplet is assumed to form an image with intermediate x image but no intermediate y image, so that $M_x = +1$ and $M_y = -1$. Thus, the points A_1, B_1 are transformed to A_n, B_n and consequently, the $x_1; y_1$- coordinate system transforms into the $x_n; y_n$- coordinate system.

The simplest approach is to require the quadruplet system under consideration to fulfill an object-image relation $(x|a) = (y|b) = 0$ between two profile planes and postulate $(x|x) = -(y|y)$. In this case, points A_1 and B_1 at the object are translated to points A_n and B_n (see Fig. 2.7), which is not really a rotation but rather a mirror action which respect to the $(x = y)$ plane of the quadrupole multiplet.

Assume A_1 and B_1 to be points of the x_1, y_1 axes of Fig. 2.7, rotated by an angle $-\Omega$ relative to the $x; y$ coordinates of the quadrupole. Then, the points A_n and B_n are points on the $x_n; y_n$ axis. Note than x_n axis is rotated by an angle 2Ω, and the y_n axis is rotated by an angle $2\Omega + \pi$ relative to the $x_1; y_1$ coordinate system. For $\Omega = \pi/4$, consequently, the x and y axis are interchanged. Thus, the transfer matrix of the rotator is represented as:

$$\begin{pmatrix} x \\ a \\ y \\ b \\ \delta \end{pmatrix} = \begin{pmatrix} 0 & 0 & -1 & 0 & 0 \\ 0 & 0 & 0 & -1 & 0 \\ 1 & 0 & 0 & 0 & 0 \\ 0 & 1 & 0 & 0 & 0 \\ 0 & 0 & 0 & 0 & 1 \end{pmatrix} \begin{pmatrix} x_0 \\ a_0 \\ y_0 \\ b_0 \\ \delta_0 \end{pmatrix} \tag{2.69}$$

The more general approach requires not only the x, y coordinated to be "rotated", but the a, b values as well, in which case the quadrupole multiplet does not have to satisfy an object-image relation between the two profile planes in question. This problem can always be solved by a combination of five or more quadrupole lenses, which all are rotated by an angle $\pi/4$ [13].

2.4.2 Example 2: the FRS

In general any optical system can consist of n subsystems such as drift lengths, dipoles, quadrupoles and other elements. Each element is described by it's transfer matrices $T_1; T_2; \dots T_n$; and the total system transfer matrix is the multiplication of the submatrices:

$$T = T_n \dots T_2 T_1. \tag{2.70}$$

As an example of a complex system Fig. 2.8 shows the existing FRS facility at GSI [14]. It consists of two symmetric stages in order to ensure the achromatism of the system. Each stage consists of two dipoles and a set of quadrupoles and sextupoles. The four dipoles provide the required magnetic field to bend relativistic heavy ions with $B\rho$ value up to 18 Tm. The quadrupoles in front of the dipoles are adjustable to properly illuminate the bending magnets in order to achieve the required resolution and to maximize the transmission. The quadrupoles following the dipole magnets determine the ion-optical conditions at the four image planes. Sextupole magnets are placed before and after each dipole. They are used to correct second-order aberrations and to avoid the dependencies on momentum of the image plane positions. The physical dimensions of the system (6 m path length per dipole, 70 m total length) are determined by the magnetic rigidity of the investigated particles ($\le$ 18 Tm) and the maximum magnetic fields ($B_{Dipole} \approx 1.6$ T, $B_{Quad} \le 1$ T) achievable with standard technologies. The design of the separator limits the magnetic rigidity and angular acceptances to $\delta B\rho / B\rho_{max} \approx \pm 1.5\%$ and $\Delta\theta_{max} \approx 15$ mrad, respectively.

In its achromatic configuration (standard setting), the FRS has two important image planes, a dispersive one in the midplane (F2) and an achromatic one at the end (F4) (see Fig. 2.8). The main transfer matrix coefficients of this setting at F2 and F4 are listed in Table 2.1. The figure illustrates the trajectory followed by a

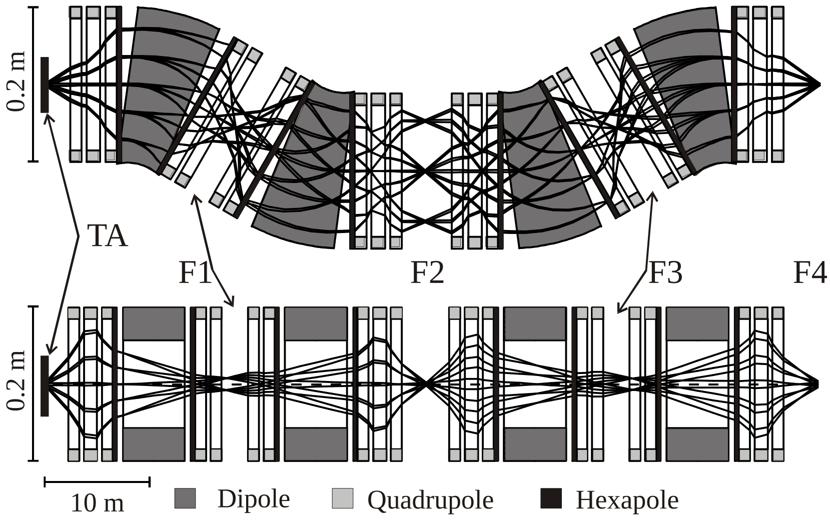

Figure 2.8: Layout of the FRS [14] at GSI showing the most important magnetic elements. Quadrupole magnets are placed before and after each dipole magnet to define the ion-optical conditions at each image plane as well as to maximise the transmission through the separator. F_i (i = 1:::4) define the focal planes of the separator. The hexapole magnets placed in front an behind each dipole stage serve to correct the higher-order aberrations in the system.

particle traversing the FRS with a momentum 1% higher than that of the particle following a central trajectory. A detailed description of the FRS can be found in ref. [14].

Matrix elements	at F2	at F4
(xjx)	0.73	1.0
(xja); [m=rad]	0	0
(xj$\pm_p$); [m]	-6.47	0
(ajx); [rad=m]	0.11	0.1
(aj$\pm_p$); [rad]	0	0
(yjy)	1.23	1.42
(yjb); [m=rad]	0	0
(bjy); [rad=m]	0.55	0.81

Table 2.1. Calculated first-order transfer matrix elements at the focal planes F2 and F4 of the FRS. The momentum deviation $\pm_p$ in parts of the nominal value.

Chapter 3

Ion optical systems with matter

The transfer matrix formalism for fragment separators containing degraders was proposed in ref.[15], [16]. There the first-order transfer matrix of a shaped degrader was introduced and achromaticity condition as well as separation properties of a one-stage separator were described in terms of transfer matrix coefficients. Besides, a simplified representation of these coefficients was proposed, based on an approximate range-velocity dependence of an ion beam in matter. A slightly different approximation of similar accuracy was later used in ref.[17], where it was also proposed to describe degrader properties in the second-order approximation.

Below, we use first order transfer matrix algorithm is introduced to describe general properties of a fragment separator with two degrader stages. A simple representation of degrader transfer matrix coefficients is used, based on a modified range-velocity dependence. This representation can be used not only for a qualitive overview of separator properties, but also for reasonably accurate numerical estimations.

3.1 Non-Liouvillian elements

In the following considerations as same again that in first-order approximation the ion motion can be decoupled in x- and y-directions and only the dispersive x-plane will be described.

It is convenient to replace the position vector introduced in eq. 2.8 by $\overrightarrow{X}_0 = (x; a; \delta v; \delta m; \delta Z)$, since the influence of the degrader on the separation quality in N-Z map of nuclei should be investigated. Here $\delta v = \Delta v/v$, $\delta m = \Delta m/m$ and $\delta Z = \Delta Z/Z$ are the relative velocity, mass and charge to the reference particle, respectively. Moreover, v can be expressed by the dimensionless velocity

$$\beta = v/c; \quad \gamma = (1 - \beta^2)^{-1/2}$$

In the first order approximation the degrader does not change the ion position and trajectory slope but possesses energy, mass and charge dispersive properties, so that its action can be approximately represented by the transfer matrix

$$T_D = \begin{pmatrix} 1 & 0 & 0 & 0 & 0 \\ 0 & 1 & 0 & 0 & 0 \\ W_x & 0 & W_v & W_m & W_Z \\ 0 & 0 & 0 & 1 & 0 \\ 0 & 0 & 0 & 0 & 1 \end{pmatrix} \tag{3.1}$$

Here

$$W_x = \frac{1}{v_2}\frac{\partial v_2}{\partial x};\, W_v = \frac{v_1}{v_2}\frac{\partial v_2}{\partial v_1};\, W_m = \frac{m}{v_2}\frac{\partial v_2}{\partial m};\, W_Z = \frac{Z}{v_2}\frac{\partial v_2}{\partial Z}; \tag{3.2}$$

v_1 and v_2 are the ion velocities in front and behind the degrader, correspondingly. Angular scattering and energy straggling are neglected.

For the coefficients of the degrader transfer matrix a simple approximation can be derived, based on the energy-range relation $r = k(m/Z^2)v^{\lambda}$ [18], [16] for slowing down ions in matter at intermediate energies, where r is the ion range in matter and k and λ some parameters depending on the material, with λ slowly changing with the velocity. In this approximation, the energy loss in the degrader reads

$$v_2 = v_1 \left(1 - \frac{d + \alpha x}{k m v_1^{\lambda_1}} Z^2\right)^{1/\lambda_2} \tag{3.3}$$

with d being the degrader thickness, measured along the optic axis, α the wedge angle of the degrader, $\lambda_1 = \lambda(v_1)$ and $\lambda_2 = \lambda(v_2)$. Differentiating Eq. (3.3) and denoting $\tilde{\lambda} = \lambda + (d\lambda/dv)v \ln v$, following expressions for the transfer matrix coefficients are received:

$$W_x = -\frac{\alpha}{\lambda_2 r_2};\, W_v = \frac{\tilde{\lambda}_1}{\lambda_2}\frac{r_1}{r_2};\, W_m = \frac{d}{\lambda_2 r_2};\, W_Z = -\frac{2d}{\lambda_2 r_2}; \tag{3.4}$$

where r_1 and r_2 are the ion beam ranges in front and behind the degrader, $\tilde{\lambda}_1 = \tilde{\lambda}(v_1)$.

3.2 One-stage fragment separators

The transfer matrix of a sector magnet can be rewritten in the new coordinate system as

$$T_M = \begin{pmatrix} M & 0 & D & D & -D \\ -F & M^{-1} & D' & D' & -D' \\ 0 & 0 & 1 & 0 & 0 \\ 0 & 0 & 0 & 1 & 0 \\ 0 & 0 & 0 & 0 & 1 \end{pmatrix} \tag{3.5}$$

where M is the magnification coefficient $(x|x)$, F is the focal power $(a|x)$, D and D' are the linear and angular dispersion coefficients. A one-stage fragment separator consists of two dispersive magnetic cascades separated by a degrader placed at the image position, so that the system transfer matrix is $T_S = T_{M_2} T_D T_{M_1}$:

$$T_S = \begin{pmatrix} M_2 & 0 & D_2 & D_2 & -D_2 \\ -F_2 & M_2^{-1} & D'_2 & D'_2 & -D'_2 \\ 0 & 0 & 1 & 0 & 0 \\ 0 & 0 & 0 & 1 & 0 \\ 0 & 0 & 0 & 0 & 1 \end{pmatrix} \times \begin{pmatrix} 1 & 0 & 0 & 0 & 0 \\ 0 & 1 & 0 & 0 & 0 \\ W_x & 0 & W_v & W_m & W_Z \\ 0 & 0 & 0 & 1 & 0 \\ 0 & 0 & 0 & 0 & 1 \end{pmatrix} \times \begin{pmatrix} M_1 & 0 & D_1 & D_1 & -D_1 \\ -F_1 & M_1^{-1} & D'_1 & D'_1 & -D'_1 \\ 0 & 0 & 1 & 0 & 0 \\ 0 & 0 & 0 & 1 & 0 \\ 0 & 0 & 0 & 0 & 1 \end{pmatrix};$$

with transfer matrix coefficients:

$$\langle x|x\rangle = M_1 M_2 + D_2 W_x M_1, \tag{3.6}$$

$$\langle x|v\rangle = M_2 D_1 + D_2(W_x D_1 + W_v), \tag{3.7}$$

$$\langle x|m\rangle = M_2 D_1 + D_2(W_x D_1 + W_m + 1), \tag{3.8}$$

$$\langle x|Z\rangle = -M_2 D_1 + D_2(-W_x D_1 + W_Z - 1), \tag{3.9}$$

$$\langle a|a\rangle = M_1^{-1} M_2^{-1}, \tag{3.10}$$

$$\langle a|v\rangle = D'_1/M_2 + W_v D'_2 + D_1(-F_2 + W_x D'_2), \tag{3.11}$$

$$\langle v|v\rangle = W_x D_1 + W_v, \tag{3.12}$$

etc. In an achromatic separator the following two conditions are fulfilled: $\langle x|v\rangle = 0$ and $\langle a|v\rangle = 0$. The first of these conditions will be discussed in more details.

Let

$$Q_i = R_i \varepsilon, \tag{3.13}$$

be the quality factor of the i-th magnetic dispersive cascade with

$$R_i = -\frac{D_i}{2x_i M_i} \tag{3.14}$$

being the resolving power of the cascade. Here $\varepsilon_i = 2x_i 2a_i$ is the phase space occupied by the ion beam, x_i, a_i are initial coordinates at the entrance to the cascade. Then for two consecutive magnetic cascades the quality factors are:

$$Q_1 = -\frac{D_1}{M_1} 2a_1, \qquad Q_2 = -\frac{D_2}{M_2} 2a_2 = \frac{D_2}{M_1 M_2} 2a_1. \tag{3.15}$$

In the just introduced notations for the achromatic separator Eq. (3.7) can be written as

$$W_x D_1 + W_v = \frac{Q_1}{Q_2}, \tag{3.16}$$

or as

$$W_x = \frac{\frac{Q_1}{Q_2} - W_v}{D_1}. \tag{3.17}$$

This means that for any ratio of the optical quality factors of the magnetic cascades preceding and succeeding the degrader, and for any degrader thickness (which defines the coefficient W_v) one can choose the wedge angle (which defines the coefficient W_x) so that the separator becomes achromatic. At the same time

$$\langle v|v\rangle = \frac{Q_1}{Q_2}, \tag{3.18}$$

which means that the relative momentum spread at the exit of the separator is changed depending on the ratio of the quality factors of the cascades preceding and succeeding the degrader. Since the magnification coefficient reads

$$\langle x|x\rangle = W_v M_1 M_2 \frac{Q_2}{Q_1}, \tag{3.19}$$

the transversal phase space at the exit of the achromatic separator is

$$\langle x|x\rangle\langle a|a\rangle = W_v \frac{Q_2}{Q_1}, \tag{3.20}$$

and is thus, first, increased due to the slowing down ions in the degrader and, second, changed inversely proportional to the change of the relative momentum spread.

The mass and charge dispersion coefficients of an achromatic separator are

$$\langle x|m\rangle = D_2(W_v - W_m - 1); \qquad \langle x|Z\rangle = D_2(1 - W_v - W_Z), \tag{3.21}$$

so that the mass and charge resolving powers are

$$R_m = \frac{\langle x|m\rangle}{2|\langle x|x\rangle|x_1} = \frac{R_1}{W_v}(W_v - W_m - 1), \tag{3.22}$$

$$R_Z = \frac{\langle x|Z\rangle}{2|\langle x|x\rangle|x_1} = \frac{R_1}{W_v}(1 - W_v - W_Z), \tag{3.23}$$

and thus are proportional to the momentum resolving power R_1 of the magnetic cascade preceding the degrader but do not depend on the resolving power of the magnetic cascade succeeding the degrader.

As examples, we consider two particular cases:

1) Symmetric achromatic separator, in which $Q_1 = Q_2$. In this case $\langle v|v\rangle = 1$, that is the relative momentum spread is preserved, and the degrader wedge angle is determined from the relation $W_x = (1 - W_v)/D_1$. The transversal phase space at the exit of the separator is increased proportional to slowing down the ion beam: $\langle x|x\rangle\langle a|a\rangle = W_v$.

2) Achromatic separator with a homogeneous degrader, in which $W_x = 0$. In this case the ratio of the quality factors is defined by the degrader thickness: $Q_1/Q_2 = W_v$, the relative momentum spread at the exit from the separator is increased: $\langle v|v\rangle = W_v > 1$, and the transversal phase space is preserved: $\langle x|x\rangle\langle a|a\rangle = 1$.

In approximation of Eq. (3.4) the dispersion free condition of Eq. (3.17) takes the form

$$\alpha = \lambda_2 r_2 \frac{\frac{\widetilde{\lambda}_1}{\lambda_2}\frac{r_1}{r_2} - \frac{Q_1}{Q_2}}{D_1}, \tag{3.24}$$

whereas the mass and charge resolving powers of Eqs. (3.22), (3.23) read

$$R_m = R_1\frac{d}{r_1}\frac{(\widetilde{\lambda}_1 - \lambda_2)\frac{r_2}{d} + \widetilde{\lambda}_1 - 1}{\widetilde{\lambda}_1}, \tag{3.25}$$

$$R_Z = R_1\frac{d}{r_1}\frac{(\lambda_2 - \widetilde{\lambda}_1)\frac{r_2}{d} + 2 - \widetilde{\lambda}_1}{\widetilde{\lambda}_1} \tag{3.26}$$

To get an angular dispersion free system $\langle a|v\rangle = 0$ must be fulfilled. Considering that the first part of the system has zero angular dispersion eq. 3.11 can be rewritten as:

$$W_v D'_2 + D_1(-F_2 + W_x D'_2) = 0. \tag{3.27}$$

From this equation it is clear that the pure ion optical angular dispersion D'_2 of the second stage can not be zero. The expression for the degrader angle α which will fulfil eq. 3.27 is given by:

$$\alpha' = \lambda_2 r_2 \frac{\frac{\widetilde{\lambda}_1}{\lambda_2}\frac{r_1}{r_2}D'_2 - D_1F_2}{D_1D'_2}. \tag{3.28}$$

To obtain an achromatic system i.e. dispersion free as well angular dispersion free eq. 3.24 and 3.28 have to be fulfilled simultaneously, which finally leads to the condition

$$F_2D_2 + M_2D'_2 = 0. \tag{3.29}$$

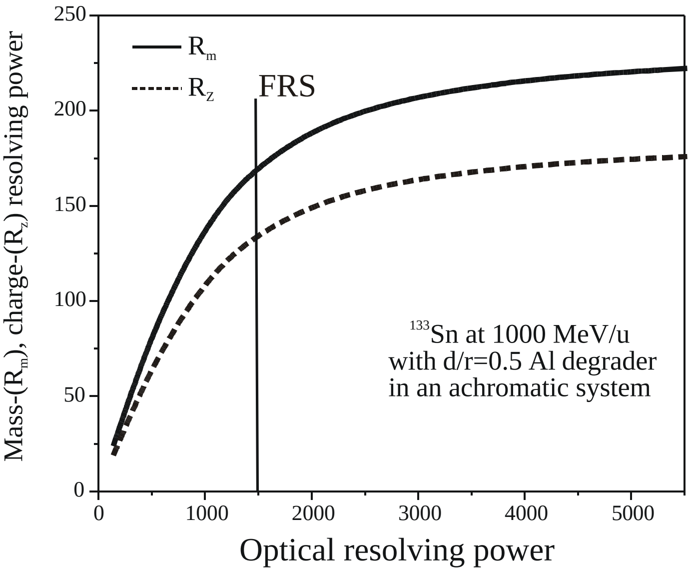

Figure 3.1: Typical example of the dependence of the mass- and charge- resolving powers on the pure ion optical resolving power for the ^{133}Sn fragment with an energy of 1000 MeV/u and a degrader thickness of $d/r = 0.5$. d/r represents the degrader thickness in units of the range corresponding to the fragment's energy in front of the degrader.

These expressions for the resolving powers represent the ideal case. In fact there is also the energy straggling phenomena, which brings an additional broadering of the position distribution at the exit of the degrader due to the energy loss. The energy straggling is written as [18]:

$$\delta E^2 = \left(\frac{dE}{dx}(E_f)\right)^2 \int_{E_f}^{E_i} \frac{\sigma_E^2(E)}{\left[\frac{dE}{dx}(E)\right]^3} dE \qquad (3.30)$$

where E_i and E_f are the fragment energies in front of and behind the degrader, respectively. The energy straggling is a statistical phenomena and it is well described in ref. [19]. Including the energy straggling in the above formula the term $\langle x|x\rangle$ for the achromatic case is expressed as:

$$\langle x|x\rangle = \sqrt{\left(W_v M_1 M_2 \frac{Q_1}{Q_2}\right)^2 + D_2^2 \sigma_E^2(E)}. \qquad (3.31)$$

Thus the equations for the mass- and charge- resolving powers loose the linear dependence from the pure optical resolving power of the system (see Fig. 3.1).

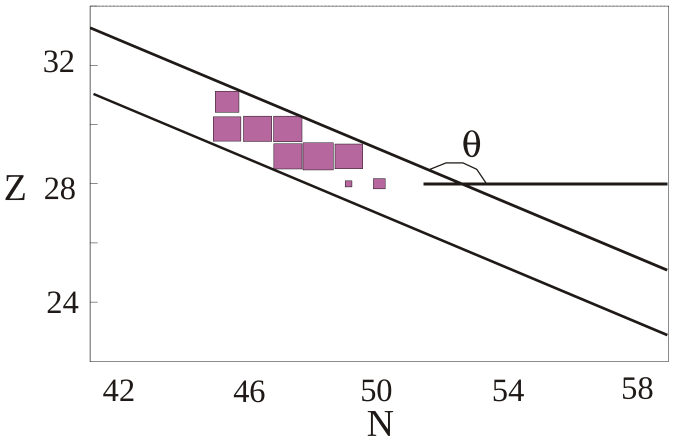

Figure 3.2: The separation quality of a one-stage separator for ^{78}Ni fragment (produced by ^{238}U fission) with an initial energy of 820 MeV/u. The thicknesses of the Al degrader corresponds to half of the range of the fragment in front of the degrader.

The new equations for mass- and charge-resolving powers will be the following:

$$R_m = R_1^*(W_v - W_m - 1) \tag{3.32}$$

$$R_Z = R_1^*(1 - W_v - W_Z); \tag{3.33}$$

where R_1^* is

$$R_1^* = \frac{R_1}{\sqrt{W_o^2 - \frac{D_1^2}{M_1^2}\sigma_E}}. \tag{3.34}$$

3.3 Separation quality of a one-stage fragment separator

Due to the combined mass and charge dispersive properties of a degrader, only those fragments will pass through the fragment separator, which are located along a certain line at the nuclear chart N-Z plane (see Fig. 3.2). The direction of this cut produced by the separator is defined by the equation $\langle x|m\rangle \Delta m/m + \langle x|Z\rangle \Delta Z/Z = 0$. Substituting $\Delta m = \Delta N + \Delta Z$, the following formula for the direction of the cut is obtained

$$\tan\theta = \frac{\Delta Z}{\Delta N} = -\frac{\langle x|m\rangle}{\langle x|m\rangle + \frac{m}{Z}\langle x|Z\rangle}. \tag{3.35}$$

To characterize the separation quality of the separator, we introduce the dispersion coefficient in the direction $\vec{l}$, perpendicular to the direction of the cut line, as $\langle x|l\rangle = m(\delta x/\delta l)$. Since along this direction $\delta N = -\delta l \sin\theta$ and $\delta Z = \delta l \cos\theta$, the dispersion coefficient is

$$\langle x|l\rangle = \sqrt{\langle x|m\rangle^2 + \left(\langle x|m\rangle + \frac{m}{Z}\langle x|Z\rangle\right)^2}. \tag{3.36}$$

Using the approximate expression eq. 3.21 for the degrader transfer matrix coefficients, we come to the relations

$$\cot\theta = \frac{m}{Z}\,\frac{\tilde{\gamma}_1 - 2 + \frac{r_2}{d}(\tilde{\gamma}_1 - \gamma_2)}{\tilde{\gamma}_1 - 1 + \frac{r_2}{d}(\tilde{\gamma}_1 - \gamma_2)} - 1, \tag{3.37}$$

Fig. 3.3 demonstrates how the cut angle in the N-Z plane depends on the energy of the fragments. Calculations are done for three different Ni isotopes, which differ in m/Z by approximately 0.5 each. The thickness of the degrader is fixed to be half of the range of the fragments and the degrader angle α provides the achromatic condition at the final focal plane of the separator. Simulations are done using the ATIMA code [20].

$$\begin{aligned} R_l &= \frac{\langle x|l\rangle}{2|\langle x|x\rangle|x_1} = \\ &= R_1\frac{d}{r_1}\frac{1}{\tilde{\gamma}_1}\sqrt{\left(\tilde{\gamma}_1 - 1 + \frac{r_2}{d}(\tilde{\gamma}_1 - \gamma_2)\right)^2 + K} \qquad (3.38) \\ \text{with } K &= \left(\tilde{\gamma}_1 - 1 + (\tilde{\gamma}_1 - \gamma_2)\frac{r_2}{d}\left(1 - \frac{m}{Z}\right) + \frac{m}{Z}(2 - \tilde{\gamma}_1)\right)^2. \qquad (3.39) \end{aligned}$$

Including the energy straggling effect the following expression for R_l is obtained:

$$R_l = R_1^* \sqrt{(W_v - W_m - 1)^2 + \left(W_v - W_m - 1 + \frac{m}{Z}(1 - W_v - W_Z)\right)^2} \tag{3.40}$$

In reality γ decreases if the energy increases. The value of γ is changing within the range of $1.5 < \gamma < 3$. Thus, the direction of the cut produced by the separator in the N-Z plane of the nuclear chart, depends on the energy of the ion beam passing through the separator. Besides, for a fixed quality factor of the magnetic dispersive cascade and for a fixed degrader thickness relative to the ion beam range, the resolving power of the separator also depends on the ion energy and in general increases with increase of the energy.

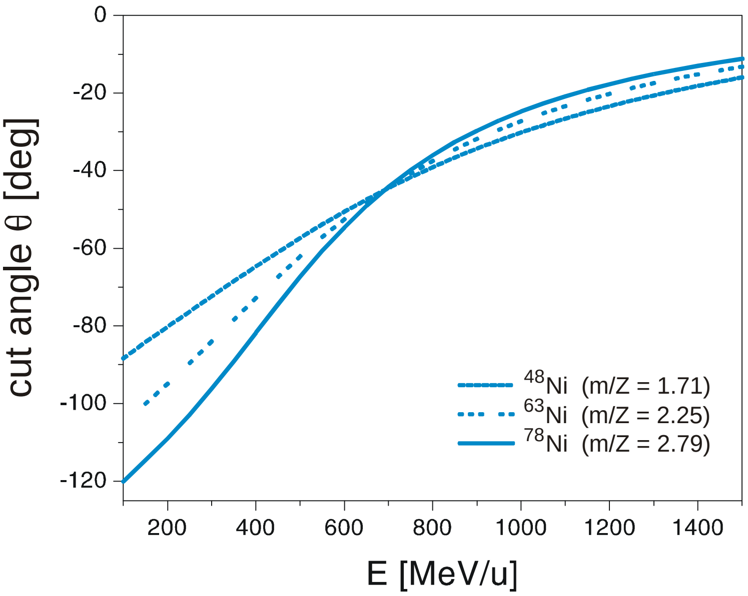

Figure 3.3: The cut angle dependence on the energy of the fragment. The calculations are done using the ATIMA code [20] for infinitly thin degrader. The energy of the Ni fragments was chosen to be 1000 MeV/u.

3.4 Separation quality of a two-stage fragment separator

Assume now a system that consists of two subsequent separator stages with the same bending direction. Both stages are considered to be symmetric, that is in each stage magnetic cascades preceding and succeeding the degrader are the same but included in reversed directions. The subscript I corresponds to the 1st separator and the subscript II to the second one.

Multiplication of transfer matrices of both separator stages gives the following expressions for the coefficients of the overall transfer matrix $T_{2S} = T_{II} T_I$ of the two-stage separator:

$$\langle x|x\rangle = W_{v_{II}} W_{v_I}; \tag{3.41}$$

$$\langle a|a\rangle = 1; \tag{3.42}$$

$$\langle x|m\rangle = W_{v_{II}} \frac{D_I}{M_I}(W_{v_I} - 1 - W_{m_I}) \pm \frac{D_{II}}{M_{II}}(W_{v_{II}} - 1 - W_{m_{II}}); \tag{3.43}$$

$$\langle x|Z\rangle = W_{v_{II}} \frac{D_I}{M_{v_I}}(1 - W_{v_I} - W_{Z_I}) \pm \frac{D_{II}}{M_{II}}(1 - W_{v_{II}} - W_{Z_{II}}): \tag{3.44}$$

Here the "±" means that the M and D terms could have a positive sign as well as a negative. In following formulas the "+" sign will be used assuming algebraic values of these coefficients.

For the direction of the cut line in the N-Z plane as well as for the dispersion of the two-stage separator, Eqs. (3.35) and (3.36) hold, with the dispersion transfer matrix coefficients given by Eqs. (3.43) and (3.44)

Equations (3.36) and (3.37) can be also approximated, using Eq. (3.4). We denote

$$C = \frac{d_{II}}{d_I}\frac{Q_{II}}{Q_I}\frac{\lambda_2}{\widetilde{\lambda}_2}; \quad \Lambda_I = \widetilde{\lambda}_1 + (\widetilde{\lambda}_1 - \lambda_2)\frac{r_2}{d_I}; \quad \Lambda_{II} = \widetilde{\lambda}_2 + (\widetilde{\lambda}_2 - \lambda_3)\frac{r_3}{d_{II}}: \qquad (3.45)$$

where the variables with the subscript 1 correspond to the beam in front of the 1st separator stage, the subscript 2 to the beam between the 1st and the 2nd stages, and the subscript 3 to the beam behind the 2nd stage. Then, we obtain

$$\cot\theta = \frac{m}{Z}\frac{(\Lambda_I - 2) + C(\Lambda_{II} - 2)}{(\Lambda_I - 1) + C(\Lambda_{II} - 1)} - 1; \qquad (3.46)$$

$$\begin{aligned} R_I &= \frac{\langle x|l\rangle}{2|\langle x|x\rangle|x_1} = \\ &= R_I\frac{d_I}{r_1}\frac{1}{\widetilde{\lambda}_1}\sqrt{[(\Lambda_I - 1) + C(\Lambda_{II} - 1)]^2 + K_+} \end{aligned} \qquad (3.47)$$

$$\text{with } K_+ = \left((\Lambda_I - 1) + C(\Lambda_{II} - 1) + \frac{m}{Z}((2 - \Lambda_I) + C(2 - \Lambda_{II}))\right)^2;$$

where x_1 is the half-spread of initial coordinate at the entrance of the two-stage separator. Equation (3.46) means that the direction of the cut line produced by the two-stage separator at the N-Z plane is in between the directions of the cuts that each of the stages would produce separately, and this direction is closer to the direction of the cut that the stage with the larger resolving power would produce.

The consequence of the just mentioned fact is, that in realistic situations the directions of the cuts produced at the exit of the two-stage separator and at the exit of its first stage, are not very different. To increase this difference, one can consider a two-stage separator, in which the bending direction in the 2nd stage is opposite to the bending direction of the 1st stage. In this case Eqs. (3.46) and (3.47) turn to

$$\cot\theta = \frac{m}{Z}\frac{(\Lambda_I - 2) - C(\Lambda_{II} - 2)}{(\Lambda_I - 1) - C(\Lambda_{II} - 1)} - 1; \qquad (3.48)$$

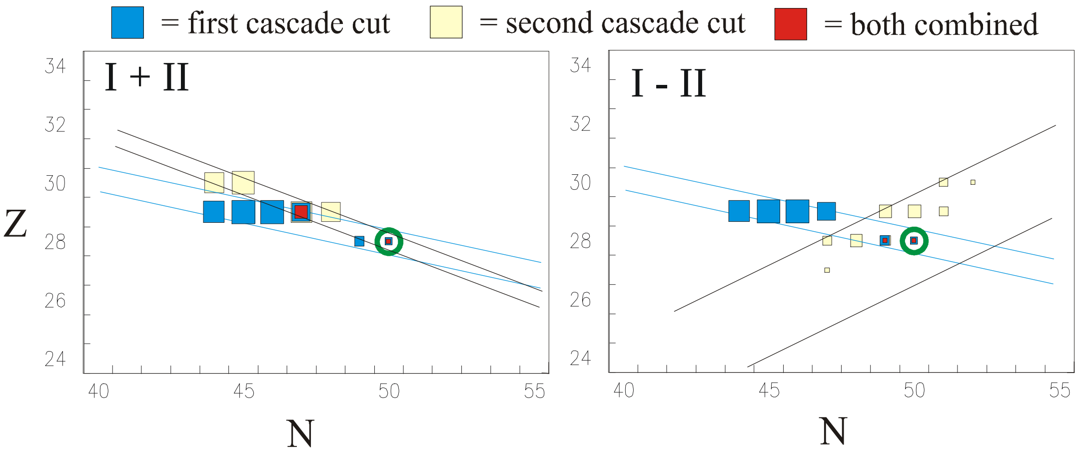

Figure 3.4: The separation quality of a two-cascade separator for ^{78}Ni fragment produced by 1500 MeV/u ^{238}U fission on Be target with the thickness of 1 g/cm^2. The thicknesses of both Al degraders correspond to the half of the range of the fragment in front of each degrader. Left side: the cascades work in adding dispersion mode ("+"); Right side: reversive mode of the separator ("-").

$$R_I = \frac{\langle x|l\rangle}{2|\langle x|x\rangle|x_1} =$$

$$= R_I \frac{d_I}{r_1}\frac{1}{e_1}\sqrt{[(\alpha_I - 1) - C(\alpha_{II} - 1)]^2 + K_-} \qquad (3.49)$$

$$\text{with } K_- = \left((\alpha_I - 1) - C(\alpha_{II} - 1) + \frac{m}{Z}((2 - \alpha_I) - C(2 - \alpha_{II}))\right)^2; \qquad (3.50)$$

in which case the denominator of Eq. (3.48) can be both positive or negative, depending on the ratio of the resolving powers of the 1st and 2nd stages. Thus, the angle θ can vary in a wide range, unlike in the case of Eq. (3.46) in which the denominator is always positive. However, the separator with opposite bending directions of the stages has a smaller resolving power as compared to the separator with the same bending direction.

To include in this formulas the contribution of the energy straggling phenomena the $\langle x|x\rangle$ coefficient should be written as following:

$$\langle x|x\rangle = \sqrt{M_{1II}^2 M_{2II}^2 M_{1I}^2 M_{2I}^2 W_{vI}^2 W_{vII}^2 + M_{1II}^2 M_{2II}^2 W_{vII}^2 D_{2I}^2 \sigma_I(E) + D_{2II}^2 \sigma_{II}(E)}. \qquad (3.51)$$

Chapter 4

Production and separation of exotic nuclei

The two main methods used for separation of exotic nuclei are commonly known as Isotope Separation On-Line (ISOL) ([21], [22]) and In-Flight Separation ([23], [24]).

The ISOL methods relies on the use of a thick target (» 100 g/cm^2), in which a high energy primary beam (100...1000 MeV/u) is almost fully stopped. Usually light mass projectiles (p, d, ®, ...) and refractory targets (UC$_x$) are used. The target is heated to temperatures of typically 2000 K. Thus the reaction products are thermalized and then transported by diffusion from the target to an ionization region before they are accelerated to energies of typically 10 - 100 keV (see Fig. 4.1). Electromagnetic fields separate the nuclei according to their mass over charge ratio and after this the particles are postaccelerated. A mass resolving power R_M = M=±M of typically 20000 is needed, in order to separate neighboring isobars with a mass number of around 100. Some of the running ISOL facilities are listed in Table 4.1.

Name	Place	Accelerator Type	Projectile	Energy MeV/u	Power kW	Intensity μA	Post Accelerator	Energy MeV/u
RNB	Louvain-la Nueve, Belgium	Cyclotron	p	30	6	200	Cyclotron CIME	0,8
SPIRAL	GANIL, Caen, France	Cyclotron	heavy ions	95	6		Cyclotron	25
ISOLDE	CERN, Geniva, Switzerland	PS Booster	p	1400	2	2	Linac	2,2
TRIUMF	Vancouver, Canada	Synchrotron	p	500	50	100	Linac	1,5
HRIBF	Oak Ridge, USA	Cyclotron	p, d, α	100		20	25 - MW tandem	

Table 4:1: Main parameters of some ISOL facilities running worldwide [24]; [25]:

In the In-Flight Separation method a thin target (100...5000 mg/cm^2) is used and the primary beam is not stopped in the target. The typical energies of a primary beam

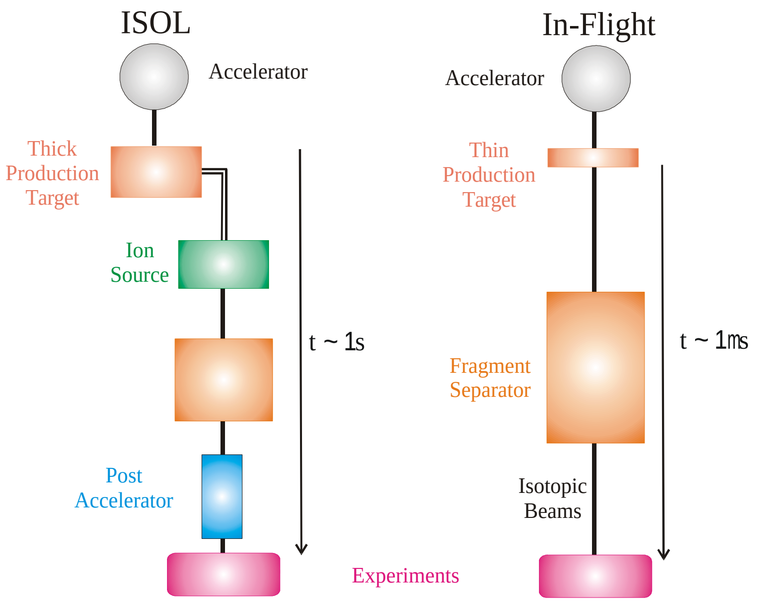

Figure 4.1: The basic methods of production and separation of exotic nuclear beams. Left panel: the ISOL method with associated post-accelerator. Right panel: the In-Flight method [1].

for projectile fragmentation and fission are around 100...1500 MeV/u. The projectile fragments emerge from the target with almost the same velocity as the primary beam and the transversal and longitudinal momentum distributions are narrow, i.e. the fragments are emitted in a narrow angular cone ($< 1^0$). A fragment separator follows directly after the production target. Because the projectile fragments are already at high energies, a post acceleration is not needed. Some running In-Flight facilities are listed in the Table 4.2.

The main advantages of the in-flight separation method can be summarized as follows:

1) in-flight separation is chemistry-independent and thus provides secondary beams of all elements;

2) separation and transport to experimental devices is limited mainly by the time of flight through the separator, typically less than a microsecond, therefore it allows to study very short-lived species;

3) high energies allow the use of thick secondary-reaction targets and thus high luminosities even for rare exotic species;

4) the concept allows both monoisotopic beams or mixed beams of isotopes with similar $A=Z$;

5) with a synchrotron as the driver accelerator, intense short-pulsed beams for

injection into storage rings as well as quasi-continuous secondary beams for fixed target experiments can be provided.

Name	Place	Accelerator Type	Energy, MeV/u
SISSI	GANIL, Caen, France	Cyclotron	95
FRS	GSI, Darmstadt, Germany	Synchrotron	1000
ACCULINNA	Dubna, Russia	U400, U400M Cyclotrons	
A1900	MSU, East Lansing, USA	K500, K1200 Cyclotrons	200
RIPS	RIKEN, Saitama, Japan	Cyclotron	135
RIBLL	IMP, Lanzhou, China	Cyclotron	80

Table 4.2. Characteristics of some worldwide In-Flight facilities [24].

4.1 Exotic nuclei produced In-Flight

The main production mechanisms to create exotic nuclear beams are projectile fragmentation and fission reactions (see Fig. 4.2). In the following some important characteristics of the methods will be introduced.

4.1.1 Projectile Fragmentation

Projectile fragmentation occurs at impact parameters at which the radii of the interacting nuclei overlap.[26] During the short nuclear encounter between projectile and target several nucleons may be abraded off leading to a highly-excited prefragment. In the slower deexcitation step the prefragment decays mainly via evaporation of nucleon. By nuclear fragmentation of relativistic heavy ions, exotic beams over the entire periodic table up to uranium are produced depending on the primary beam and the target material used.

At energies of about 1000 MeV/u the total cross section σ_n is mainly determined by the geometric dimensions of the colliding nuclei. It can be described using Kox parametrization [27]:

$$\sigma_n = \pi r_0^2 (1 - \frac{B}{E_{cm}})(A_p^{1/3} + A_t^{1/3} + a\frac{A_p^{1/3} A_t^{1/3}}{A_p^{1/3} + A_t^{1/3}} - b)^2 \tag{4.1}$$

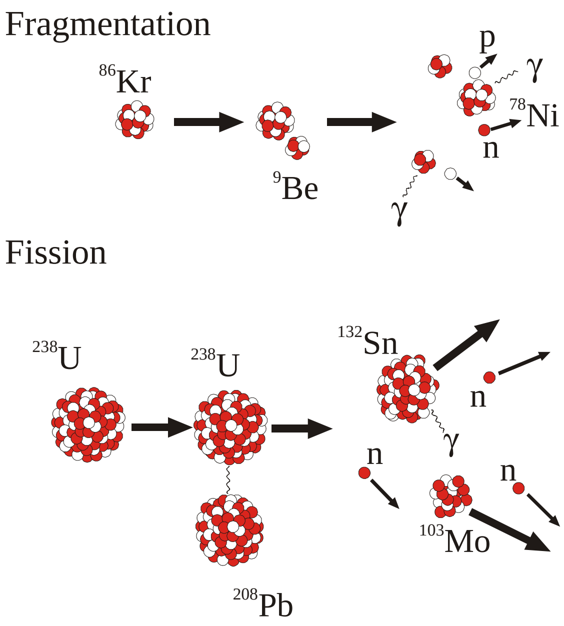

Figure 4.2: The main production mechanisms to create the exotic nuclei in-flight are projectile fragmentation and projectile fission processes.

where $r_0 = 1.1$ fm and $a = 0.85$. The surface transparency parameter b is slightly energy dependent with a value $b = 2.05$ at energies in the range $E/A = 200 - 300$ MeV/u and value of $b = 1.9$ at higher energies. B is the expression for the Coulomb barrier and E_{cm} is the energy of the center-of-masses.

In collisions of relativistic ions with large Z electromagnetic processes contribute appreciably to the total cross section. These can be described as an excitation of the Giant Dipole Resonance (GDR) by the virtual photon spectrum generated by the target nucleus (see also Fig. 4.2). The GDR then decays primarily into the 1n-, 2n- an f-channels. The total cross section for electromagnetic dissociation can be calculated by folding Weizsaecker-Williams virtual photon spectrum [28] with the tabulated Lorenz-curve parameters of the GDR [29].

The kinematics of nuclei produced in projectile-fragmentation reactions is mainly determined by two effects - the Fermi momentum of the nucleons abraded in the interaction between the projectile and the target, and the later evaporation of nucleons from the excited projectile residue. In the frame of the Fermi-gas model, the momenta of the fragments follow a Gaussian distribution. The sum of these momenta is zero in the centre-of-mass frame of reaction

$$\vec{P}_{CM} = \sum_{i=1} \vec{p}_i = 0 \qquad (4.2)$$

where $\vec{P}_{CM}$ is the momentum of the nucleus in the centre-of-mass frame, N is the number of nucleons and $\vec{p}_i$ is the momentum of each nucleon. After the collision, some nucleons from the projectile will be ejected, while the projectile-like residue (prefragment) will be left with some excitation energy. Due to conservation of momentum, the ejected nucleons and the prefragment will have opposite momenta in the centre-of-mass frame

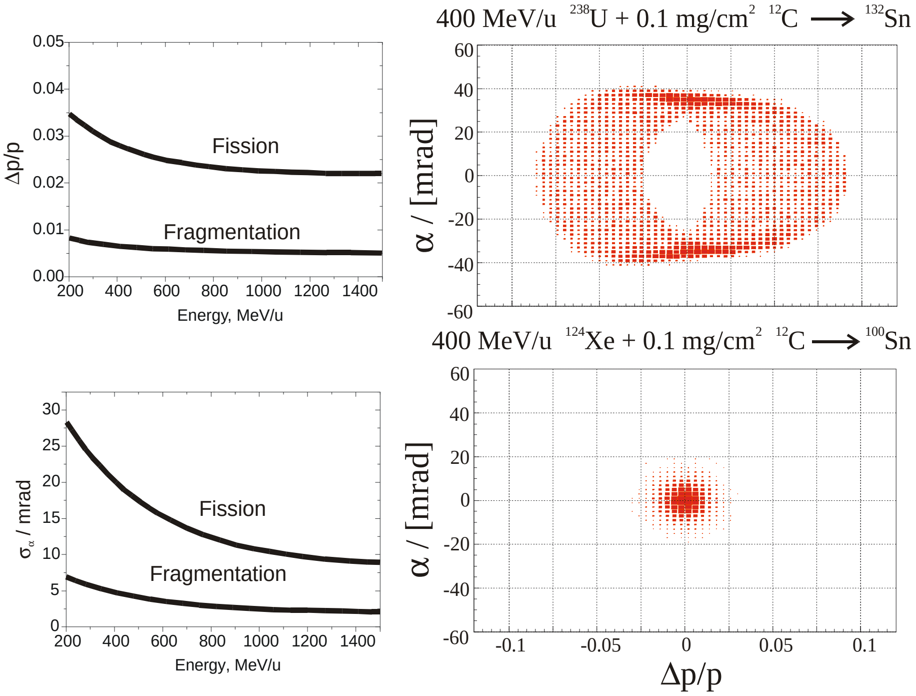

Figure 4.3: Left panel: Standard deviations of the momentum and angular distributions for ^{132}Sn and ^{100}Sn fragments produced via ^{238}U projectile fission and ^{124}Xe fragmentation, respectively. The curves, as a functions of the incident projectile energy, are shown for a very thin target (0.1 mg/cm^2). Right panel: Typical example for the reaction kinematics of projectile fission and projectile fragmentation. Angular and momentum distribution of ^{132}Sn fission fragments compared to ^{100}Sn projectile fragments. The fission products are created with 400 MeV/u ^{238}U projectile in a 0.1 mg/cm^2 carbon target and ^{100}Sn is produced with 400 MeV/u ^{124}Xe in a 0.1 mg/cm^2 carbon target [54].

$$\vec{P}^{f}_{CM} = \sum_{i=n} \vec{p}_i = -\sum_{i=1} \vec{p}_i \tag{4.3}$$

where $\vec{P}^{f}_{CM}$ is the momentum of the prefragment in the centre-of-mass frame and n is the number of ejected nucleons. Since the momenta of the ejected nucleons can be modelled after Gaussian distribution, then one may conclude that the same type of distribution exists for the momentum of the prefragments.

Taking these considerations into account, Goldhaber calculated the width of this Gaussian distribution for the longitudinal momentum component [30]

$$\sigma(p_{\parallel}) = \frac{p_F}{\sqrt{5}} \sqrt{\frac{A_f(A_p - A_f)}{A_p - 1}} \tag{4.4}$$

where p_F is the Fermi momentum of the nucleons, A_p is the mass of the projectile and A_f is the mass of the fragment.

Later, Morrissey determined a semiempirical parametrization of $\sigma(p_{\parallel})$, including the effect of the evaporation of nucleons from the excited projectile residue, which leads to a broadening of the longitudinal momentum distribution [31]

$$\sigma(p_{\parallel}) = \frac{150}{\sqrt{3}} \sqrt{A_p - A_f} \quad (\mathrm{MeV}/c) \tag{4.5}$$

The variance of the transverse momentum is composed of the contribution from the intrinsic motion of the nucleons and an additional contribution from the reaction of the order of $\sigma_n^2(p_{\perp}) \approx 0.3$ GeV/c [32] so that

$$\sigma^2(p_{\perp}) = \sigma^2(p_{\parallel}) + \sigma_n^2(p_{\perp}) \tag{4.6}$$

Therefore, to calculate the width of the angular distribution in the reference particle frame one has to divide $\sigma(p_{\perp})$ by the longitudinal momentum component. In the laboratory frame, the distribution of the longitudinal component is approximately centered at the momentum of the primary beam. Therefore, the value of θ for the fragment of interest will be

$$\theta = \frac{\sigma(p_{\perp})}{p_{\parallel}} \tag{4.7}$$

For the same projectile fragments with masses $A_f = 0.9A_p$ this gives deflection angles of the order of 2.2...1.5 mrad.

4.1.2 Projectile Fission

Spontaneous or induced fission of heavy nuclei produce neutron-rich nuclei in the medium mass range [33]. The kinematics of fission products is determined by the Coulomb repulsion. Therefore, the most probable value of the total kinetic energy of the fission fragments in the rest frame of the mother nucleus can be predicted as

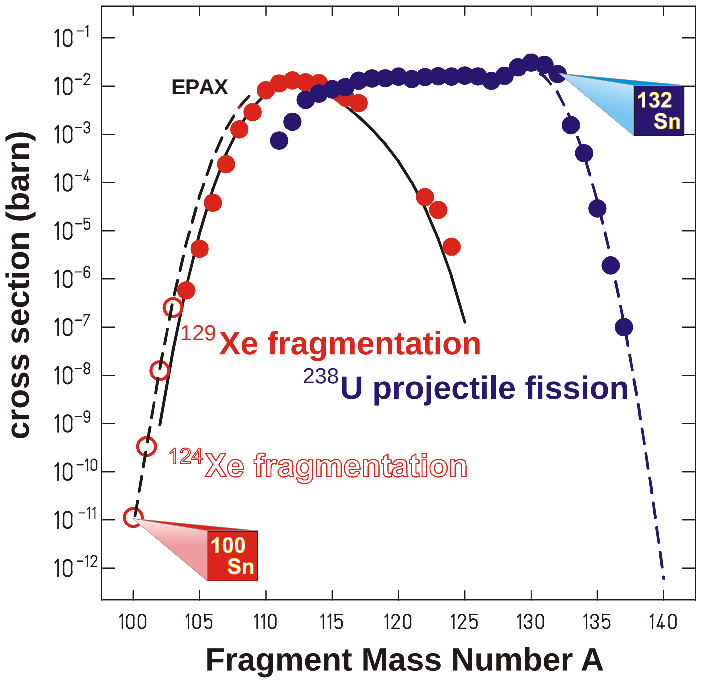

Figure 4.4: The cross sections of Sn isotopes from projectile fragmentation and projectile fission [37].

a simple function of the Coulomb parameter $(Z^2/A^{1/3})$ [35]. For projectiles that can undergo fission, like some uranium isotopes, the interaction with the target can cause an excitation above the fission barrier. The fission products are neutron rich and for some isotopes this method can offer higher yields as compared to fragmentation (see also Fig. 4.4). The kinetic energy of the selected fission fragment follows from energy and momentum conservation. The spread in kinetic energy for a fixed mass ratio is less than 10% indicating the small variation of the fragment separation distance at the point of scission [36].

At relativistic energies, nuclear disintegration after Coulomb excitation becomes important.[2] The Lorentz-contracted Coulomb field of relativistic heavy ions with large proton numbers mainly excites the giant dipole resonance of the projectile; for an energetic heavy nucleus (for uranium $E \geq 3000$ MeV/u), the probability of Coulomb excitation in the field of a heavy target will exceed the geometrical cross section[38]. Subsequently one- or two-neutron evaporation leads to the enhanced production of isotopes in the vicinity of the projectile. The isotopic distributions created by induced fission are determined by the excitation energy. For example, fission of ^{238}U, induced by thermal neutrons from nuclear reactors, creates the well-known double-humped fragment distribution forced by the strong shell effects [33].

For increasing excitation energy, the influence of the shells disappears and the valley in the double-humped distribution is filled [39], until for proton- and heavy-ion-induced fission, a symmetric mass distribution is observed that also can be well described [40].

The kinetic energy of these residues can be calculated from the Brosa [41] or Viola [35] models

$$E_K = 0.14\frac{Z_1Z_2}{A^{1/3}} - 30\ \text{MeV, (Brosa),} \tag{4.8}$$

$$E_K = 0.1189\frac{Z_1Z_2}{A^{1/3}} + 7.3\ \text{MeV, (Viola)} \tag{4.9}$$

where Z_1 and Z_2 are the nuclear-charge of the two fission products and A is the mass number of the mother nuclei.

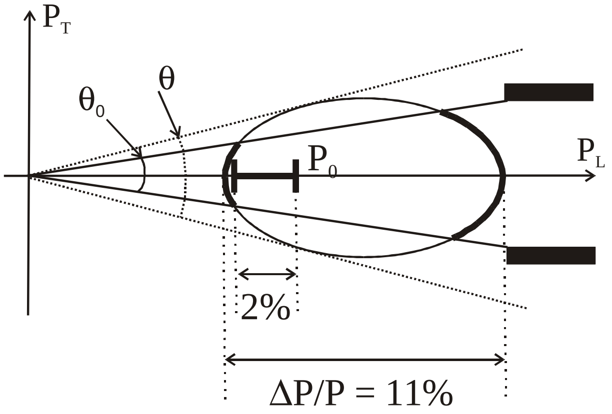

Figure 4.5: Schematic representation of the momentum distribution in the laboratory frame of fission residues produced in heavy-ion collisions. P_T and P_L represent the transversal and longitudinal momentum, respectively. The solid segment represents the momentum acceptance of the present FRS, and P_0 is the momentum of the particle following a trajectory centred along the optical axis of the FRS. Only nuclei with momentum deviations up to ±1.0% will be transmitted through the separator. $\Delta P/P = 11\%$ corresponds to the momentum spread of ^{78}Ni fragment, produced via ^{238}U fission with an initial energy of 1500 MeV/u. Angular acceptance of the FRS cutting the ellipsoidal distribution of fission fragments in the space of momenta. Only nuclei with angles lower than θ_0 will be transmitted through the separator.

The final momentum distribution of the fission residues is spherical in the centre-of-mass frame of the reaction with a radius given by the kinetic energy calculated with the Eq. 4.8. Due to the Lorentz transformation from the centre-of-mass frame into the laboratory frame, this spherical distribution becomes an ellipsoid (see Fig. 4.5).

In the case of a fission product like ^{78}Ni having the same energy as the ^{238}U primary beam, 1500 MeV/u in the laboratory frame, the angular and momentum spread are about ± 30 mrad and 11%, respectively. If these values are compared with the acceptances of the FRS, one realizes that the transmission of such products is quite low.

Fig 4.5 illustrate the effect of the limited momentum and angular acceptance of a fragment separator for the fission residues. These nuclei populate the border of the ellipsoid in momentum space. The centre of mass of this ellipsoid roughly corresponds to the beam momentum. Those nuclei with momentum P_0 follow a trajectory centered along the optical axis of the FRS. The figure shows that only nuclei with momentum deviations of $\leq \pm 1.0\%$ can pass through the spectrometer. It also shows the cuts in the momentum distribution of the fission residues which belong to the limited angular acceptance of the separator. In the space of momenta, the angular acceptance defines a cone which cuts the ellipsoidal distribution. Only those nuclei inside the cone will be transmitted.

4.2 In-Flight separation

4.2.1 Separation by A and Z

A fragment separator has to offer more than just a $B\rho$ separation in order to be useful for the separation of secondary beams. Since the most interesting rare isotopes are also the ones that have the smallest production cross sections, the separator must be able to capture a large fraction of the angular and momentum range of the selected fragment. To achieve a $B\rho$ separation, most fragment separators consist of two dispersive stages, where the first stage does the selection and the second stage eliminates the dispersion of the first stage and provides an achromatic system. However, a separator consisting only of magnetic elements is not capable to resolve fragments with the same A/Z ratio and almost the same velocity. To overcome this, an energy degrader could be used (see Fig. 4.6). A degrader is a non-Liouvillian optical element (see Chapter 3) and can enforce favorable optical conditions on the separator. Because the atomic slowing down of the ions is proportional to Z^2/v^2 [42], different isotopes will have different velocities after passing through the degrader. This change in velocity causes the isotopes with the same A/Z ratio to be separated out in the second dispersive stage with the aim of the slits. Since the energy loss in the degrader also depends on the particle velocity, the degrader must be shaped in such way that the thicker degrader part interacts with the high velocity side and a thinner degrader at lower velocities in order to keep achromaticity.

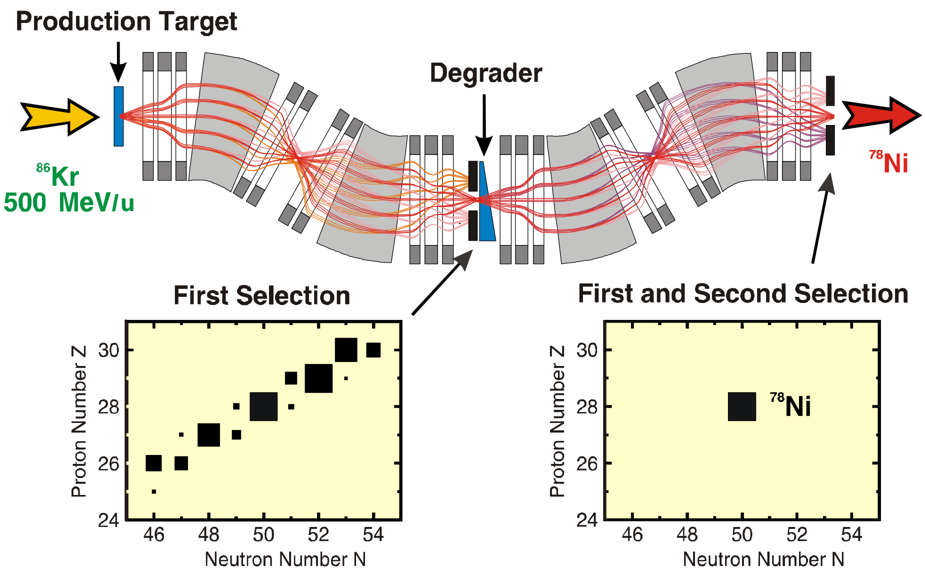

Figure 4.6: Calculated separation performance of the FRS for the doubly-magic nuclei ^{78}Ni, which is produced via fragmentation of ^{86}Kr projectiles in 1g/cm^2 Be target at 500 MeV/u.

4.2.2 Energy operation domain of the projectile

The B½ ¡ ¢E ¡ B½ method is most effective if the energy of the fragments is high enough to ensure that the ions emerging from the production target or from the thick energy degrader are fully stripped. Table 4.3 compares the charge state population for a uranium beam passing a Be target of 1 g/cm^2 for an energy of 400 MeV/u and 1500 MeV/u, respectively. The calculations were done using the GLOBAL code [43], [45].

Primary beam energy, / [Mev/u]	U^{92+}, / %	U^{91+}, / %	U^{90+}, / %	U^{89+}, / %
400	4	30	60	6
1500	64	32	4	0

Table 4.3 Calculated charge state distribution of ^{238}U after passing a 1 g/cm^2 Be target. Calculations are done for a primary beam energy of 400 MeV/u and 1500 MeV/u, respectively, using the GLOBAL code [43] The initial charge state of ^{238}U was 73+.

Fragments in several charge states cause ambiguities in the B½ analysis. On the other hand, the thicknesses of production target and degraders have to be optimized to prevent excessive losses due to secondary nuclear reactions. These two main design criteria, the charge-state population and the nuclear absorption, are shown in Fig. 4.7 as a function of the atomic number Z of the separated fragments for a Nb degrader. In these examples the total degrader thickness corresponds to half of the stopping range of the fragments in Nb. The red line connects those energies at which 50% of the produced fragments are lost due to secondary reactions. For energies above this curve the nuclear reaction probability is larger. The lower energy limits (black lines) result from the conditions where 80%, 90%, and 95% of the fragments are fully stripped.

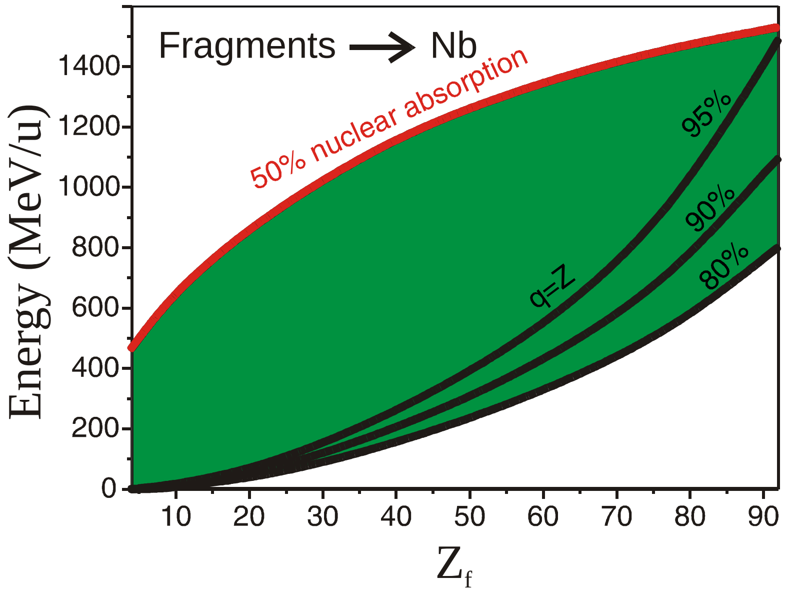

Figure 4.7: The optimization of the $B\rho - \Delta E - B\rho$ separation requires choosing the energy of the projectiles and fragments emerging from the production target high enough on the one hand, to yield a high degree of fully ionized ions, and on the other hand, to limit the losses due to secondary reactions. The latter gives the upper energy range (red line) for a chosen degrader thickness corresponding to half of the range in Nb. The former condition is indicated by the black lines drawn for fractions of 95%, 90% and 80% of fully stripped ions, respectively. The calculation is performed for isotopes with $A/Z = 2.6$.

The loss of fragments due to secondary reactions in the degrader can be expressed by the nuclear absorption coefficient μ:

$$\mu = \frac{N_A}{A_D}(\sigma_{Nuc} + \sigma_{ED}) \tag{4.10}$$

N_A is Avogadro's constant, A_D is the mass number of the degrader material, σ_{Nuc} and σ_{ED} are the total cross sections for nuclear reactions and electromagnetic dissociation, respectively. The upper curve in Fig. 4.7 represents the energy which fulfills the following condition:

$$e^{-\mu d} = 1/2 \qquad \text{with } d = r_f/2; \tag{4.11}$$

where d is the degrader thickness at the center.

The range r_f depends strongly on the energy of the fragments, while the absorption coefficient μ is nearly constant as long as the electromagnetic dissociation can be neglected. In this case, the corresponding 1/e thickness of a fragment with mass number A_f in a degrader material and with mass number A_d can be estimated by the relation [18]:

$$1/\mu \approx 44 \left(\frac{A_d}{A_d^{1/3} + A_f^{1/3}} \right)^2 \quad \mathrm{g/cm^2} \tag{4.12}$$

Both μ and r_f depend on the degrader material. In order to minimize the loss of fragments during the slowing-down process, the ratio of atomic interactions relative to the nuclear reactions must be maximized.

Niobium is an optimum stripping material at about 1000 MeV/u and is currently used in the FRS in particular for experiments with the heaviest fragments.

4.3 Limitations of the present exotic beam facility at GSI

As a conclusion the present secondary beam facility at GSI (see Fig. 4.8) has the following limitations:

1) low intensity primary beams due to the space charge limit of the existing synchrotron SIS18 [46]. To solve this problem a new accelerator complex is needed which can deliver uranium beams in lower charge states (U^{28+}) with high repetition rate.

2) the present FRS was designed to handle projectile fragmentation reactions. To transmit also fission products a fragment separator with larger acceptance is needed.

3) low transmission to the rings and experimental caves due to the fact that the beam lines were designed for the phase space of a primary beam but not for the secondary beams which occupy much larger phase spaces. To provide better beam transmission to all users an improved overall layout must be designed.

4) the present facility is restricted to a maximum magnetic rigidity of 18 Tm. As explained before in Chapter 4.3.2 this limit should be raised to at least 20 Tm.

5) the one-stage separation principle does not work properly for fission projects because of the essential overlap of the broad momentum spreads for the neighboring isotopes.

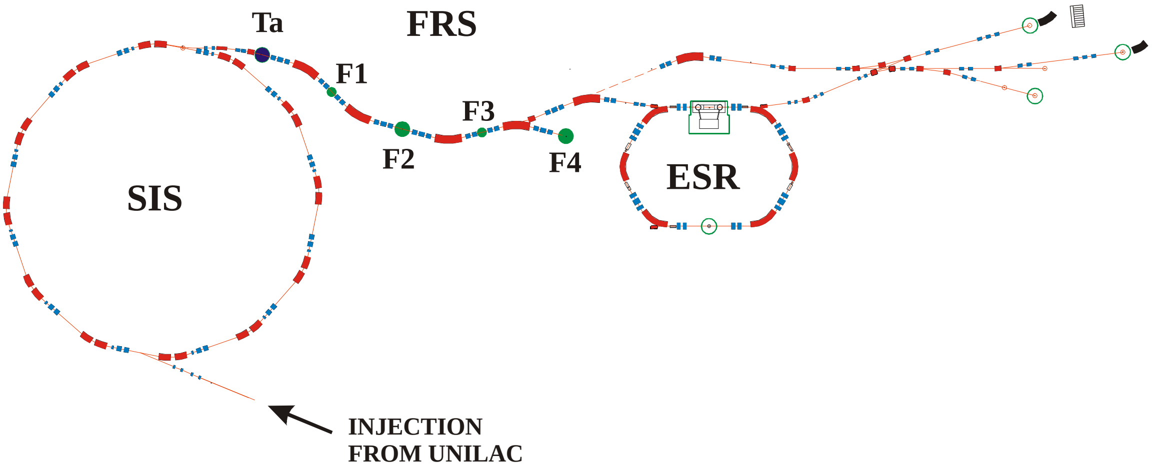

Figure 4.8: Present exotic nuclear beams facility at GSI

Chapter 5

From SIS100/200 to the Super-FRS target

5.1 Accelerator concept of the new GSI facility

The key instrument of the planned new accelerator facility is a synchrotron complex, which consists of two rings having 100 and 200 Tm maximum magnetic rigidity, respectively. Both rings will have an equal circumferences of about 1100 m and will be installed underground in a common tunnel tube (Fig. 5.1) at a level of -24 m [3]. The existing UNILAC/SIS18 facility serves as an injector. Primary ion beams of all elements from hydrogen to uranium are provided with intensities of two to three orders of magnitude larger than those of the present GSI facility. For both synchrotrons, superconducting magnets shall be used to save on initial investment and operation costs.

The first synchrotron (SIS100, $(B\rho)_{max} = 100$ Tm) will provide pulsed uranium ($q = 28+$) beams with intensities of 1×10^{12} ions/pulse at energies up to 2.7 GeV/u, and pulsed proton beams with intensities of 2.5×10^{13} at 29 GeV. For both heavy-ions and for protons the particles can be compressed into bunches with a full width of 50 ns, which is required for efficient injection into the collector and/or storage ring. Such short, intense ion bunches are also required for plasma physics experiments. The double ring concept enables high average intensities of up to 1×10^{12} heavy ions per second at energies of $\approx$1500 MeV/u provided for fixed target experiments. This is possible by transferring the SIS100 beams to the 200 Tm ring (SIS200), which is used as a stretcher ring with subsequent slow extraction (quasi DC-beams).

The main characteristics of the SIS100/200 synchrotrons relevant for Super-FRS experiments are listed in Table 5.1.

Figure 5.1: Schematic view of the tunnel with two synchrotron rings SIS100/200 [3]

Primary Beam Parameters	Slow-Extraction Mode	Fast-Extraction Mode
Ion species	p - U	p - U
Intensity	10^{12}/s	10^{12}=spill
Spill Length	quasi DC	50 ns
Operating Energy ($^{238}U^{28+}$)	1500 MeV/u	1500 MeV/u
Emittance ("$_x$, "$_y$)	(13, 5) ¼ mm mrad	(26, 10) ¼ mm mrad
Momentum Spread	§ 0:07 %	§ 1 %

Table 5.1 Key parameters of SIS100/200 for primary beams provided for the Super-FRS. The values for emittance and momentum spread represent two standard deviations.

5.2 Beam transport from SIS100/200 to the Super-FRS target

The beam transport system delivers the accelerated ion beams from either the SIS100 or the SIS200 ring to the individual experimental facilities. Both rings as well as the transport beam lines are placed on top of each other with a separation distance of

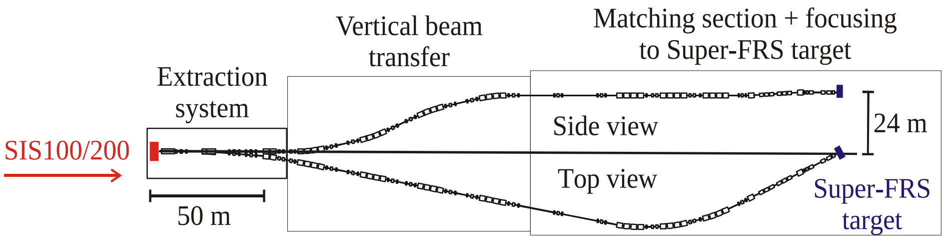

Figure 5.2: Beam line topology. Upper part: side view; Lower part: top view. The three achromatic systems (extraction, vertical transfer and matching part) are indicated.

1.3 - 1.5 m. A vertical beam transfer channel from the SIS100 level to the SIS200 level is located just in front of the focusing system of the Super-FRS target station.

The design of the beam transport system is based on dipole magnets with a maximum flux density of 2 T. It takes into account the parallel operation of the beam lines for different experiments. Thus, the beam lines may be equipped with either superconducting magnets or iron dominated, normal conducting magnets. With respect to the long term operation costs, superconducting magnets are more favorable.

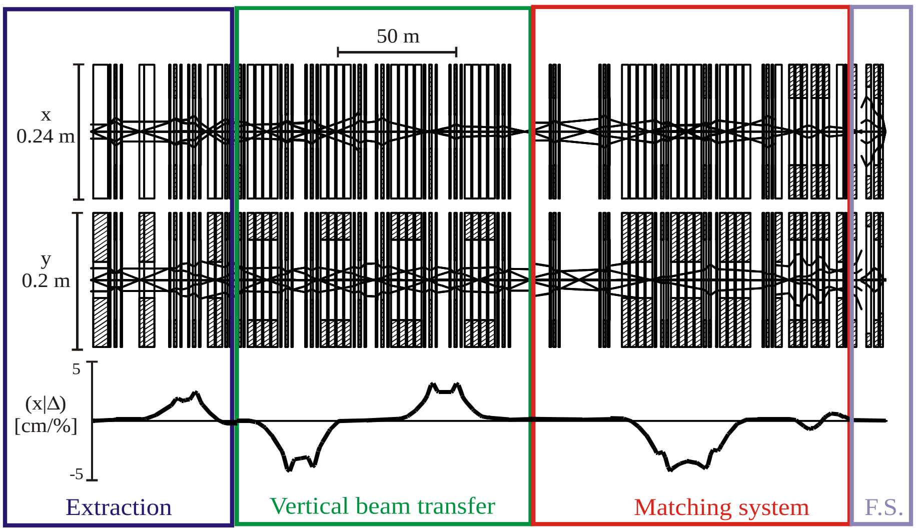

Figure 5.3: The ion optical layout of the transport beam line from the SIS100/200 to the Super-FRS target. Shown are the extraction system at -24 m, the vertical beam transfer and the horizontal matching system with the focusing system (F.S.). Trajectories are drawn for $\varepsilon_x = \varepsilon_y = 25\pi$ mm mrad.

The transfer line from SIS100/200 to the Super-FRS consists of the three following achromatic stages: 1) the extraction from the synchrotron, 2) the vertical transfer line from the -24 m level to ground level and 3) the horizontal matching part on ground level, which adjusts the beam line to the focusing system for the target station of the Super-FRS. The topology of the beam transport line is shown in the Fig. 5.2 and the ion optical design is shown in Fig. 5.3.

5.3 Focusing systems for the Super-FRS target

The focusing system for the Super-FRS connects the matching section of the transport beam line with the target. The general characteristics of the primary beam were already given in Table 5.1. For designing the focusing system the following additional parameters are taken into account:

1) Maximum magnetic rigidity 100 Tm;

2) Twiss parameters at the entrance of the focusing system:
x-direction: $\alpha_x = 0$, $\beta_x = 18.348$ mm/mrad (corresponds to $x_0 = \pm 21.4$ mm)
y-direction: $\alpha_y = 0$, $\beta_y = 20.392$ mm/mrad (corresponds to $y_0 = \pm 22.6$ mm).

3) The final beam spot size at the Super-FRS target has to be ±1 mm in x-direction, and ±2 mm in y-direction (it should be variable).

4) The distance between the last lens and the target should be as long as possible to provide mechanical flexibility, but on the other hand the strong focus requirements must remain sufficient. As a compromise the distance was chosen to be 1.5 m.

Solution 1: Multiplet consisting of five superferric quadrupoles (pole tip flux density is less than 2 T).

The layout of the system is shown in Fig. 5.4. The first quadrupole is used to blow up the beam, which requires also a certain (rather long) drift between quadrupole Q_1 and Q_2. In the y-direction this is actually achieved by overfocusing the beam. This procedure is necessary to finally get the fine focus at the target.

	B, T	G_0, mm	L, m
Q_1	1.59	±80	2.3
Q_2	2.03	±190	2.2
Q_3	1.79	±190	2.0
Q_4	1.79	±190	2.0
Q_5	1.83	±80	2.3

Table 5.2. The quadrupole characteristics for the fine focusing system with superferric lenses.

The ultimate focusing lens is a quadrupole triplet, where the middle quadrupole is splitted into two parts in order to keep the magnetic flux density low. The total

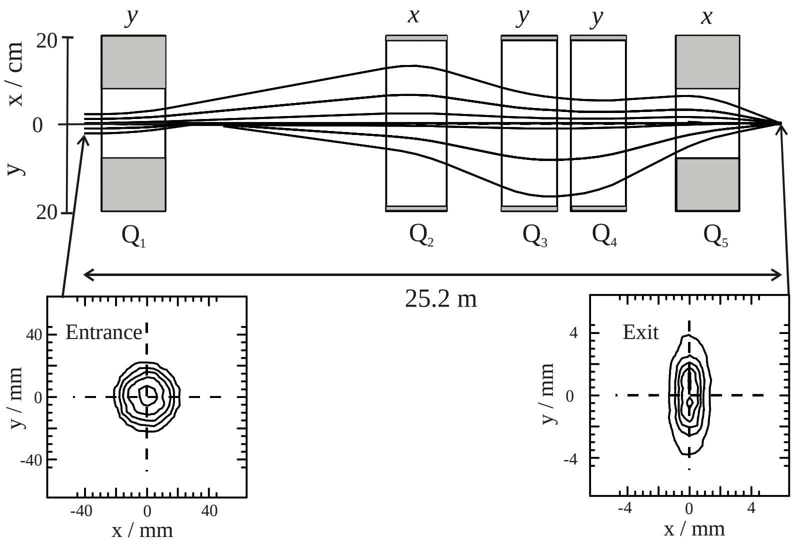

Figure 5.4: Ion optical layout of the fine focusing system consisting of five superferric quadrupoles with pole tip flux densities ≤ 2 T. The overall length of the system is 25.2 m. A final beam spot on the target of 1×2 mm^2 is achievable. ”x” and ”y” for each quadrupole indicate the focusing directions of the lenses.

length of the system is 25.2 m. The specifications of the quadrupoles are listed in Table 5.2.

Advantage of this solution is, that the same type of quadrupoles are used as in the separator (see chapter 6.3.2) even with the same gap size of $G_0 = \pm 190$ mm, such reducing construction and tooling costs.

Solution 2: Multiplet consisting of the four superconducting $\cos\theta$ quadrupoles (pole tip flux density is less than 4 T).

The layout of the system is shown in Fig. 5.5. The working principle of the system is the same as described before. The first quadrupole is used to blow up the beam and the last triplet focuses the beam to the required spot size. Because of the higher magnetic flux densities achievable with $\cos 2\theta$ quadrupoles [44] the system can be built much shorter (15.7 m).

The main parameters of the quadrupoles are listed in the Table 5.3.

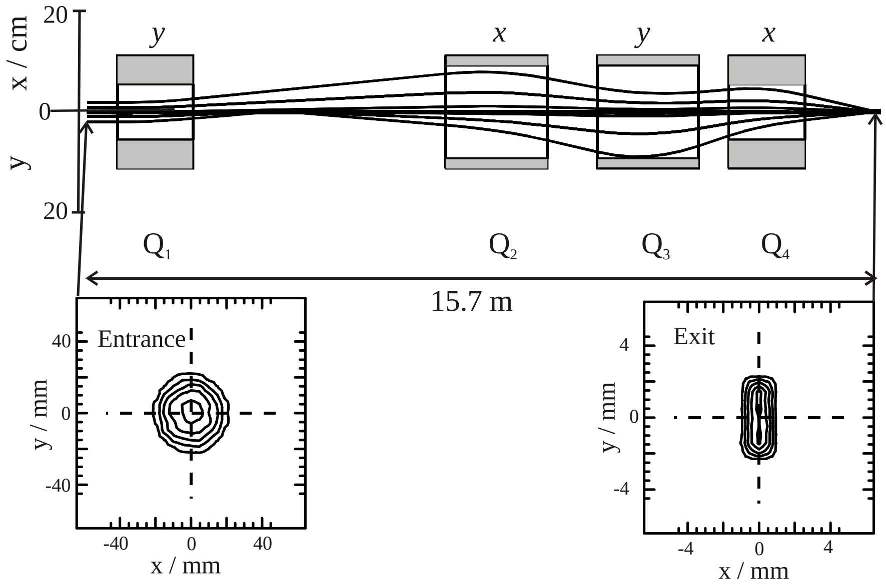

Figure 5.5: Ion optical layout of the fine focusing system consisting of four cos2µ lenses with the pole tip flux densities · 4 T. The overall legth of the system is 15.7 m.

	B, T	G_0, mm	L, m
Q_1	1.78	60	1.5
Q_2	1.84	100	2.0
Q_3	-3.37	100	2.0
Q_4	2.89	60	1.5

Table 5.3 The quadrupole characteristics for the fine focusing system with cos2µ lenses.

Operating mode at low beam magnetic rigidities

Since the lens system must work not only at high magnetic rigidities, but also at low ones (down to 10 Tm beams from the present SIS18). A solution can be implemented splitting one quadrupole into several parts, such that in the low-rigidity mode only some parts of the lenses are excited. Thus reasonably high enough magnetic flux densities are maintained over a large operation regime. Such a system is modelled for the design shown in Fig. 5.4. The first and the last lens of this multiplet are split into three 0.75 m long parts, the second lens into two 1.3 m long parts and the 3-rd and the 4-th one into three 1.3 m parts. If beams of B½ = 100 Tm are used all lenses are excited. If beams of B½ = 20 Tm are used only one part of the split lens is excited as it is indicated in Table 5.4.

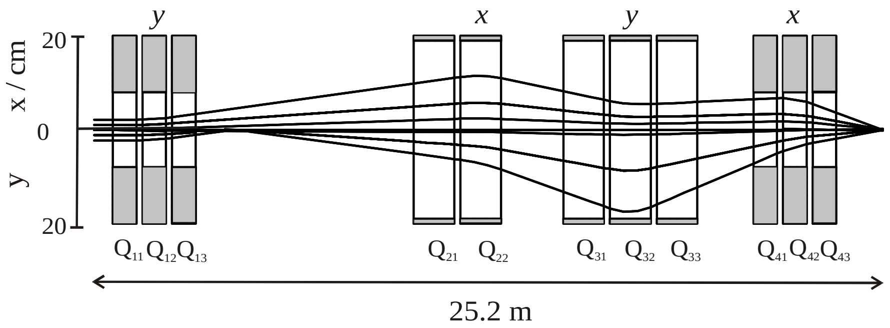

Figure 5.6: Ion optical layout of focusing system (solution 1) for the low magnetic rigidity mode.

Table 5.5 compares the quadrupole strengths if the final beam spot size in y-direction is varied from §2 mm to §10 mm.

	B (100 Tm), T	B (20 Tm), T	G_0, mm	L, m
Q_{11}	1.79	0	80	0.75
Q_{12}	1.79	0.88	80	0.75
Q_{13}	1.79	0	80	0.75
Q_{21}	1.77	0	190	1.3
Q_{22}	1.77	0.59	190	1.3
Q_{31}	1.79	0	190	1.3
Q_{32}	1.79	0.88	190	1.3
Q_{33}	1.79	0	190	1.3
Q_{41}	1.8	0	80	0.75
Q_{42}	1.8	0.89	80	0.75
Q_{43}	1.8	0	80	0.75

Table 5.4 Quadrupole excitation for the split-quadrupole system using beams of 100 Tm or 20 Tm, respectively.

	y_{foc} = §2 mm	y_{foc} = §5 mm	y_{foc} = §10 mm
B_{Q12}; [T]	-0.87	-0.47	-0.36
B_{Q22}; [T]	0.59	0.50	0.45
B_{Q32}; [T]	-0.87	-0.88	-0.86
B_{Q42}; [T]	0.89	0.98	1.00

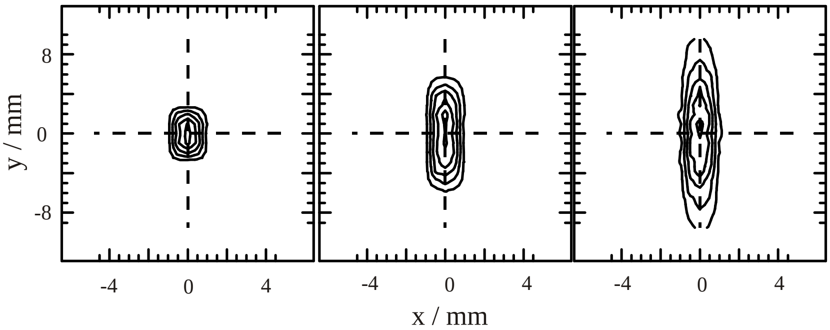

Table 5.5. Comparison of the quadrupole strengths for a variable beam spot size in y-direction (from §2 mm to §10 mm) for the split-quadrupole system using the 20 Tm rigidity beams.

5.4 Condenser lens systems

If a primary beam with a given emittance is focused onto a reaction target the secondary beam will leave the target with an increased angular distribution according to the nuclear reaction mechanism. Thus the secondary beam will occupy an enlarged phase space compared to the primary beam (see bottom left of Fig.5.7.). However, since the position of the reaction products inside the target stays almost constant this phase space enlargement of the secondary beam can be reduced if the primary beam is focused even stronger onto the target by the first part of the condenser lens system. The second part of the condenser lens system is needed to collect and to guide efficiently the secondary beam to a following fragment separator. To fulfill these requirements the condenser system must consist of lenses with a high focusing power which means focal lengths as short as possible with small apertures and high field gradients.

At intermediate energy (» 100 MeV/u) such a device, based on superconducting solenoids, is installed at GANIL and has improved the secondary beam intensity by about a factor of 50.[1] At higher energies (¼ 1000 MeV/u) the system has to be built by quadrupole lenses instead of solenoids [14]. The first part of the condenser lens system for the Super-FRS target consists of the focusing system described in chapter 5.3. The second part is build by a special collector lens consisting of a quadrupole triplet.

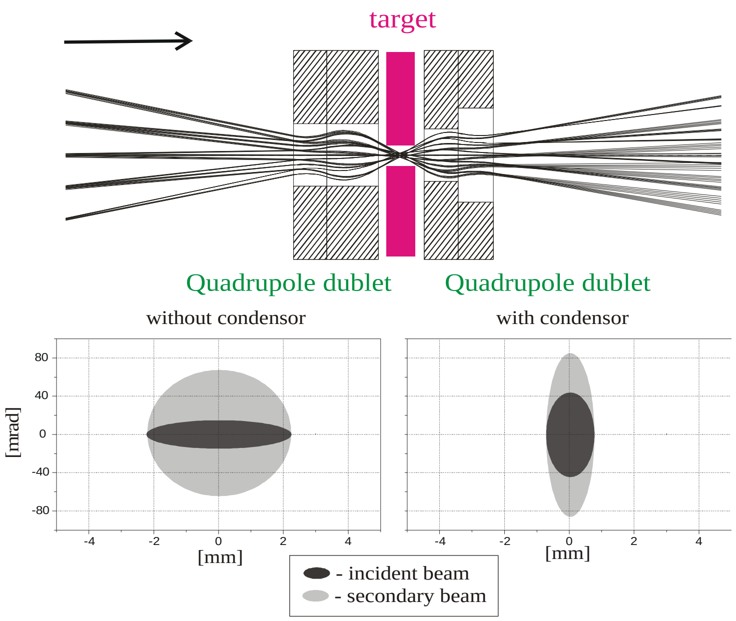

Figure 5.7: Principle of a condensor lens system (top) and the phase space enlargement of the secondary beam with and without a condensor lens (bottom). The dark area marks the emittance before the reaction and the light gray after [1].

To obtain an even higher phase density of the fragment beam one must use lenses with a much shorter focal length (in the order of few cm), which requires quadrupole lenses with very high field gradients ($g_0 \approx 1000$ T/m). Such lenses were developed and build as pulsed quadrupoles [47]. In the framework of this PhD the focusing properties of pulsed quadrupoles were tested for the first time in combination with the FRS using an ^{197}Au^{79+} beam with an energy of 650 MeV/u.

5.4.1 Front-end lens system for the Super-FRS

Considering the large phase space of exotic nuclear beams (see chapter 4 and 6.1) the collector lens system for the Super-FRS has to be installed as short as possible behind the reaction target. Since it must collect beams with large angles of divergence and high magnetic rigidity it requires quadrupole lenses with high-field gradients. Two solutions are proposed, both primarily consisting of quadrupole triplet.

The first solution is shown in Fig. 5.8. It consists of a separated quadrupole doublet and a single quadrupole lens arranged 2.7 m downstream from the doublet. This distance is necessary to provide a small beam width in y-direction at the entrance of the third quadrupole to avoid the strong defocusing of the beam and at the same time to focus the wide beam in x-direction (the more detailed fitting conditions will

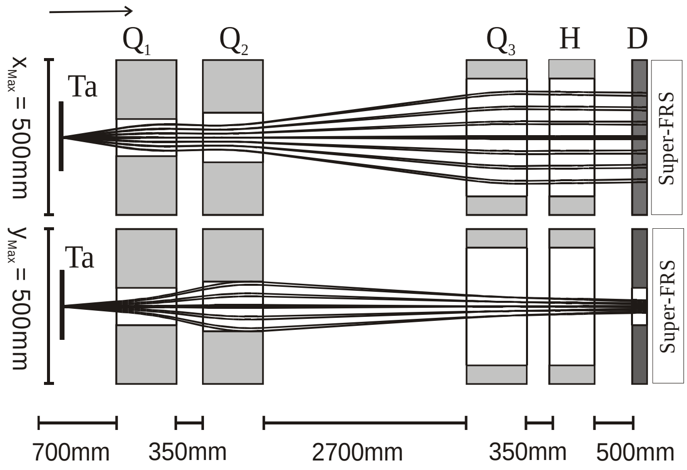

Figure 5.8: Ion optical layout of the collector system designed as a long system with the first dipole of the Super-FRS.

be given in chapter 6.2). The multiplet includes also a stand-alone hexapole, which is needed for correction of image aberrations. The characteristics of the collector system are listed in Table 5.6.

	Length / [mm]	$2G_0$ / [mm]	B_{max} / [T]
Quad 1	800	120	1.9
Quad 2	800	160	1.9
Quad 3	800	380	1.1
Hexapole	600	380	0.5

Table 5.6 Main characteristics of the ion-optical elements for the long-length collector system.

The main disadvantages of this system are:

1) Difficulty to put all magnets into one common cryostat because of the large separation distance of the system;

2) Short distance from the target to the first quadrupole lens.

3) Very high field gradients for the first two quadrupoles

An alternative solution is presented in Fig. 5.9. It consists of a compact quadrupole triplet, which can be put in a common cryostat. A hexapole correction coil is superimposed to the third quadrupole. The maximum pole tip flux density is reduced to 1.6 T, which relax the strong demands on the quadrupoles. Also the distance from the target is increased to 1.0 m. The angular acceptance is slightly decreased compared to the first solution, however, it still fulfills the design goals of the Super-FRS (see chapter 6). The specifications of the system are listed in Table 5.7.

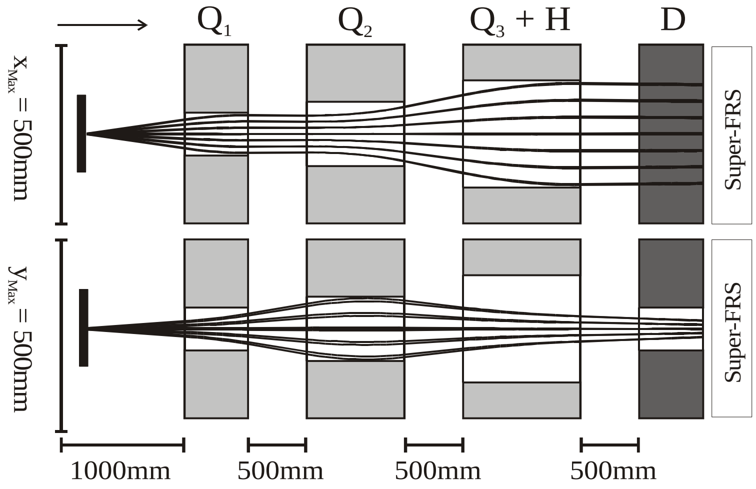

Figure 5.9: Ion-optical layout of the short length collector system with the first dipole of the Super-FRS.

	Length / [mm]	$2G_0$ / [mm]	B_{max} / [T]
Quad 1	650	120	1.5
Quad 2	1000	180	1.6
Quad 3	1200	300	1.1

Table 5.7. The main characteristics of the ion-optical elements for the short-length collector system.

The new facility will work with very high beam intensities, which leads to a huge radiation level around the target area and the first dipole (where the primary beam is stopped). Thus using superconducting magnets there could cause problems in sense of quenching (going from superconductivity state to normal conducting) but also in sense of long term radiation damage. For this reason also one collector system is designed using only normal conducting quadrupole lenses (i.e. the maximum magnetic flux density is kept to $B = 1$ T). The losses in transmission in this design is about10% compared to the superconducting one. The specifications of this system are listed in Table 5.8.

	Length / [mm]	$2G_0$ / [mm]	B_{max} / [T]
Quad 1	900	120	1.0
Quad 2	1600	220	1.0
Quad 3	1000	300	1.0

Table 5.8. The characteristics of the normal conducting collector system.

5.4.2 Pulsed quadrupoles for condenser lens systems of short focal length

Conventional iron-dominated quadrupole lenses are limited by the saturation of the ferromagnetic material and thus the flux density $\vec{B}$ at the quadrupole pole tip is usually lower than 1.0 T. To achieve lenses with a shorter focal lengths higher flux densities of the quadrupole are necessary.

For some cases pulsed magnetic quadrupole lenses have been proposed that could focus high energetic ion beams during short time intervals of ~10 μs [48]. The average energy dissipation for relatively low repetition rates in such lenses is small, so that conventional copper wires can be used for the coils. Such quadrupoles have a simple and compact structure in which we have achieved field gradients of more than 1300 T/m in the tested prototypes.

Construction of pulsed quadrupole lens

Since the saturation effect of steel limits the magnetic flux density in the quadrupole aperture, the coil of pulsed magnetic quadrupole should be built in an iron-free structure (Fig. 5.10.). To provide a stable operation the coils are fixed with epoxy resin. In addition they are protected from inside and outside with stainless steel tubes [47].

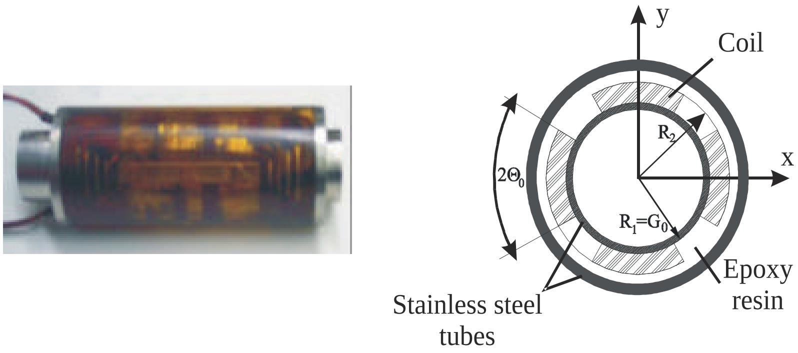

Figure 5.10: Photo of the pulsed magnetic quadrupole prototype and schematic view of the quadrupole in transversal cut

These tubes prevent possible radial mechanical deformations or even the destruction of the current leading coils due to Lorentz forces acting in the region of extremely high magnetic flux densities and at the same time they allow also to provide additional cooling. Evidently the eddy currents induced by the time-varying magnetic field in the conducting tubes would reduce the resulting magnetic flux density on the aperture. But for pulse duration of T >100 μs and using stainless steel tubes with a thicknesses of 1 mm or 2 mm this effect may be neglected because of their low electrical conductivity.

The detailed description of the construction and the properties investigation of such a quadrupole are done in ref. [47], also with the off-line experimental results and field quality investigations. Here the focusing characteristics of the pulsed magnetic quadrupole which was tested on-line with heavy ions beam will be described.

Electrical circuit and field quality

The electrical circuit consists of the high current pulse generator, the transfer line, the quadrupole and the measurement devices (see Fig 5.11). An input voltage of 220 V is raised through a variable-ratio step-up transformer up to 3 kV and then rectified by a high voltage diode to become a DC current for charging a capacitor (C) of 820 μF. The charge time was found to be 3 seconds until the total energy of up to 8 kJ being stored in the capacitor.

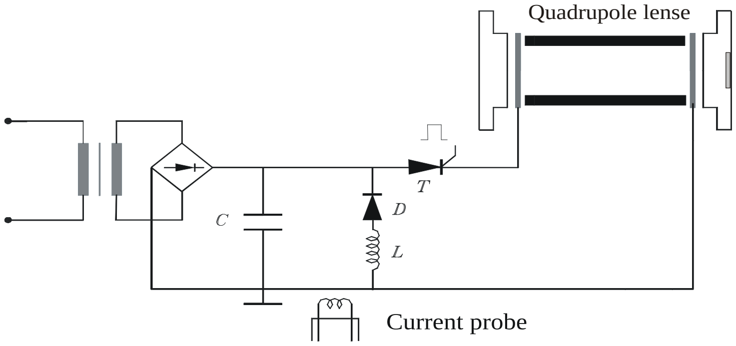

Figure 5.11: Electrical circuit consisting of the pulse generator and the quadrupole.

The high current through the quadrupole is controlled by a power thyristor (T) with a maximal current rating of 34 kA. Due to the oscillatory nature of the circuit, the capacitor is recharged by converting the magnetic energy in the quadrupole; however, now with the opposite polarity. To distribute this energy optimally, a special return path for the current through a diode (D) and an additional coil (L) was installed. The inductance of the coil was chosen to be large enough to significantly reduce energy losses during the recharging process.

The magnetic flux densities in a quadrupole aperture was measured by a computer controlled inductive probe which is a thin coil of 1 mm diameter connected to an integrating amplifier. With such a probe it is possible to measure the flux density distribution on the aperture with a precision of about 3%. A current transformer was used to control the waveform of current pulses. A typical signal of this transformer is shown in (Fig. 5.12.).

Several types of quadrupoles were built in order to investigate the influence of the various design parameters on the maximal achievable flux density and on the field

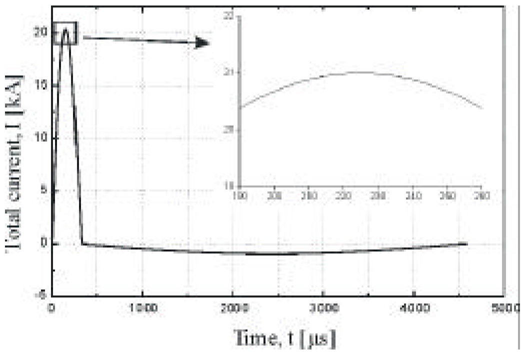

Figure 5.12: Typical signal of the discharge current measured with the current transformer [47].

quality in the quadrupole. Fig. 5.13. for instance shows the x-component of the magnetic flux density B_x measured in the radial direction for two different quadrupoles. Typically the measurements differed by ~3% from theoretical calculations. However, one can expect that the real field quality is even better since the observed discrepancy is partially due to the errors of positioning of the inductive probe.

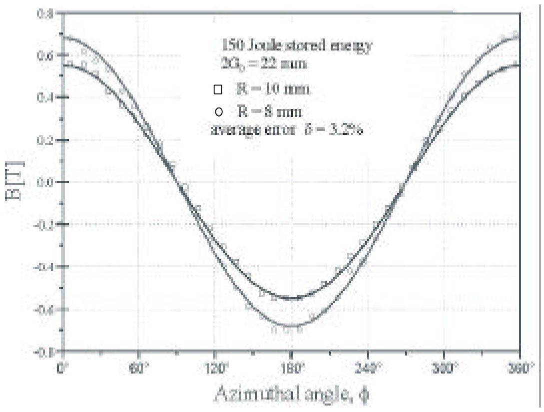

Figure 5.13: B_x component of the magnetic field measured along the azimuthal direction of a quadrupole. Measurements were performed at two different radii.

On-line experiment at the FRS

To test the focusing properties of a pulsed quadrupole an on-line experiment was performed at GSI. The quadrupole was placed at the F4 final focal plane of the FRS. The separator was operated in the standard mode, i.e. a dispersion of -6.82 cm/% at F2 and no degrader was used. A scintillator screen was installed ¼300 mm

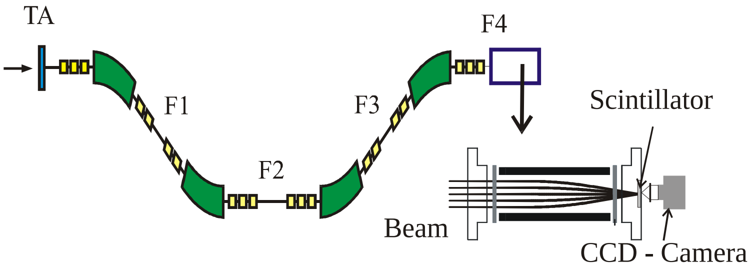

Figure 5.14: The experimental setup shows the FRS together with the pulsed quadrupole.

downstream of the pulsed quadrupole lens and monitored by a CCD camera (see Fig. 5.14).

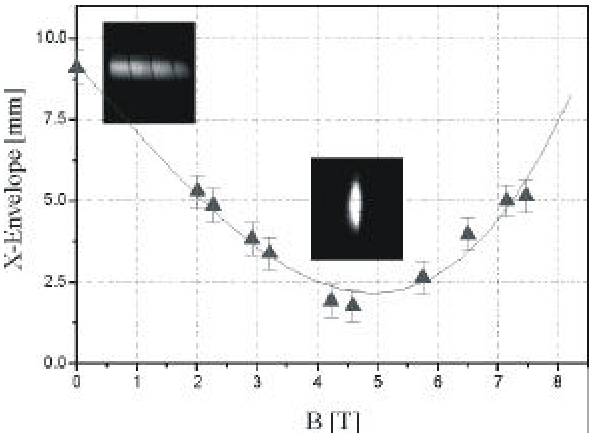

Figure 5.15: The size of the beam envelope in horizontal plane for different quadrupole field strengths.

In the experiment we used a ^{197}Au^{79+} heavy ion beam with an energy of 650 MeV/u which corresponds to a magnetic rigidity of 10.5 Tm. The magnetic field in the quadrupole aperture was varied by changing the voltage of the pulse generator from 0 V to 2.5 kV. For each voltage the resulting beam profile was measured on the scintillator screen. The smallest beam size was observed at a charging voltage of 1.4 kV of the capacitor which corresponds to a peak current of about 11 kA and a magnetic flux density of 4.65 T, respectively. The beam with an initial width of §10 mm in horizontal direction was focused to §2.5 mm which corresponds to the minimum possible beam diameter for the given beam phase space. Applying higher charging voltages led to an overfocusing of the heavy ion beam as shown in Fig. 5.15

Chapter 6

Design of the Super - FRS

At the beginning of the design of any ion optical system the dimensions of all elements, such as bending magnets, quadrupole lenses and higher order correcting elements can usually be chosen from technically feasible types. To obtain finally a system that fulfills the given requirements one has to choose a suitable arrangement of all magnets taking into account all experimental as well as technical constraints. In a second step the fulfillment of the ion optical properties of the system requires an iterative approximation procedure, which is carried out with the help of a number ion-optical programs, such as GICO [49], COSY INFINITY [50], GIOS [51], MIRKO [52] and others.

The main design goals of the planned projectile fragment separator, Super- FRS, are the following:

1.) Large momentum and angular acceptance for all projectiles produced via fragmentation and fission reactions.

2.) Separation of the projectile fragments in A and Z with a low amount of unwanted species of nuclides.

3.) Transport to the experimental areas and injection into the collector and storage rings of the separated particle beams with high efficiency.

Together with the design goals the following parameters were decided to keep fixed:

1) operating magnetic rigidity: $B\rho$ up to 20 Tm.

2) resolving power at the dispersive midplane of the separator: 1500.

6.1 Design goals

As it was pointed out already in chapter 4 the exotic nuclear beams produced by projectile fragmentation and especially by projectile fission will have a large phase space occupation. In Fig 6.1 phase space calculations of relativistic ^{132}Sn and ^{100}Sn, produced by ^{238}U projectile fission and ^{124}Xe fragmentation, respectively, are compared. Simulations were done using the MOCADI code [53]. The calculations assume a realistic target thickness, which was optimized to obtain highest count rates at the final focal plane of a high-acceptance fragment separator.

Especially the transmission of fission fragments through the Super-FRS should be increased considerably compared to that of the FRS, which is only a few percent (i.e. less than 5% for elements with $Z < 50$). The acceptance window indicated by the thick lines in the right-hand panel of Fig. 6.1 reaches a pure ion-optical transmission of more than 60% for medium mass fission fragments and still 30% for light mass fission fragments, which is at least one order of magnitude more compared to the FRS. The acceptance window corresponds to a maximum momentum acceptance of the Super-FRS of dp=p = §2:5 % and 40 ¼ mm mrad (x_0 = §1 mm, a_0 = §40 mrad and y_0 = §2 mm, b_0 = §20 mrad).

The resolving power of the separator should be R = 1500: This is the same as for the FRS, which was proven in many experiments to be an appropriate value. The achievable resolving power of an ion-optical system is directly connected to the beam emittance and the used magnetic volume of the dispersive elements (see Eq. 2.39). Taking into account technical side constraints the acceptable beam emittance in the dispersive plane of the Super-FRS is determined to be $"_x$ = 40 ¼ mm mrad, and thus the object size on the target should be x_0 = §1 mm.

The Super-FRS should also in y-direction accept a beam with an emittance of $"_y$ = 40 ¼ mm mrad, but now with a somewhat larger object size on the target of y_0 = §2 mm. There are two reasons for it:

1) The beam spot area on the target should not be too small [3] in order not to destroy the target by bombarding it with the high intensity primary beam;

2) The first quadrupole lens right after the target can focus the beam only in one plane (here the x-plane), but it defocuses the beam in the perpendicular plane. Thus the beam should have smaller angles of divergence in this plane in order not to loose it already in the first lens.

The Super-FRS should be operated with a maximum magnetic rigidity of B½ = 20 Tm, which was already concluded by the limitations of the energy operation domain in chapter 4.3.2. Table 6.1 summarizes the design goals of the Super-FRS.

Beam rigidity	up to 20 Tm
Energy, max. for U^{92+}	1,5 GeV/u
acceptance $"_x$	§(1 £ 40 ¼ mm mrad)
acceptance $"_y$	§(2 £ 20 ¼ mm mrad)
momentum width, ¢p=p	§2.5 %
Resolving power, R	1500

Table 6.1. The design parameters of the Super-FRS [54].

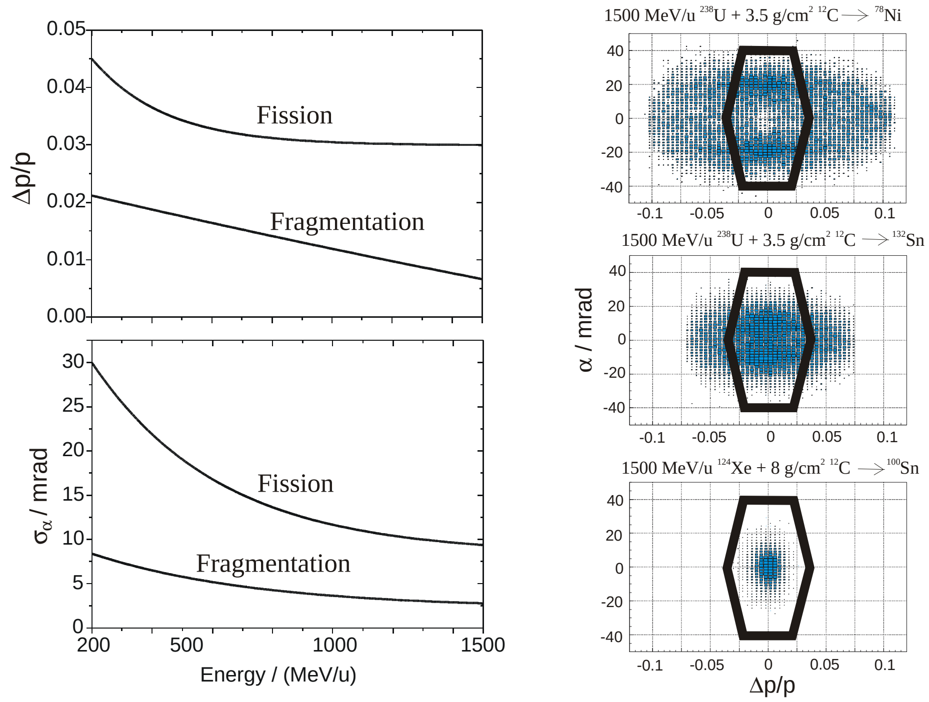

Figure 6.1: Left panel: Standard deviations of the momentum and angular distributions for ^{132}Sn and ^{100}Sn fragments produced via ^{238}U projectile fission and ^{124}Xe fragmentation, respectively. Compared to Fig. 4.3 the calculations are done for the production targets optimized for the acceptance of the Super - FRS. Right panel: Angular and momentum spread of ^{78}Ni and ^{132}Sn fission fragments compared to ^{100}Sn projectile fragments. The fission products are created with 1500 MeV/u ^{238}U projectiles in a 3.5 g/cm^2 carbon target and ^{100}Sn is produced with 1500 MeV/u ^{124}Xe in a 8 g/cm^2 carbon target. The thick contour line represents the acceptance of the Super - FRS.

6.2 General layout and 1st order optics of the standard achromatic mode

The Super-FRS is a two stages separator - a pre-separator and a main separator - each equipped with an energy degrader stage (Fig. 6.2). It has altogether six independent "cells" - two for the pre-separator and four for the main separator - each consisting of a 28^0-degree dipole magnet and a set of quadrupole lenses in front and behind each dipole to fulfill the ion optical requirements. In the standard mode the pre- and main-separator are operated as achromatic systems, and hence the complete system is also achromatic. The cells include also higher order multipole lenses. There purpose

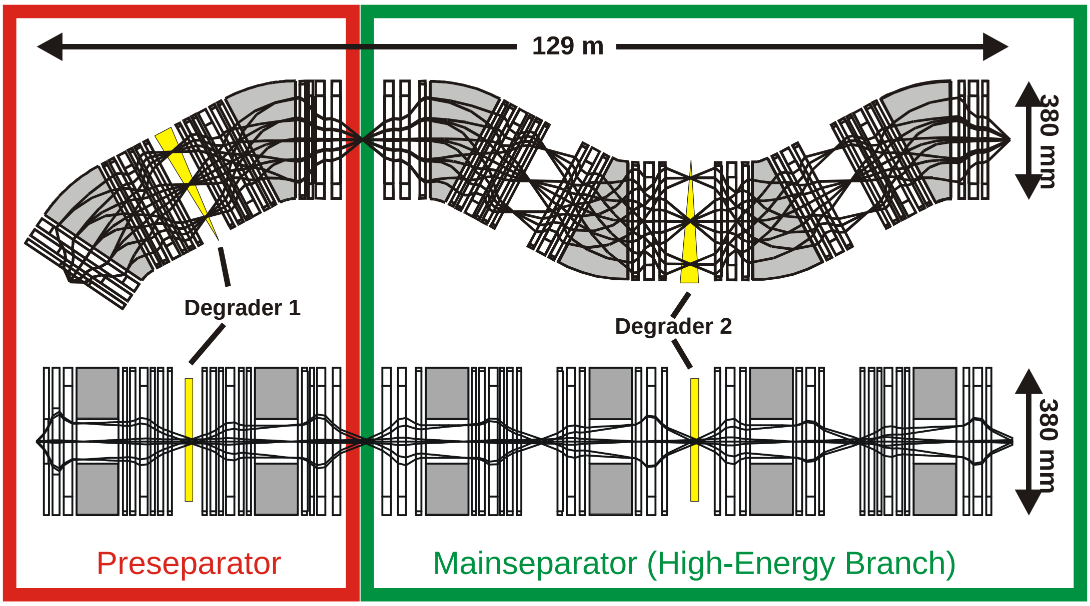

Figure 6.2: The layout of the Super-FRS consisting of the pre- and the main separator. The overall length of the system is 129 m. Trajectories are drown for beams with an emittance of $\pm 40\,\pi$ mm mrad in x- and y-directions and a momentum spread of $\pm 2.5\%$.

will be described in Chapter 7.

The design studies of the Super-FRS include two different ways to arrange the pre-separator, which are:

1) Pre- and main separator have the same plane of deflection (so-called "horizontal" design of the pre-separator). It is assumed that the separator is positioned on ground level;

2) Pre-and main separator have an ortogonal planes of deflection ("vertical" pre-separator). In this design it is assumed that the production target is placed at SIS100/200 level (-24 m) and the pre-separator is used simultaneously to transport the beam to ground level (level of the main separator).

6.2.1 The Super-FRS using a "horizontal" pre-separator

The layout of the Super-FRS and its 1st order imaging conditions are presented in Fig. 6.3. The envelopes and the dispersion line are plotted for 40 π mm mrad and 2.5%, respectively. The ion-optical plot shows the image conditions in x-direction, the dispersive plane, and in the perpendicular coordinate, y-direction. The quadrupole magnets are necessary to guide the fragment beam, to achieve the required resolution by proper illumination of the dipole magnets, and to focus the beam at the different image planes.

In the achromatic mode a point-to-point focusing in x-direction is required at all six focal planes (i.e. F1...F6) while waists (images) in y-direction are required at the focal planes F1, F2, F4 and F6. For the focal planes F3 and F5 there are no strong requirements to have an images in y-direction. The achromatic condition at the exit of the pre-separator (F2) and at the final focal plane (F6) is realized by requiring that both the image size and the angular divergence are independent to first order of the momentum spread of the incident beam (i.e., (xj±) = 0; (aj±) = 0). Fig. 6.3 includes all 1st order fit conditions at the focal planes, while in Table 6.2 the most important 1st order matrix elements at the central and final focal plane of the pre-separator (F1, F2) and the main separator (F4, F6) are listed.

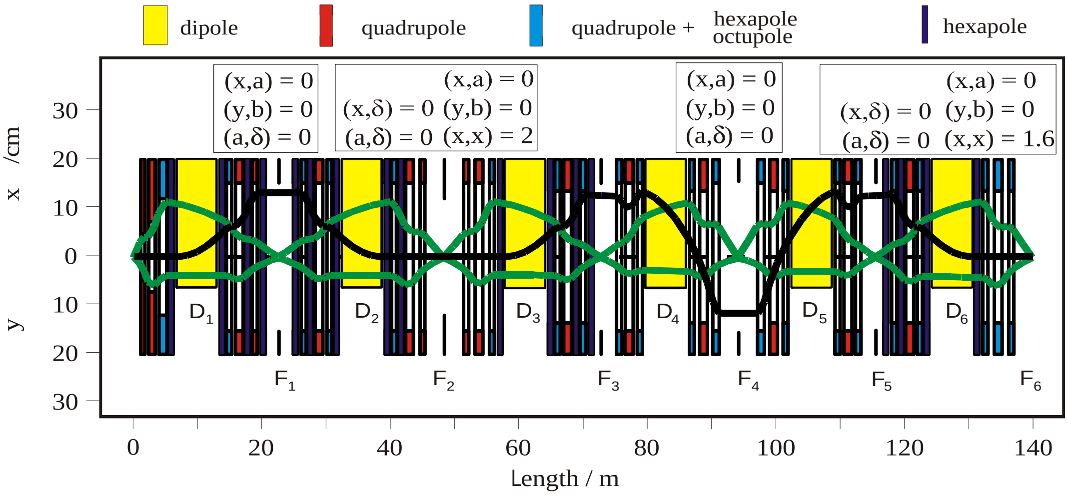

Figure 6.3: Ion optical elements, beam envelopes and the dispersion line for 2.5% momentum deviation. The envelopes result from an emittance of 40 ¼ mm mrad in x and y directions. The 28 degree magnets are indicated by D_1- D_6 and the different focal planes by F_1 - F_6. Quadrupole triplets are placed in front and behind each dipole magnets to achieve the desired ion-optical conditions at the focal planes and to properly illuminate the dipole magnets. Also indicated are the 1st order fitting conditions at the midplane and the final focal plane of the pre-separator as well as of the main separator [54].

The dipole magnets are illuminated, such that the required resolving power of R ¼ 1500 is achieved. This leads to fitting conditions as shown in Fig. 6.4. A monoenergetic beam has a size of x_{in} ¼ 140 mm at the entrance of the dipole and x_{out} ¼ 100 mm at the exit of the dipole (left side of Fig. 6.4). For a beam with a momentum spread of ¢p=p = §2:5 % the picture change as shown on right side of

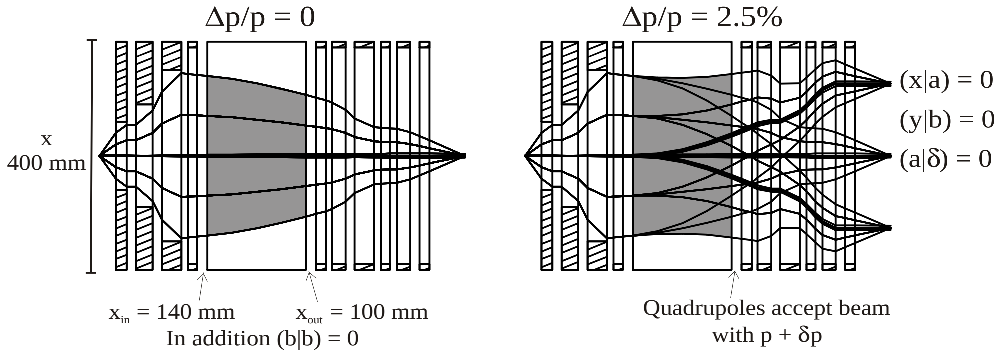

Figure 6.4: Fitting conditions for proper dipole illumination.

Fig. 6.4. Now the illuminated area of the dipole is rectangular and the beam with maximum momentum spread can still be accepted by the following lens system.

In order to provide the ion optical mode in y-direction two approaches are proposed:

1) to have the beam focused inside each dipole (i.e. (yjb) = 0).

2) to keep the beam "parallel" inside the dipole gaps (i.e (bjb) = 0) (see Fig. 6.5).

Matrix elements	at F$_1$	at F$_2$	at F$_4$	at F$_6$
(xjx)	-3.28	2.00	1.46	1.60
(xja); [m=rad]	0	0	0	0
(xj±$_p$); [m]	5.05	0	-4.48	0
(ajx); [rad=m]	0.25	-0.59	-0.68	-0.66
(aj±$_p$); [rad]	0	0	0	0
(yjy)	-2.55	1.90	2.84	1.94
(yjb); [m=rad]	0	0	0	0
(bjy); [rad=m]	0.12	-0.21	-0.36	-0.67

Table 6.2. Calculated first order transfer matrix elements at the focal planes F1 (central focal plane of the pre-separator), F2 (exit of the pre-separator), F4 (central focal plane of the main separator) and F6 (final focal plane of the main separator) of the Super-FRS. The momentum deviation in parts of the nominal value.

Fig. 6.6 indicates that a parallel beam in y-direction in the dipole has several advantages. The beam transmission will increase with increased gap size, while it is approximately constant if an intermediate focus in the dipole is fitted (right side of Fig. 6.6). In case the initial y-spot size has to be larger than ¾$_y$ = 2 mm (in order not to destroy the target) the beam transmission stays almost constant if the beam is parallel in the dipole (up to ¾$_y$ ¼ 10 mm) while in the other case the transmission

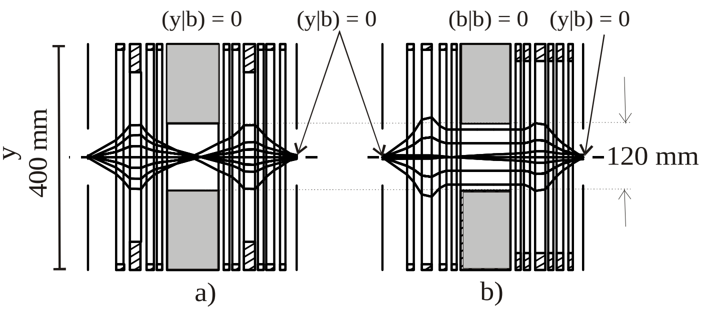

Figure 6.5: One cell design using the mode with images inside the dipoles (left) and 'parallel' mode (right).

drops to » 50% (left side of Fig. 6.6). This happens because in the parallel mode the width of the position distribution inside the magnet in y-direction is specified mainly by the initial angular distribution but not an initial width of the beam.

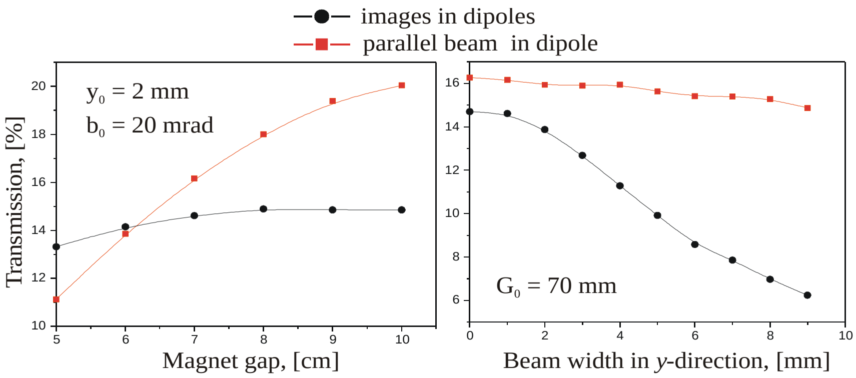

Figure 6.6: Beam transmission through the separator (at F6) as a function of the dipole gap size (left) and the initial y-beam spot size (right). Calculations are done for the two ion-optical modes described in Fig. 6.5, i.e having the beam parallel in the dipole (red lines) or having an additional images in the dipole (black lines). The calculations were done for the ^{78}Ni fragment produced via fission of ^{238}U in 3 g/cm^2 Be target with the energy of 1000 MeV/u. All other elements in the system (quadrupoles, hexapoles) have fixed parameters for both cases.

The Super-FRS is a versatile ion optical system, that is why other optical modes are possible besides the standard achromatic mode. Some examples will be given later in the Chapter 6.6.

6.2.2 The Super-FRS using a "vertical" pre-separator

It was also considered to have the high-power production target placed underground, i.e. at -24 m, the same level like the synchrotrons SIS100/200. In this case the pre-separator will not only be used to get rid of the primary beam and bulk of unwanted fragments, but it will transport the beam to ground level. Fig. 6.7 shows the topology of this solution and Fig. 6.8 compares the ion-optical design for the "horizontal" and the "vertical" pre-separator.

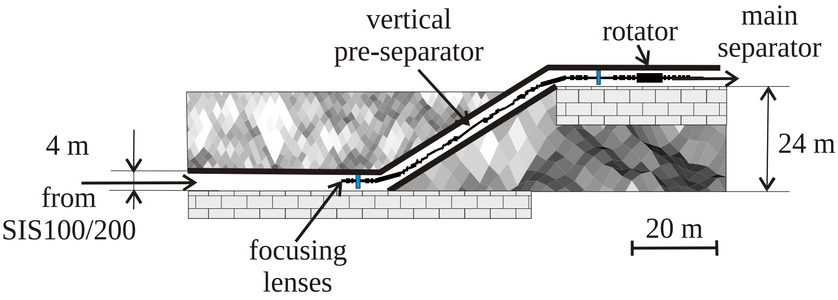

Figure 6.7: The topology of a "vertical" pre-separator.

In case of a "vertical" pre-separator two intermediate images between the dipoles are necessary, in order to keep the achromatism of the system. This requires at least one quadrupole triplet more. Actually two quadrupole triplets are needed in addition in order to overcome the 24 m difference in altitude and not to loose in transmission.

The pre-separator and the main separator are connected by a beam rotator. It's purpose is to couple the dispersive planes of the pre-separator and the main separator in a proper way. The rotator is built by seven quadrupole lenses (see Fig. 6.9). This multiplet is a telescopic system, which means that it has point-parallel and parallel-point focusing properties at the midplane and point-point and parallel-parallel properties at the end of the multiplet. The rotator does not really rotate the beam by 90 degree but it mirrors the planes as it was described before. The ion-optical properties of the rotator are shown in the Table 6.3.

	before rotator	after rotator
(xjx)	-2	2
(xja); [m=rad]	0	4¢10$^{¡3}$
$(xj\pm_{p})$; [m]	0	0
(yjy)	-2.08	-2.08
(yjb); [m=rad]	0.18	0.17
$(yj\pm_{p})$; [m]	0	0

Table 6.3. The main 1^{st} order transfer matrix elements of the rotator system

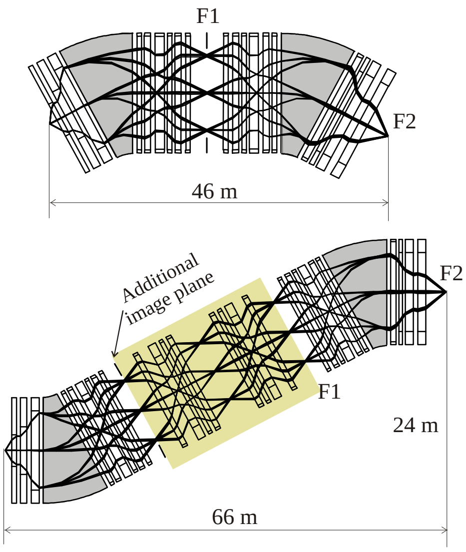

Figure 6.8: Comparison of the ion-optical design of the "horizontal" pre-separator (upper part, top view) and the "vertical" pre-separator (lower part, side view). The "horizontal" design is as compact as possibble and includes the energy degrader stage at the midplane F1. In the "vertical" design a second intermediate image guarantees the achromatism of the system. To keep the required beam transmission the "vertical" pre-separator has to be equipped with 2 additional quadrupole triplets.

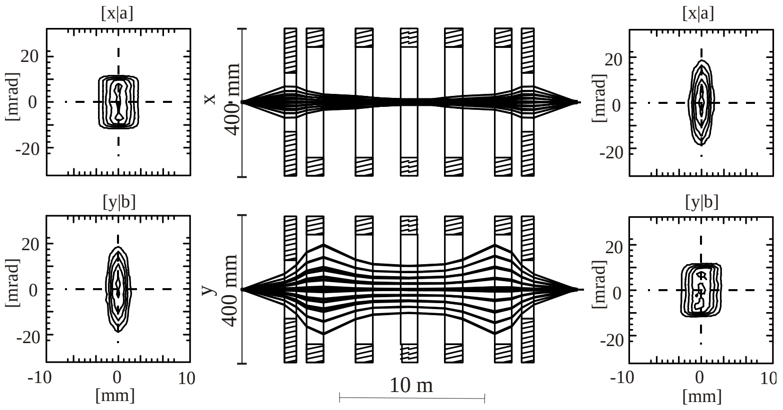

Figure 6.9: The ion optical layout for the rotator. The rotator is a multiplet of seven quadrupoles. The trajectories are drawn for the beam with the emittance of 40 ¼ mm mrad and the momentum spread of 2.5 %.

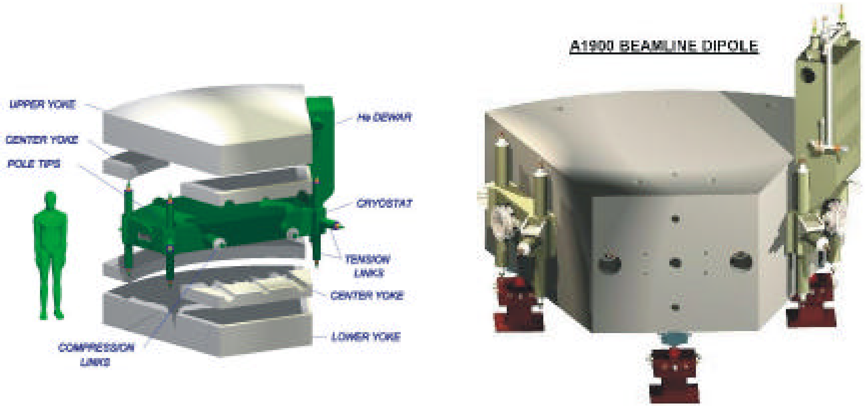

Figure 6.10: The schematic view of the running dipole magnet at A1900 at MSU [55].

6.3 Magnetic elements for the Super-FRS

6.3.1 Bending magnets

The system includes six identical homogeneous bending magnets with 28^0 degree deflection each. The radius of beam deflection was chosen to be 12.5 m, thus the magnetic flux density is limited to 1.6 T for beams with a maximum magnetic rigidity of 20 Tm. The maximal width of the ion beam inside the magnet is §0:15 m, and the inner height of the vacuum chamber is assumed to be §0.07 m. No inclination of the entrance and exit field boundaries is implied in the design. Due to the moderate flux density needed the magnet could be built in standard technology using normal conducting coils. However, considering the large gap of the dipole the magnets will require a huge power consumption (for the FRS this number is » 1 MW). In order to save operating costs it is therefore considered to use superconducting magnets.

	A1900	**Super-FRS**
Radius of deflection (m)	3.0	12.5
Angle of deflection (°)	45	28
Magnet air gap (mm)	90	140
Maximal flux density (T)	2.0	1.6

Table 6.4. Comparison of the main specifications for A1900 and Super-FRS dipole.

Superconductivity and cryo-technique will be necessary for the new accelerator complex. Actually the dipoles for the Super-FRS should be built as superferric magnets, like e.g. the dipole magnets for the A1900 separator (ref. [55] see Fig. 6.10). These are iron dominated magnets, i.e. the field will be shaped by the iron yoke, but the coils are superconducting. Table 6.4 compares the main specifications for A1900 and the Super-FRS dipole.

6.3.2 Quadrupole lenses

As can be seen from the Table 6.5 the Super-FRS requires four different type of quadrupoles. Type I and II have rather high field gradients in the order of up to $g \approx 25$ T/m and are installed right after the high-power production target. Type III and IV have very big apertures (up to $G_0 = \pm 190$ mm) to guarantee the transmission of large phase-space beams with high momentum spread. Also they need a magnetic flux density up to $B_{max} \approx 1.9$ T. these requirements make the use of superconductivity indispensable (but also from the point of view of operating costs).

At the moment it is foreseen to built also the quadrupoles as superferric lenses, i.e. iron dominated but using superconductive coils. The same type of quadrupoles are already operated at the A1900 separator at NSCL, MSU ref. [56], however, those lenses are much shorter because of the lower rigidity of the beams of only $B\rho \approx 6$ Tm.

Element		Quant.	l / [mm]	$2G_0$ / [mm]	B_{max} / [T]
Dipole	$\varphi_0=28^o$	6		140,0	1,6
	$\rho_0=12.5$ m				
Q-pole	-Type I	1	650,0	120,0	1,6
	-Type II	1	1000,0	180,0	1,6
	-Type III	14	1200,0	340.0	1,5
	-Type IV	20	800,0	380.0	1,8
H-pole	-magnet	13	600,0	380,0	0,6
	-coil I	1	1200,0	340,0	0.1
	-coil II	9	800,0	380,0	0.1
O-Pole	-coil I	2	1200,0	340,0	0,1
	-coil II	14	800,0	380,0	0,2

Table 6.5. The quadrupole lenses specifications required for the Super-FRS.

To built a cost-effective system a set of lenses, i.e. a quadrupole triplet, should be assembled together (Fig. 6.11) using a common cryostat. For this purpose it is of advantage to use only such quadrupole configurations as indicated on the left side of Fig. 6.12, where the vacuum chamber is shrank at the most on one side.

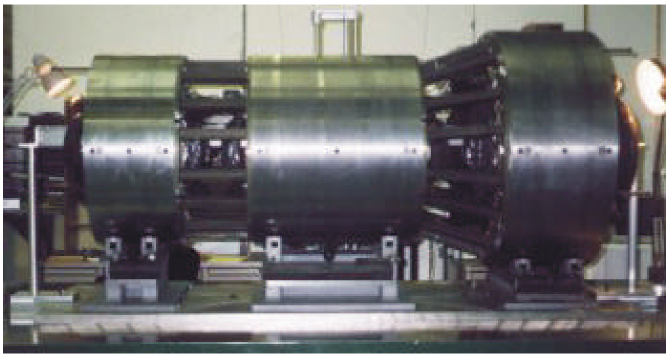

Figure 6.11: Superferric quadrupole triplet at the A1900 at MSU. The triplet consists of two types of quadrupoles with different apertures [56].

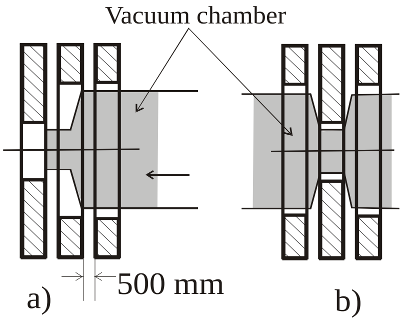

Figure 6.12: The only quadrupole configurations as shown on the left side should be used (vacuum chamber is shrinked on one side). The solution on the right side is technically much more difficult to realize.

6.3.3 Higher-order multipoles

Correction of higher-order aberrations is very important for the Super-FRS and it will be discussed in chapter 7. It is planned to use hexapole as well as octupole correctors. These either can be inserted in quadrupoles, like at the A1900 separator ref. [55], or stand spacially separated.

The multiplet inserts are surface coils installed in the circular aperture of the quadrupole, simulating a $\cos(3\phi)$ (hexapole) or $\cos(4\phi)$ (octupole) field distribution, which is superimposed to the quadrupole field.

The stand alone version is simply the inserts with a round yoke on the outside for the return path.

6.4 Separation performance with two degrader stages

Based on the experience of spatial isotopic separation with the FRS, the Super-FRS uses also the $B\rho - \Delta E - B\rho$ method where a two-fold magnetic rigidity analysis is applied in front of and behind a specially shaped energy degrader. The strong enhancement of the primary beam intensity expected with the SIS100/200 synchrotron requires additional measures to preserve the excellent separation quality of the FRS. The higher primary beam intensity causes also correspondingly higher production rates of parasitic fragments in the degrader, which may be of comparable intensity to those produced presently at the FRS production target. A solution of this problem is an additional degrader stage which provides an effective preselection before the fragmented beam impinges onto the main degrader. So, the Super-FRS consists of a two-stage magnetic system, the pre- and the main-separator, each equipped with a degrader. The two-stages system can provide the following properties of the Super-FRS:

1) reduction of the unwanted fragments produced in the degraders.

2) optimization of the fragment rate on the detectors in the main part of the separator.

3) introduction of another separation cut in the N-Z plane of the separated isotopes as it described in Chapter 3.

The separation performance of the Super-FRS is illustrated in Fig.6.13. MOCADI calculations show the separation quality for two doubly-magic tin isotopes, ^{100}Sn and ^{132}Sn. A 1500 MeV/u ^{238}U primary beam reacts with 3.5 g/cm^2 carbon target and produces ^{132}Sn ions via projectile fission. The area of the isotopes in the N-Z plane represents the corresponding intensities at the different focal planes F_1, F_2 and F_6. ^{100}Sn ions are produced via projectile fragmentation of ^{124}Xe beam. The energy of ^{124}Xe projectiles was chosen to be 1500 MeV/u and the thickness of the carbon production target was 7.9 g/cm^2, which is the optimum target thickness for corresponding beam energy. The band of parasitic fragments at F_1 is much broader in case of fission due to the reaction kinematics (see Chapter 4.2.2). Therefore, also in the final focal plane F_6, the number of contaminants is higher compared to the fragmentation reactions.

Together with the reduction of the number of unwanted fragments each degrader also populates the secondary contaminants which will be not separated in the conventional one-degrader separation method. In Fig. 6.14 the effectiveness of the two-degrader separation method is demonstrated for ^{100}Sn isotopes produced via fragmentation of ^{124}Xe projectiles at 1000 MeV/u. All the shown secondary fragments inevitably pass through the separator in the selected ^{100}Sn setting, whereas the rest of the contaminants are completely removed using two degrader stages.

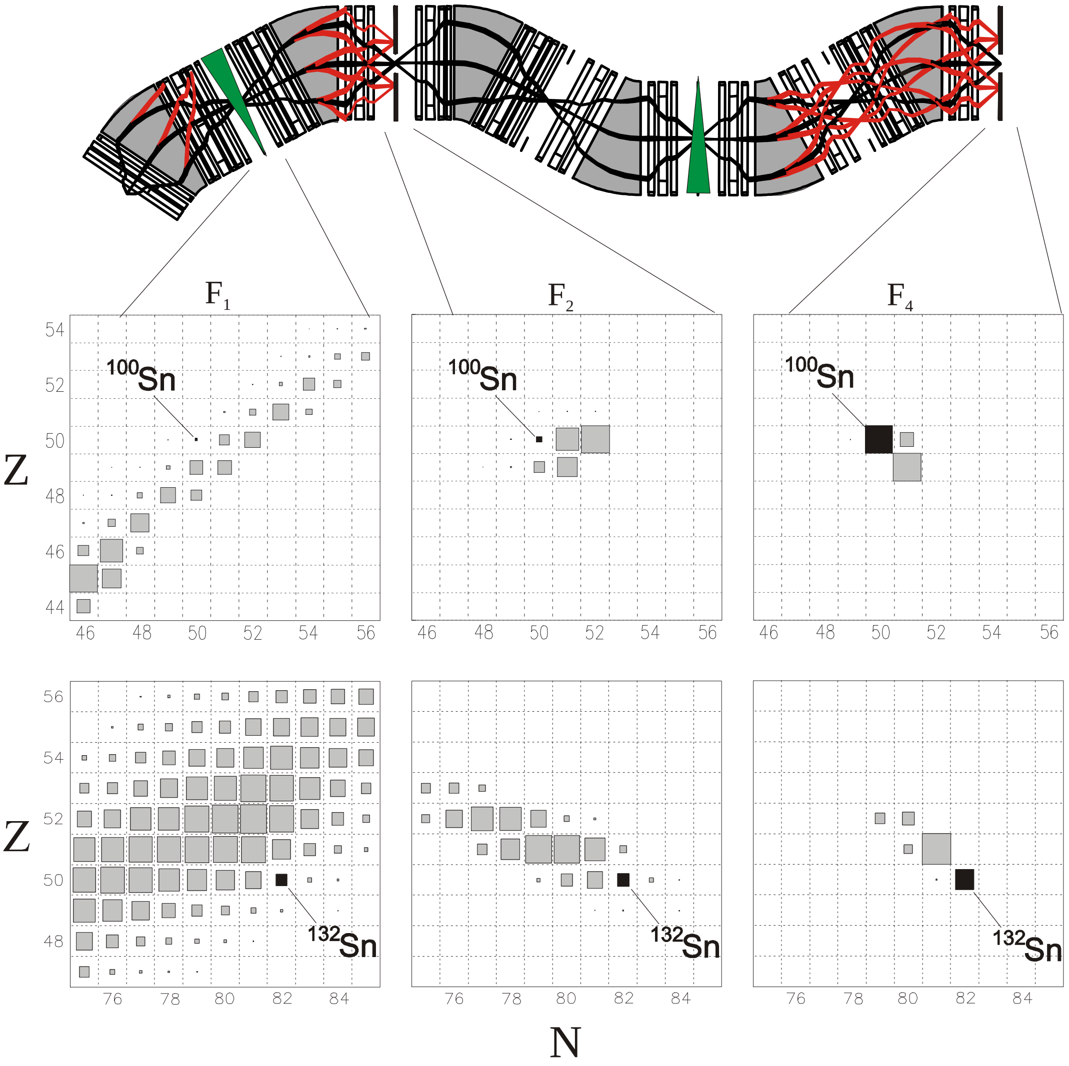

Figure 6.13: Separation performance of the Super-FRS for two doubly-magic nuclei ^{100}Sn and ^{132}Sn. ^{100}Sn is produced via fragmentation of ^{124}Xe and ^{132}Sn via fission of ^{238}U projectiles. The incident energy of both projectiles was 1500 MeV/u. In both cases the optimum target degraders thicknesses (d_1=r_1 = 0:3 and d_2=r_2 = 0:7) were selected in the pre- and main stages, respectively. d=r represents the degrader thichkness in units of the range corresponding the energy of the fragment in front of the degrader.

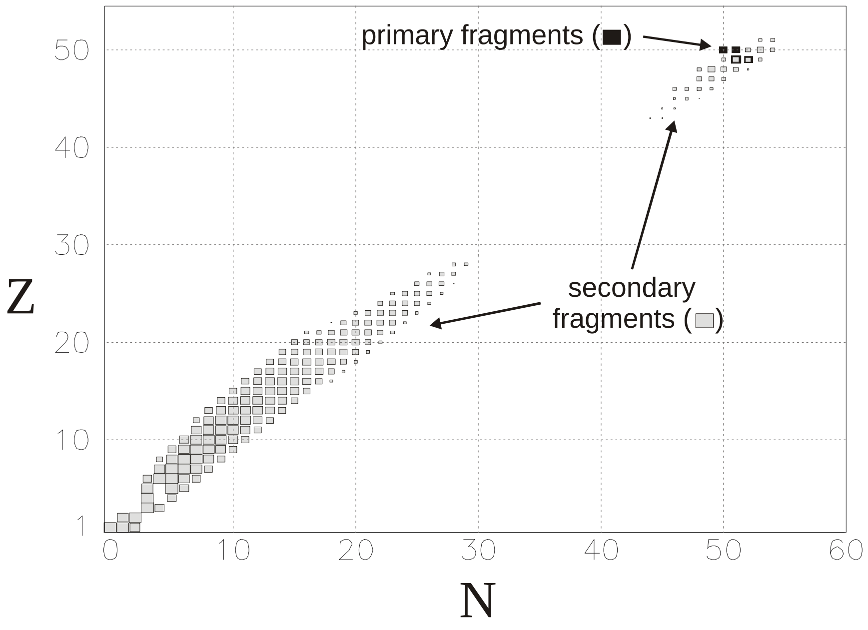

Figure 6.14: Separation performance of the two-degrader method compared with one-degrader setup. The example shows the separation of ^{100}Sn produced via fragmentation of ^{124}Xe at 1000 MeV/u. The large number of secondary fragments for a single degrader stage is illustrated by using the main separator only (light gray boxes). The total amount of the secondary fragments exceeds the separated ^{100}Sn rate by 10^4. In case the pre-separator is used in addition, only the few primary fragments are transported to the final focal plane (black boxes) [54].

6.5 Comparison of the Super-FRS and the FRS for the 1-st order achromatic mode

The gain of the Super-FRS in transmission for uranium fission products is demonstrated in Fig. 6.16 where a comparison between the FRS and future facility is presented as a function of the element number of the fragments. In this example the mass-to-charge ratio was selected to be 2.6. The incident energies of ^{238}U projectiles are 1000 MeV/u and 1500 MeV/u corresponding to the $B\rho_{max}$ of the FRS and the Super-FRS, respectively. In both cases a 3.5 g/cm^2 carbon target was selected to be close to optimum target thickness for all fragments since for energy range 1000 - 1500 MeV/u it is slightly energy dependent. The gain in transmission compared to the FRS is not limited to the fission fragments only, but valid in general, for all exotic nuclei which are far in A and Z from the projectile beams, i.e. for projectile fragments which are accepted by the FRS by only a few percent.[57].

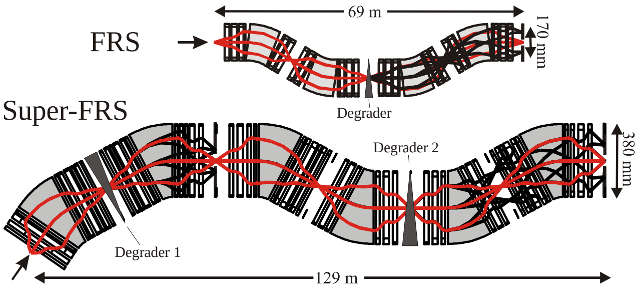

Figure 6.15: Comparison of the layout of the FRS and Super - FRS. The ion-optical plot represents a projection onto the dipersive plane for the sake of clarity the transverse and longitudinal dimensions are not drown in the same scale [54].

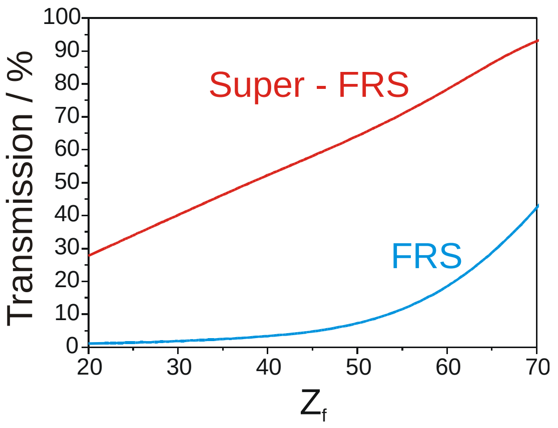

Figure 6.16: Comparison of transmission through the Super - FRS and the FRS for uranium fission fragments (A/Z=2.6). The incident energy of the uranium projectiles was 1000 MeV/u for the FRS and 1500 MeV/u for the Super - FRS. The production target consisted of 3.5 g/cm^2 carbon for both cases. The gain in transmission with the planned Super - FRS in the region of ^{78}Ni is about a factor of 30 [54].

6.6 Flexibility of the Super-FRS

The separator can be operated very flexible since each magnet will be powered independently. Some examples will be given in the following sections.

6.6.1 Spectrometer mode

If the Super-FRS will be operated is the high resolution energy-loss spectrometer precise measurements of the energy transfers in nuclear reactions become possible [58], [59] independently of the relatively large momentum spread of the incident projectile beam.

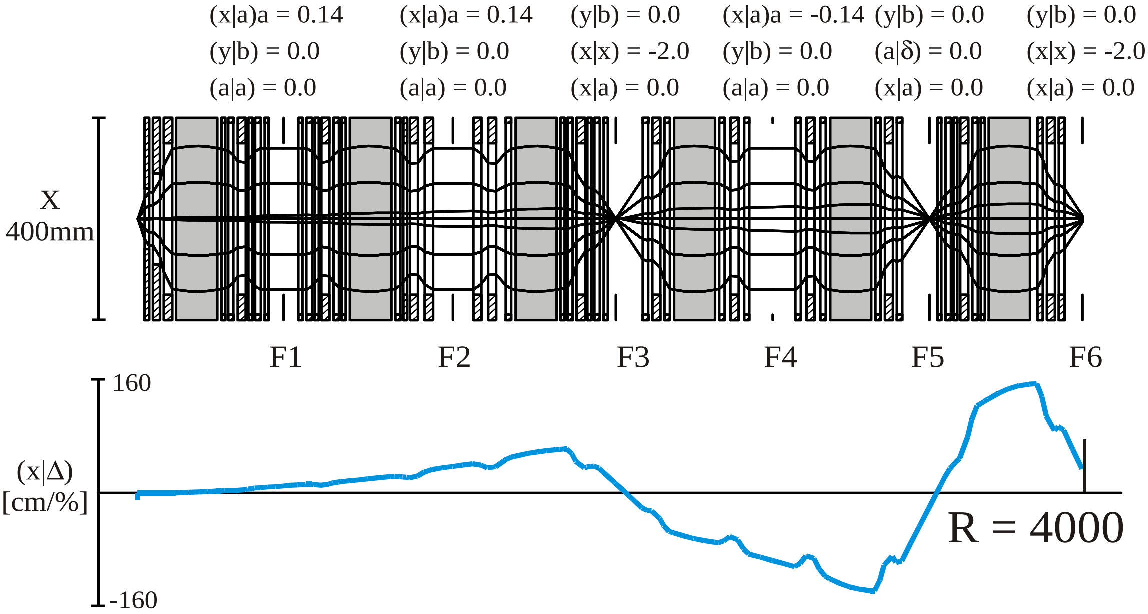

Figure 6.17: Dispersive mode of the Super-FRS. The resolving power of all six dipole stages is added and thus no image is required at the focal planes F1, F2 and F4 bu the beam is parallel here in x-direction. The maximum accepted momentum spread is dp=p = 1%. The beam behavior in y-direction is identical to the standard operational mode. The resolving power of the system at the F6 focal plane is R = 4000:

As an energy loss spectrometer and as the momentum-loss achromat, the magnetic system is always achromatic at the final focal plane. There might be applications, however, where a high resolution is required but not the achromatism. In this case the six dipole stages of the magnet spectrometer are added in resolution. Thus the total momentum resolution can be increased almost by a factor of three. This dispersive mode of the Super-FRS is shown in Fig. 6.17. In the symmetry planes of the pre-separator and the main separator no image condition is required but the beam has to be parallel. For an emittance of 40 ¼ mm mrad and the momentum acceptance of 1% the achievable momentum resolution is 4000 where the illuminated field volume is identical to that of the standard Super-FRS mode operated as a momentum loss achromat.

6.6.2 Low dispersion mode

In order to achieve even a higher transmission for exotic fragments through the Super-FRS the low dispersion mode was developed. This mode is suitable especially to provide a higher transmission for light mass fission fragments, for example rare Ni isotopes. This mode is restricted in the maximum B½ value for the fragment beam, since the quadrupole lenses have to be powered at the limits.

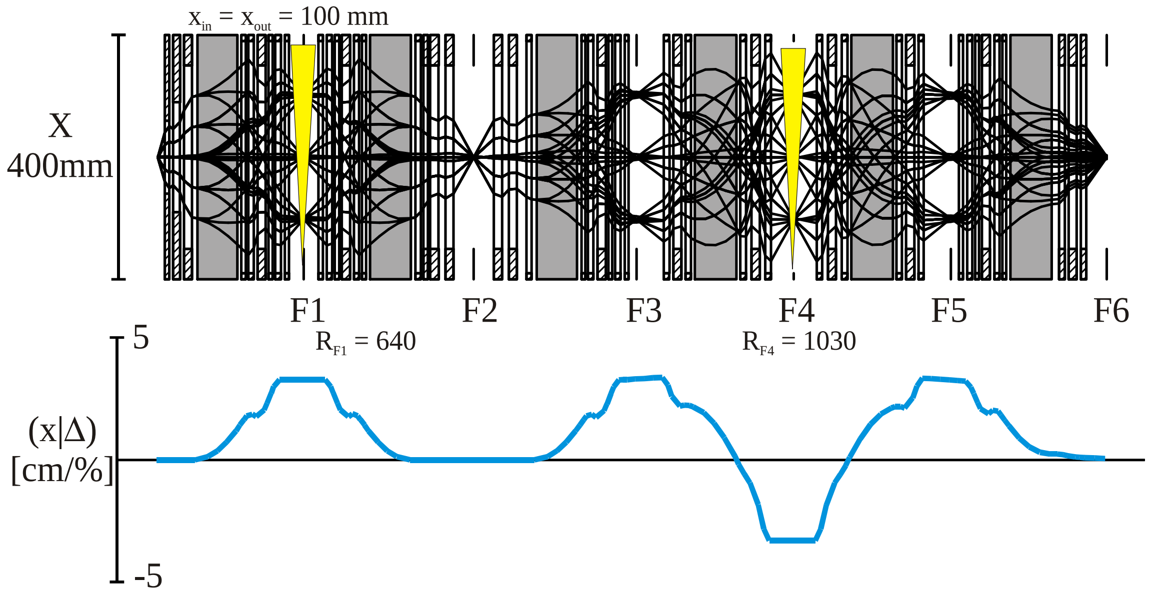

Figure 6.18: The low dispersion mode of the Super-FRS. Beam trajectories and the dispersion curve for 2.5 % momentum deviations are shown in the lattice of the Super-FRS. The trajectories result from an emitance of 40 ¼ mm mrad in x- and y-direction.

The high transmission mode is shown in the Fig. 6.18. The dispersion at the main focal planes F1 and F4 are reduced to 4.03 cm/% and 4.13 cm/%, respectively. This leads the gain factor in transmission for the ^{78}Ni fragment produced by ^{238}U fission of 15%. The two energy degraders at the F2 and F4 focal planes have half the range of the ^{78}Ni in Al. The ion optical properties of the system are listed in Table 6.6.

Matrix elements	at F_1	at F_2	at F_4	at F_6
(xjx)	-3.13	2.00	2.00	2.76
(xja); [m=rad]	0	0	0	0
(xj$\pm_p$); [m]	4.03	0	-4.13	0
(ajx); [rad=m]	0.50	-1.34	-2.28	-1.92
(aj$\pm_p$); [rad]	0	0	0	0
(yjy)	-1.95	2.71	1.86	2.05
(yjb); [m=rad]	0	0	0	0
(bjy); [rad=m]	0.02	0.23	1.00	1.17

Table 6.6 The main ion optical characteristics of the low dispersion mode of the Super-FRS.

6.6.3 Separator-buncher mode

The proposed magnetic system can also be operated in a separator-buncher mode. Such a mode consists of three stages: the pre-separator as an achromatic system, the main separator only up to F5 also operated as an achromatic system and the last dipole stage of the main separator is used as a dispersive stage. This stage could be used for applying an energy bunching technique as will be described in Chapter 6.

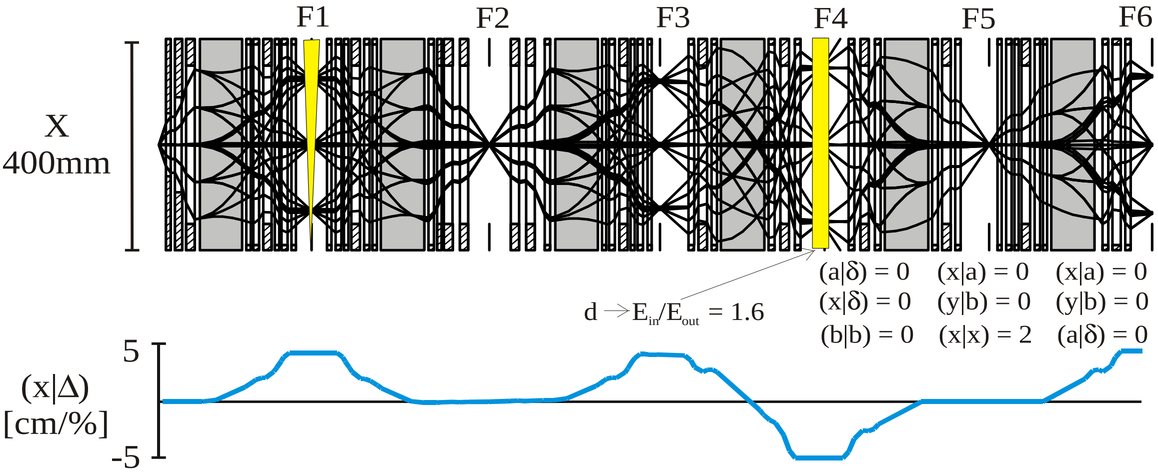

Figure 6.19: The ion optical layout of the Super-FRS operated in the separator-prebuncher mode. The beam trajectories and the dispersion line are drown for an initial beam emittance of 40 ¼ mm mrad in x- and y-direction and for momentum deviation of 2.5 %, respectively.

In order to obtain this optical mode it is necessary to illuminate the first dipoles of the main separator (F2 - F4) about two times less than that of the third one.

This is necessary to keep the field intensity of the quadrupoles within their technical limits. Otherwise, it would be necessary to introduce a homogeneous degrader after the first dipoles in order to reduce the rigidity of the beam.

According to eq. 3.7 following relation must be fulfilled in order to get an achromatic separator

$$M_2 D_1 + D_2 W_v = 0. \tag{6.1}$$

If no degrader is used in the system ($W_v = 1$) M_2 is given by $M_2 = -D_2/D_1 \approx 0.5$, since the illuminated area of the dipoles in the first section (F2-F4) is approximately a factor of 2 larger than this of the second section (F4-F5). If a degrader will be introduced these pure ion-optical coefficients can not change drastically. However, a change of up to $\approx 10\%$ for M_2 and D_2 is acceptable without a significant loss in transmission, thus that W_v can vary between

$$1 < W_v < 1.2. \tag{6.2}$$

The lower limit in this case is given by the fact that always $W_v \approx v_1/v_2 > 1$, since the beam can only be deaccelerated by the degrader.

Using the velocity-energy transformation

$$E = 931.5(\gamma - 1) \ \ \mathrm{MeV/u} \tag{6.3}$$

6.2 corresponds to an energy ratio in front of and behind the degrader of $1.4 < E_1/E_2 < 1.9$ for a uranium beam with an initial energy of about 1500 MeV/u. For the example shown in Fig. 6.19 the thickness of the degrader was chosen to be such that $E_1/E_2 = 1.6$. The ion optical properties of the system are listed in Table 6.7.

Matrix elements	at F_4	at F_5	at F_6
$(x\|x)$	1.6	-2.00	2
$(x\|a)$; [m/rad]	0	0	0
$(x\|\delta_p)$; [m]	-5.82	0	5.18
$(a\|x)$; [rad/m]	-0.69	0.65	-1.03
$(a\|\delta_p)$; [rad]	0	0	0
$(y\|y)$	2.12	-2.97	1.71
$(y\|b)$; [m/rad]	0	0	0
$(b\|y)$; [rad/m]	0.33	-0.33	0.73

Table 6.7. The main ion optical characteristics of the separator-buncher mode of the Super-FRS. The momentum deviation δ_p in parts of the nominal value.

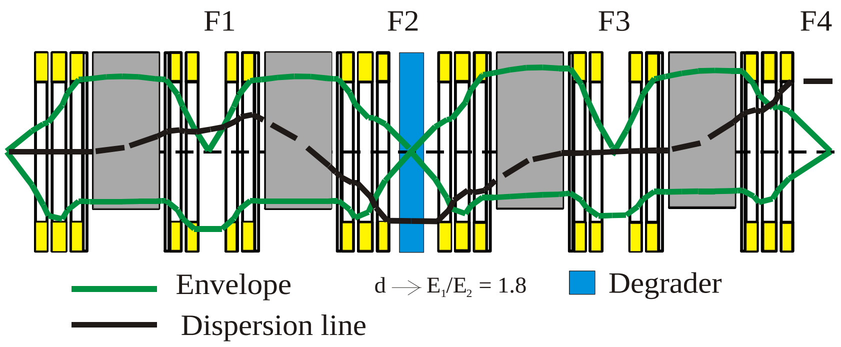

Figure 6.20: The ion optical layout of the FRS operated in F3 achromatic mode. The evelopes and the dipersion line are drown for the initial beam emittance of 13.5 ¼ mm mrad in x- and 22.5 ¼ mm mrad in y-direction and the momentum deviation of 1 %, respectively. The homogeneous degarder placed at F2 focal plane has a thickness corresponding to the energy ratio E_{in}=E_{fin} = 1:8 of the beam in front and behind the degrader

6.6.4 Separator-buncher mode tested at the FRS

According to the premises described in the previous section a new type of optical mode was tested at the present FRS and was verified experimentally. The ion optical design works as follows:

1. The first section from TA to F3 focal plane is run in an achromatic mode
2. The final section, F3 to F4, is used as a dispersive stage

At the horizontal focus of the dispersive stage a monoenergetic shaped degrader could be used for energy bunching.

The ion optical layout of the "F3 achromatic mode" and its imaging conditions are presented in Fig. 6.20. The envelopes and the dispersion line are plotted for 13.5 ¼ mm mrad (x-direction), 22.5 ¼ mm mrad (y-direction) and ¢p=p = 1%, respectively. The target spot size is assumed to be § 1.5 mm in both directions.

In the experiment a ^{238}U beam with an initial energy of E_1 = 750 MeV/u was used. The thickness of the degrader was such, that E_1=E_2 =1.8. The condition of achromatism ($M_2D0_2 + D_2F_2 = 0$, see chapter 3) is well fulfilled (accuracy of $10^{i\,3}$) for the system. These ion optical coefficients are:

M_2	-0.576
$D0_2$	-0.195
D_2	-2.193
F_2	0.0532

A momentum variation to test the selected ion optical condition was performed by using two different targets (Cu, 89mg/cm^2; Al, 158 mg/cm^2). These targets give

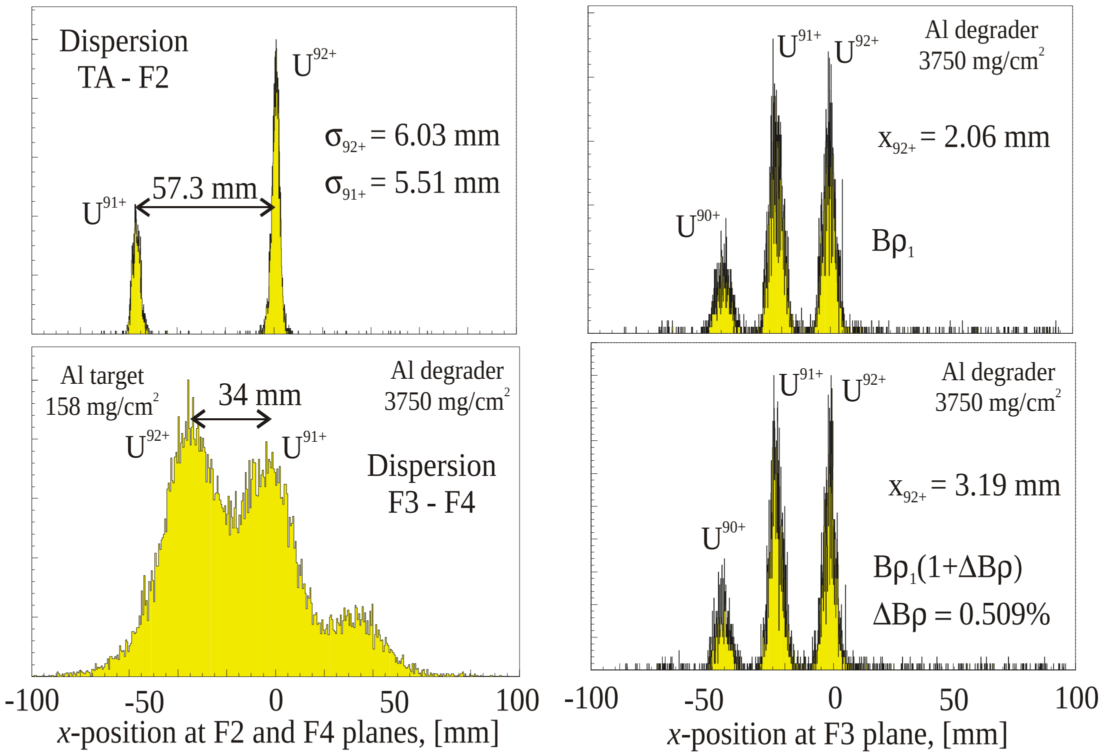

Figure 6.21: The experimental result for the F3-achromatic mode. Left panel: The dispersion measurements at F2 (upper part) and F4 (lower part) focal planes. Right panel: Comparison of the position measurements at the F3 focal planes for the different targets Al 158 mg/cm^2 and Cu 89 mg/cm^2 which provide the difference in magnetic rigidity of the beam of 0.509%.

a difference of 0.509 % in magnetic rigidity for uranium ions. The results of the experiment are shown in Fig. 6.21. The left panel of the figure shows the position spectra of uranium charge states at the F3 focal plane for the two different targets used. The relative shift in the position of the U^{92+} peak is about 1 mm for the 0.509 % difference in magnetic rigidity, which corresponds to the dispersion at F3 focal plane of about 200 mm. This number is almost two orders of magnitude smaller than for the standard mode of the FRS, but still too large for the ideal achromatic mode. This effect is explained by the fact that the degrader thickness was not adjusted according the algorithm described before but only the theoretical value was used.

In the Table 6.8 the main ion-optical parameters of the new mode of FRS are listed.

Matrix elements	at F2	at F3	at F4
(xjx)	0.76	-0.41	-1.69
(xja); [m=rad]	0	0	0
(xj$\pm_p$); [m]	-6.83	0	3.54
(ajx); [rad=m]	0.12	-0.25	-0.05
(aj$\pm_p$); [rad]	0	0	0
(yjy)	-1.41	10.53	-0.11
(yjb); [m=rad]	0	-4.29	0
(bjy); [rad=m]	1.24	0.18	-0.17

Table 6.8. Calculated first-order transfer matrix elements from the target to the focal planes F2 (central focal plane of the FRS), F3 (achromatic focal plane) and F4 (final focal plane) of the FRS. The momentum deviation $\pm_p$ is given in parts of the nominal value.

For the F3 - F4 dispersion measurements two different approaches were applied:

1) Uranium charge states (ch.s.)

2) Energy loss from the MW31 multi-wire proportional chamber (e.l.) (see Chapter 7)

The result obtained in these measurements are shown in the Table 6.9:

	Standard mode	Special Optics	GICO calculation
Dispersion TA - F3	62 mm	205 mm	14.25 mm
Dispersion F3 - F4 (ch. s.)	4390 mm	4210 mm	3825 mm
Dispersion F3 - F4 (e.l.)	3870 mm	3910 mm	
R, F3 - F4	226	249	

Table 6.9. Experimental and calculated results for the dispersion and resolving power of the buncher stage (F3-F4) operated in the F3 achromatic mode.

For the Standard mode the degrader thickness was taken as 3950 mg/cm^2 (experimentally found thickness), for the special optics according the simulations 3750 mg/cm^2 (theoretical number).

From the table it is visible the difference between the TA - F3 dispersions from the Standard mode and Special optics. This fact can be explained that for the Special optics only one adjustment step in degrader tuning was done comparing with the standard mode.

This optical mode can be very useful for the gas cell experiments at the FRS [61].

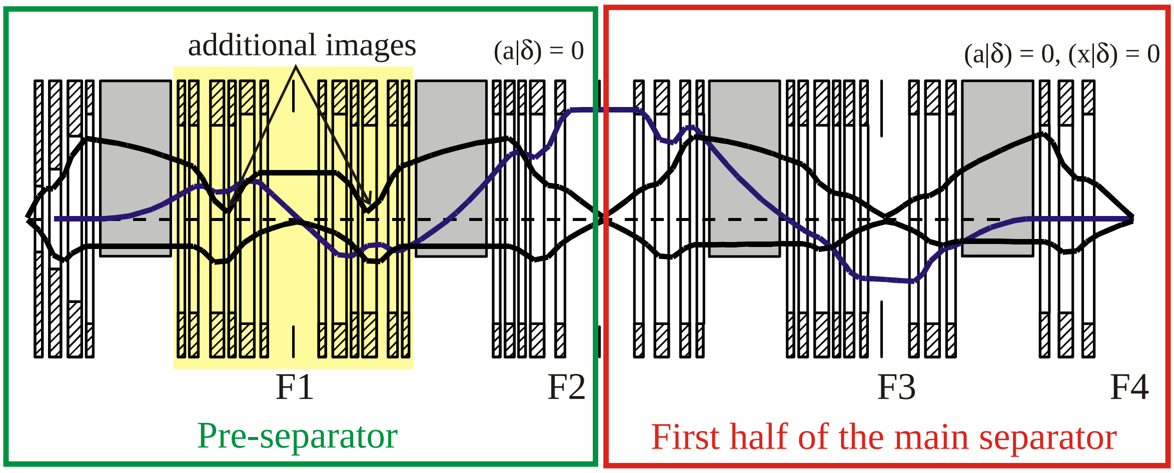

Figure 6.22: The ion optical layout of the dispersive pre-separator mode. The envelops in x and y direction and the dispersion curve are shown for the initial beam emittance of 40 π mm mrad and 2.5% in momentum spread.

6.6.5 Dispersive mode of the pre-separator

In this mode the pre-separator will not be operated as an achromatic system but the resolution of both dipole stages of the pre-separator are added. In general, the simplest and the most flexible way to do this is to add two quadrupole triplets between the dispersive stages so that both optical modes with two or three images between the pre-separator stages are available. However, this solution would lead to a considerable increase of the length of the pre-separator and will cause additional costs. Actually the layout will then be very close to that of the ”vertical” pre-separator. The more simple way to switch between both optical modes is to use the standard layout but to locate two images inside the quadrupole triplets at F1 area. In this case, however, no image profile plane is available at F1.

The ion optical layout of this solution is presented in the Fig. 6.22. Since the magnetic flux density of the quadrupole lenses is limited, the lengths of them and separation drifts are increased slightly, so that the total length of the pre-separator is increased by 0.8 m. The final momentum dispersion is large (about 7.5 cm/%), so that the momentum transmission through the pre-separator in the ”dispersive mode” is lower than in the standard achromatic mode.

Together with the first two dipole stages of the main separator an achromatic system can be achieved as demonstrated in Fig. 6.22. The third and the fourth dipole stages of the main separator could be used as a pre-buncher, similar as described in chapter 6.6.3. The main ion optical characteristics of the dispersive pre-separator mode are listed in Table 6.10.

Matrix elements	at F1	at F2	at F3	at F4
(xjx)	1.73	-2.39	2.81	-2.0
(xja); [m=rad]	-2.12	0	0	0
(xj$\pm_p$); [m]	0	7.45	-4.20	0
(aja)	0	-0.42	0.36	-0.50
(aj$\pm_p$); [rad]	-0.72	0	0.05	0
(yjy)	-3.01	1.95	-2.21	2.11
(yjb); [m=rad]	0	0	0	0
(bjy); [rad=m]	-0.02	-0.01	0.36	-0.44

Table 6.10. Calculated first-order transfer matrix elements from the target to the focal planes F1 (central focal plane of the pre-separator), F2 (dispersive focal plane), F3 (first focal plane of the main separator) and F4 (achromatic focal plane of the main separator) of the FRS. The momentum deviation $\pm_p$ is given in parts of the nominal value.

6.6.6 Defining the direction of separation cuts.

The basic equations that determine mass-, charge- and momentum resolution for a two-stage separator are already given in Chapter 3. Actually their values depend on the way of coupling the both separating stages, which is indicated by the "+" or "-" sign in equations 3.43, 3.44. This will then also have some implications on the separation cuts in the N-Z plane, as it can be read from equation 3.35 and as it is shown in Fig 3.4.

In the case of the Super-FRS the too different ways of coupling the pre- and the main separator can be realized by an additional quadrupole triplet in between the two stages as it indicated in Fig. 6.23.

For the reversed mode, the triplet creates an additional x-image between the pre-separator and the main part, so that the optical conditions at the entrance of the main separator remain unchanged but the mass and charge dispersion is reversed. In case of a standard mode the ion beam is transported through the additional triplet without having the x-image between the pre-separator and this triplet, but there is only one image in x-direction after the triplet. The ion optical coefficients for the

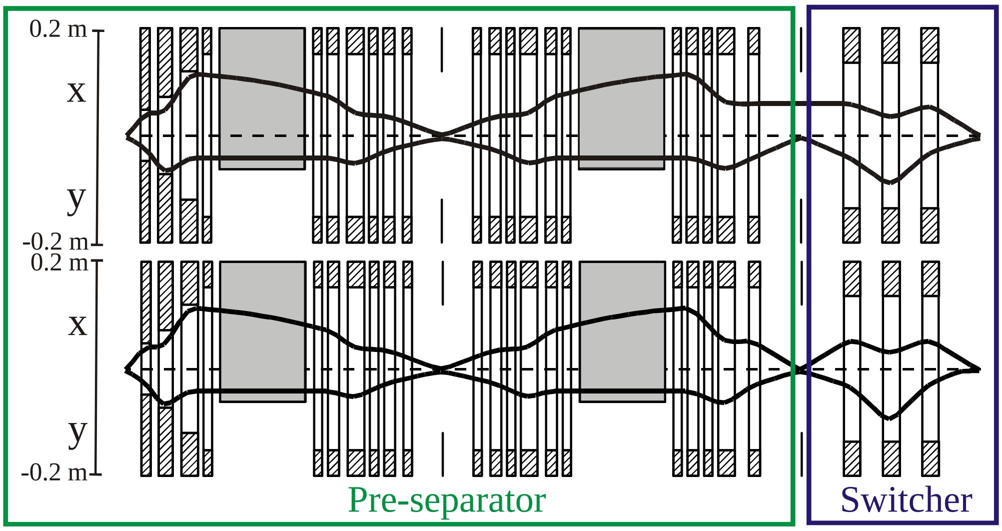

Figure 6.23: Ion optical layout for the pre-separator and the additional quadrupole triplet "switcher" for two modes. Upper part: standard operating mode. Lower part: reversed mode. The envelopes are shown for the initial beam emittance of 40 ¼ mm mrad for x- and y-direction.

focal planes in front and behind the switcher are listed in table 6.11.

Matrix elements	In front of the switcher		Bihind the switcher	
	st. mode	rev. mode	st. mode	rev. mode
(xjx)	5.84	2.0	2.0	-2.0
(xja); [m=rad]	-1.95	0	0	0
(xj$\pm_p$); [m]	0	0	0	0
(ajx); [rad=m]	0.51	0.5	0.5	-0.5
(aj$\pm_p$); [rad]	0	0	0	0
(yjy)	1.8	2.49	-2.38	-3.21
(yjb); [m=rad]	0	0	0	0
(bjy); [rad=m]	-0.52	-0.09	-0.37	-1.13

Table 6.11 The main ion optical characteristics of the pre-separator operated in the standard mode and reversed mode.

The presence of the y-image in front of the triplet improves also slightly the conditions for the beam transport in the vertical direction through the succeeding stages of the main separator. The additionally required space because of the switcher for the presented system is 11.2 m.

The comparison in separation performance are illustrated in Fig. 6.24. MOCADI

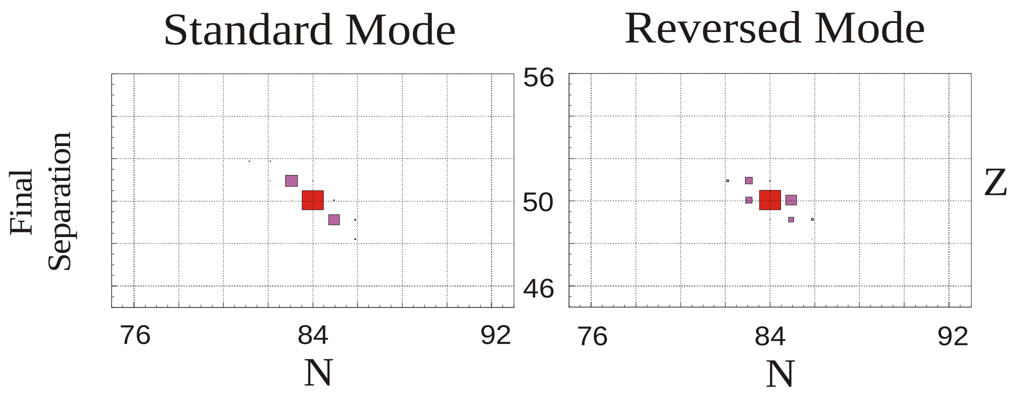

Figure 6.24: Separation performance of the Super-FRS for two operating modes. 134Sn is produced via fission of 238U projectiles. The incident energy of the projectile was 1000 MeV/u. In both cases the Be target of 3 g/cm2 and the same degrader thiknesses (d_1=r_1 = d_2=r_2 = 0:5) were selected.

calculations show the separation quality for the standard and for the reversed mode of coupling the pre- and main separator for ^{134}Sn isotope. A 1000 MeV/u ^{238}U beam is focused onto a 3 g/cm^2 Be target to provide ^{134}Sn ions via fission. The area of the isotopes in N-Z plane represents the corresponding transmissions at the final focal plane of the separator. One can observe that the transmission of the most intensive parasitic isotope ^{134}Sb is smaller in case of the reversed Super-FRS mode.

In principle it is also possible to provide reversed coupling of pre- and main separator if the pre-separator is operated in the dispersive mode (as described in Chapter 6.6.4). However. in this case at least two additional quadrupole triplets are necessary, which can provide 3 intermediate images, which is equal to the reversed mode of adding dispersion. This is necessary since otherwise the large dispersion of 7.5 % will lead to a considerable loss in transmission. Also an additional length of ¼ 25 m for such a system would be necessary.

6.7 Overall facility layout

From the experience gained with the FRS and experimental demands for the next generation facility, the Super-FRS will be equipped with three branches delivering the separated exotic nuclei to different experimental areas (see Fig. 6.25). Each of the three branches - the "High-Energy Branch", the "Ring Branch", and the "Low-Energy Branch" - dedicated to different experimental tasks.

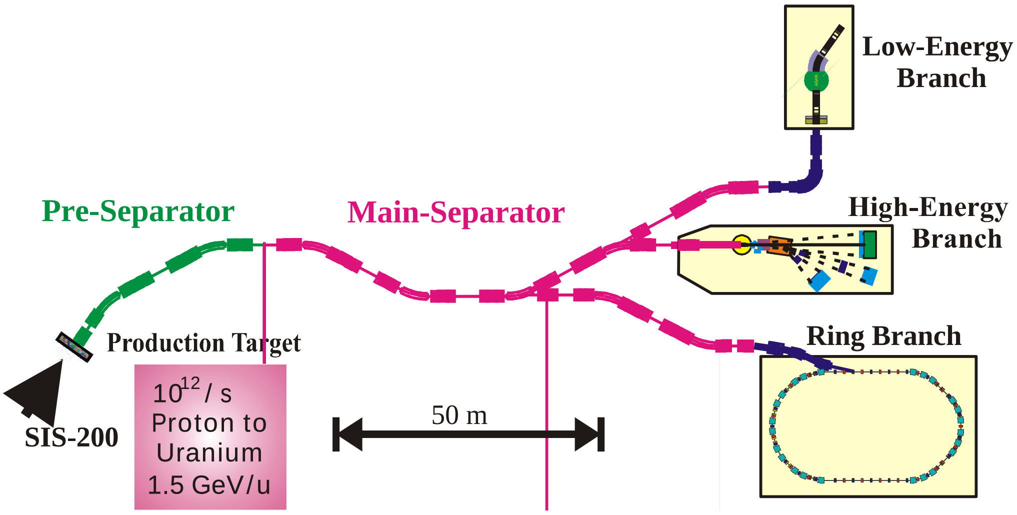

Figure 6.25: Schematic layout of the Super - FRS exotic nuclear beam facility, shown to scale. The three main branches of the experimental areas are indicated.

6.7.1 High energy branch

The high energy cave is directly connected to the exit of the symmetric main separator as described in the previous sections. It allows experiments with fast secondary beams up to $B\rho_{max}$ = 20 Tm and combines the in-flight separator with an efficient reaction setup.

The experiments foreseen in the high-energy branch cover a large variety of different reactions such as elastic scattering, knockout reactions, electromagnetic and nuclear excitations [60].

6.7.2 Ring branch

Of special importance is the Ring Branch which consists of two storage-cooler rings, the Collector Ring and the New Experimental Storage Ring (see also Fig. 1.1 [3]). Fragment pulses as short as 50 ns are injected into the CR with rigidities of up to 13 Tm. Fig. 6.26 shows the ion optical plot for the Ring Branch. The beam is transported through the third dipole of the main separator. An additional quadrupole triplet provides an extra x-image (highlighted part in Fig. 6.26) to keep achromaticity.

The main task of the CR is to efficiently collect and stochastically precool the hot fragments beams, while the NESR is equipped with an electron cooler, a gas target and an eA-collider. Experiments foreseen at the CR and the NESR are precise mass- and life time experiment using the Schottky method [62] and the isochronous mode [63] of the CR, as well as in-ring scattering experiments on internal targets and

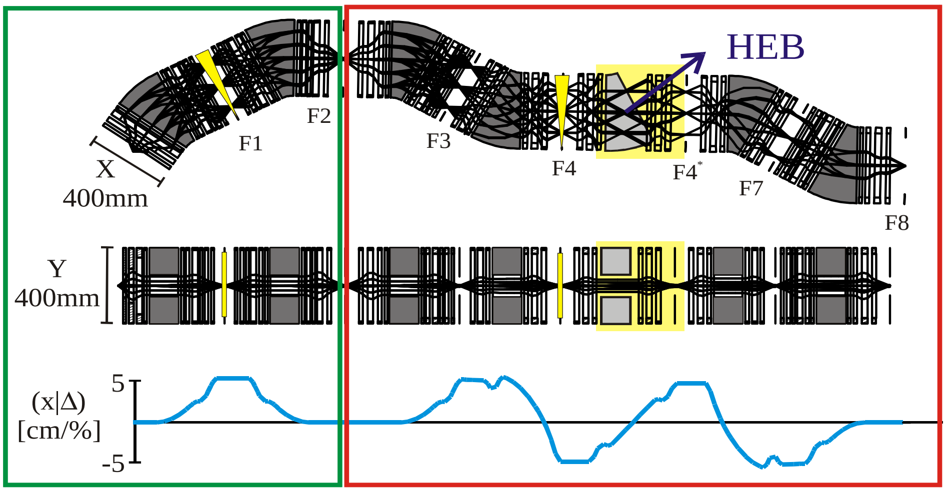

Figure 6.26: The ion optical layout for the Super-FRS ring branch. The system is operated in the same mode as for the High Energy Branch up to F4 focal plane. Then the beam is transported through the third dipole of the main-separator and throug additional quadrupole triplet, which provides an extra imadge in x-direction. The trajectories and the dispersion curve are drawn for the incident beam emittance of 40 ¼ mm mrad in x- and y-direction and for the momentum deviation of 2.5 %.

also electron scattering experiments [64]. The ion optical characteristics of the ring branch are listed in table 6.12

Matrix elements	at F_4	at $F_4^{¤}$	at F_8
(xjx)	1.46	-1.46	-1.60
(xja); [m=rad]	0	0	0
(xj±$_p$); [m]	-4.48	4.48	0
(ajx); [rad=m]	-0.68	0.68	0.66
(aj±$_p$); [rad]	0	0	0
(yjy)	2.84	-2.84	-1.94
(yjb); [m=rad]	0	0	0
(bjy); [rad=m]	-0.36	0.78	1.31

Table 6.12. Calculated first order transfer matrix elements at the focal planes F4 (central focal plane of the main separator), F4¤ (quasimiddle plane of the main separator for the ring branch) and F8 (final focal plane of the ring branch) of the Super-FRS. The momentum deviation in parts of the nominal value.

6.7.3 Low energy branch

The low-energy branch which delivers secondary beams with magnetic rigidities up to 10 Tm, includes a high resolution dispersive separator stage appended to Super-FRS. The ion optical layout for the Low-Energy branch is shown in the Fig. 6.27. The beam goes through the 4-th dipole of the symmetric branch and is then transported to the cave by using an additional set of quadrupoles to keep achromaticity and to provide the needed distance to the cave. The ion optical coefficients for the merging area at F6 and the final focal plane of the low energy branch (F10) are listed in the table 6.13.

With the energy buncher stage the separated fragment beams can be slowed down and their large momentum spread of up to 5% can be reduced to a resulting range straggling close to an ideal monoenergetic beam. After this energy spread reduction absorbers can be used to reduce the fragment energies to Coulomb barrier energies to perform gamma- and particle-spectroscopy [65]. Alternatively, the exotic beams can be stopped and cooled in gas and quickly transferred to ion or atom traps.

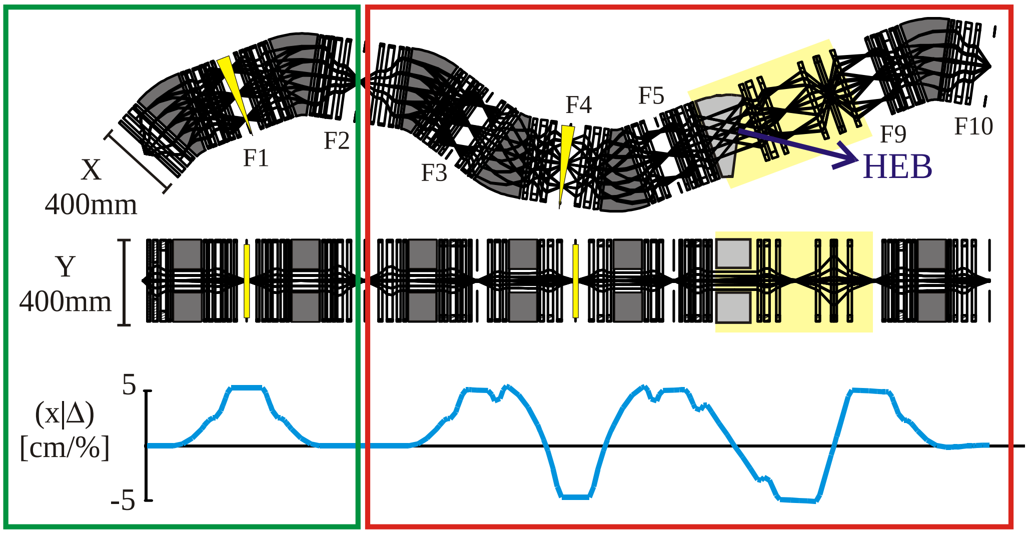

Figure 6.27: The ion optical layout of the Super-FRS Low Energy Branch. The beam is transported through the 4-th dipole of the main-separator and through the additional quadrupole multiplet to provide the needed distance (about 20 m) to the experimental cave. The trajectories and the dispersion curve are drawn for the incident beam emittance of 40 π mm mrad in x- and y-direction and for the momentum deviation of 2.5 %.

Matrix elements	at F6 area	at F10
(xjx)	1.47	1.45
(xja); [m=rad]	-2.6	0
(xj±$_p$); [m]	0	0
(aja)	0	0.69
(aj±$_p$); [rad]	-0.59	0
(yjy)	4.15	2.27
(yjb); [m=rad]	-2.21	0
(bjy); [rad=m]	0.45	-0.33

Table 6.13. The main ion optical characteristics of the low energy branch of the Super-FRS. The coefficients are calculated for the merging area with high energy branch at F6 and for the final focal plane of the low energy branch F10.

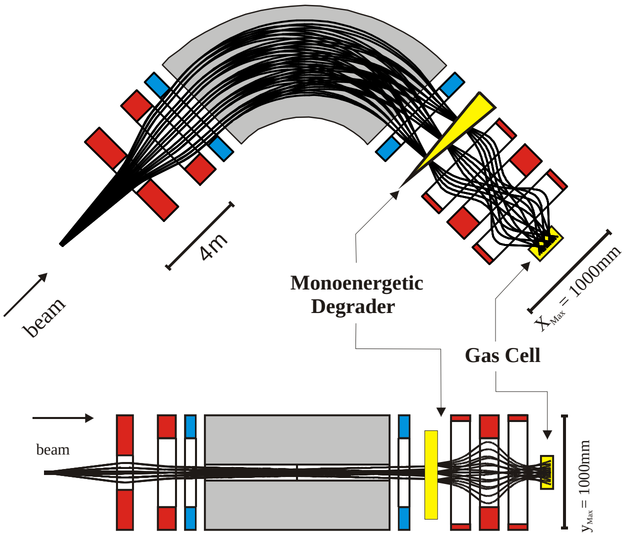

Figure 6.28: Ion optical layout of the energy buncher for the low energy branch of the Super-FRS.

The principle of monoenergetic degrader is shown in the Fig. 6.28. The energy buncher for the Super-FRS consists of a 90^0 dipole magnet with a radius of curvature of 6.5 m and a set of multipoles in front of and behind the dipole to provide the ion-optical conditions. A beam with a momentum spread ¢p will be spatially separated at the dispersive focal plane of the dipole stage. At this position a monoenergetic degrader is placed, which is shaped such that the beam has an (almost) equally energy distribution at its exit. The magnetic elements of the energy buncher system

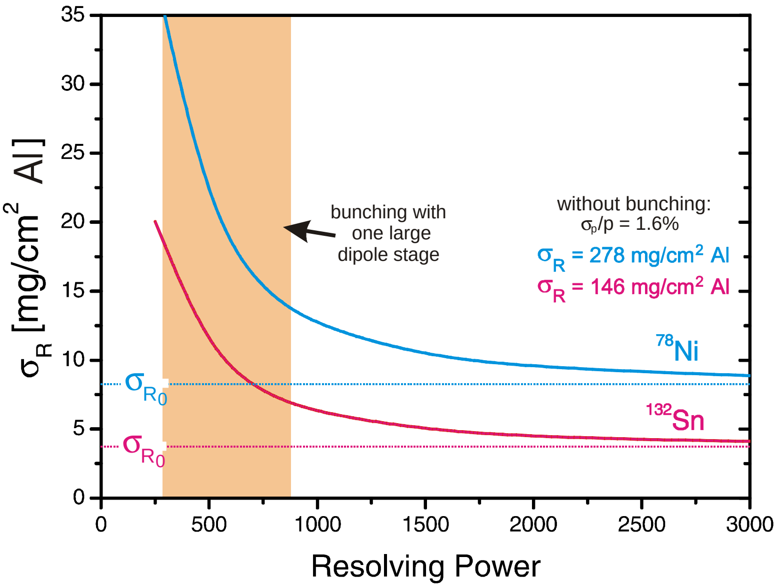

Figure 6.29: The working regime of the 90^0 energy buncher for ^{78}Ni and ^{134}Sn fission fragments with an initial energy of 300 MeV/u.

are listed in Table 6.14. The acceptance of the system is "$_x$ = 15 £ 20 mm mrad and "$_y$ = 10 £ 20 mm mrad. The operating magnetic rigidity is B½ = 10 Tm.

	L / [mm]	2G$_0$ / [mm]	Bmax / [T]
Dipole	ϕ_0 = 900 ρ_0 = 6.5 m	200	1.6
Quad 1 (x)	900	300	0.75
Quad 2 (y)	1000	600	0.65
Hexapole	600	600	0.3
Quad 3 (x)	1000	900	1.6
Quad 4 (y)	1000	600	1.5

Table 6.14. Main characteristics of the energy buncher ion optical elements.

The working regime of the energy buncher is represented in the Fig. 6.29, showing the achievable range bunching for ^{78}Ni and ^{132}Sn fragments with an initial energy of 300 MeV/u. With the expected resolving power of R ' 600:::800 for the energy buncher stage (painted on a Fig. 6.29) the initial range straggling can be reduced from 276 mg/cm^2 to 14 mg/cm^2 for ^{78}Ni and from 145 mg/cm^2 to 6 mg/cm^2 ^{132}Sn. The dashed lines indicate the limit, which would be achieved with initially monoenergetic

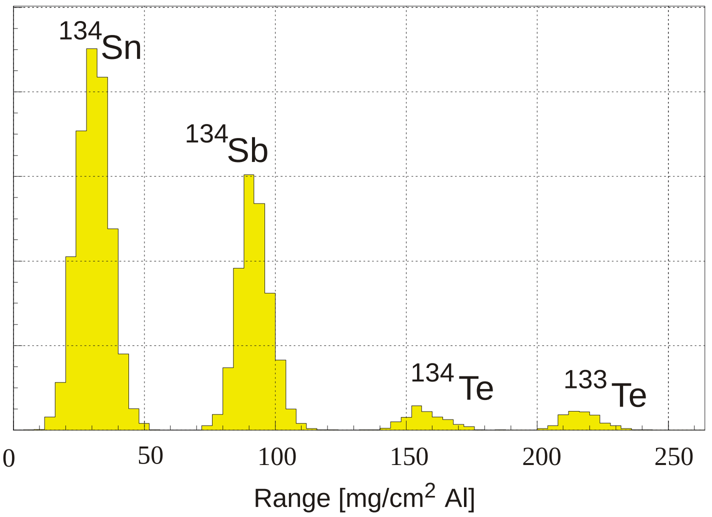

Figure 6.30: The range separation quality of the 90^0 energy buncher for ^{134}Sn fission fragment. All degraders in the system were taken with a thickness of half of the range of the fragment in front of each degrader stage.

beams. The quality of range separation is shown in the Fig 6.30. for the ^{134}Sn fission fragment.

An alternative solution for the energy buncher is presented in Fig. 6.31. It consists of 2×45^0 dipole stages. This solution assumes that the Super-FRS is in one plane but at the -24 m level (like SIS100/200). In this case the energy buncher will in addition transport the beam to the ground level where the experimental areas are installed.

The comparison of the range distribution between the horizontal design and the vertical design of the energy buncher is shown in the Fig. 6.32. As the example the ^{134}Sn fission fragment was chosen. The difference in the resolving power is explained by the different initial beam size at the entrance of the energy buncher. For the vertical design the y-direction is taken as a dispersive one, thus, the resolving power is larger because of the smaller beam size in y-direction.

.

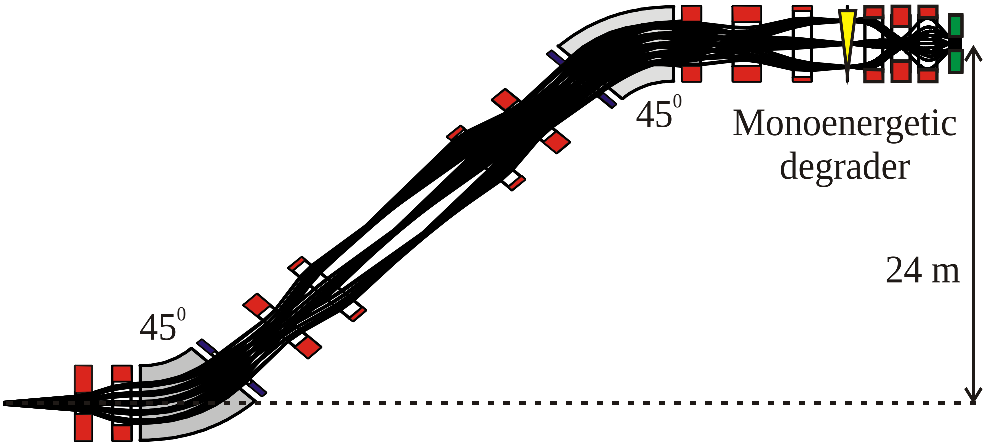

Figure 6.31: The ion-optical layout of the vertical two-stage 45^0 energy buncher.

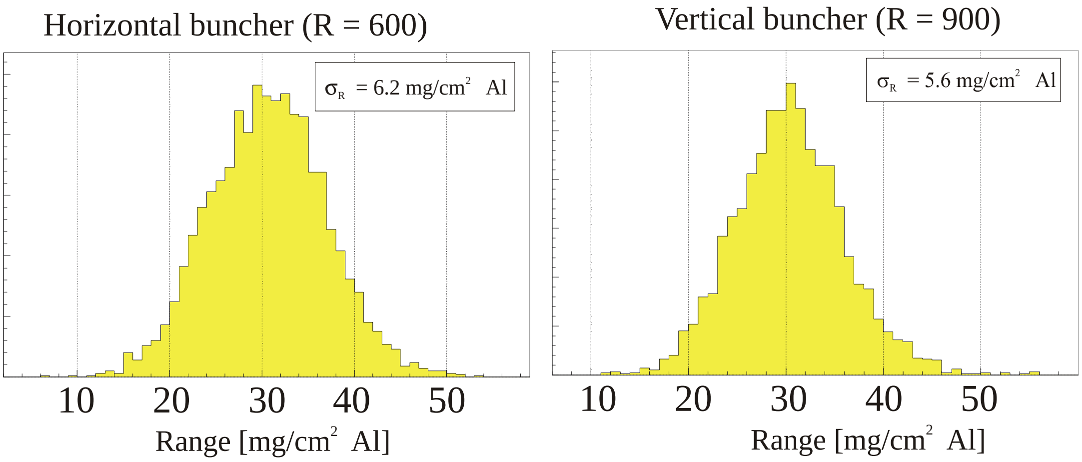

Figure 6.32: The comparison of the range distribution between the horizontal design and the vertical design of the energy buncher.

Chapter 7

Image aberrations and their correction

Trajectories of charged particles relative to an optical axis have been described before in terms of a Gaussian or first order approximation. This description is adequate for narrow particle beams; however, for realistic beams, deviations from this first order theory are observed: aberrations of second, third and higher order.

7.1 High order ion optics

The high formalism of describing ion optical coordinates and system transfer matrices introduced in Chapter 2 can easily be extended to any order. The general particle coordinate vector (Eq. 2.8) at a position z is then given by

$$r_i = \sum_{j=1} (r_i, r_j) r_j^0 + \sum_{j=1} \sum_{k=1} (r_i, r_j r_k) r_j^0 r_k^0 + \sum_{j=1} \sum_{k=1} \sum_{l=1} (r_i, r_j r_k r_l) r_j^0 r_k^0 r_l^0 + \ldots \tag{7.1}$$

with i, j, k, l ranging from 1 to 6 and are representing the coordinates of the vector $\vec{r}$. The elements (r_i, r_j), $(r_i, r_j r_k)$, $(r_i, r_j r_k r_l)$ are the first, second and the third order transfer matrix elements, respectively. For each value of i there are 6×6 elements of the first order, $(6 \times 6)^2$ elements of the second order, $(6 \times 6)^3$ elements of the third order and so on. Fortunately many of these coefficients are zero for realistic cases due to time-independent fields, non accelerating fields, symmetry conditions and so on. A detailed description can be found e.g. in ref. [6].

7.1.1 Classification of aberrations

Image aberrations can in general be divided into geometric and chromatic aberrations.

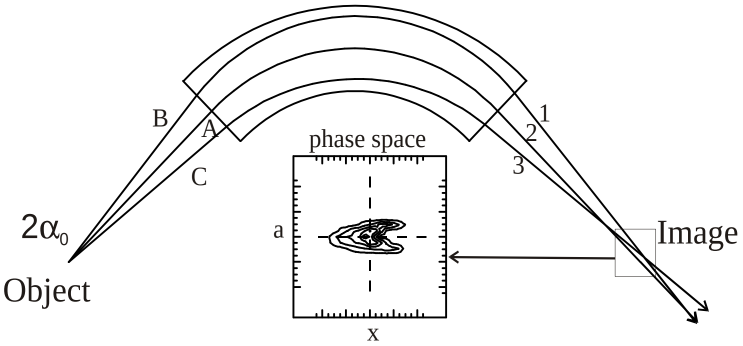

Figure 7.1: $(x|aa)$ aberration caused by a sector magnet. The intersection of path B with path A (point 1) would move further away from the magnet if path B were deflected less, and the creossing of path C with path A (point 3) would come closer to the magnet if path C did not bend so much. To accomplish these aims, path B and C should lie in the field for shorter distances.

If the $r_i; r_j; r_k; r_l; \ldots$ of Eq. 7.1 stand only for the coordinates $x; a; y; b$ the matrix coefficients represent geometric aberrations, which exist for any optical system. Fig. 7.1 shows for example the $(x|aa)$ aberration coefficient produced by the sector magnet with straight entrance and exit field boundaries. For symmetric lenses with a straight optical axis (like e.g. quadrupole) the geometric aberrations might exist only for even orders, because all electromagnetic forces are antisymmetric relative to the x- and y-direction.

If one of the expression $r_i; r_j; r_k; r_l; \ldots$ comprise δ the matrix coefficients represent chromatic aberrations which are only present if the beam contains particles with different magnetic rigidity.

7.1.2 Correction of image aberrations

The presence of image aberrations usually cause problems in real ion-optical systems. They lead to transmission losses and - especially for separator and spectrometer devices - they deteriorate the resolution due to an enlarged (aberrated) image spot size (the first order resolving power defined by eq. 2.32 must be replaced by $R_{tot} = \frac{\langle x|\delta\rangle}{2x_{image}}$, where x_{image} is the real size including all aberrations). Using corrector elements can help to improve the situation. Table 7.1 lists some corrector elements and their effect on aberrations. Since an element of n-th order has also effect on aberrations higher than n-th order, one has to design a system starting from zero-order (deflection), to first order (focusing) and so on.

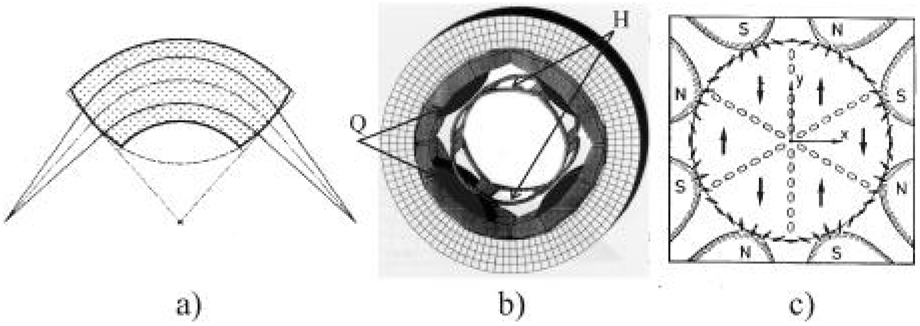
a) b) c)

Figure 7.2: Ways to correct image aberrations: a) a homogeneous sector magnet with shaped field boudaries. b) a quadrupole lense with a superimposed hexapole coil. c) schematic view of a octupole corrector.

Order	Dipole (n = 0)	Quadrupole (n = 1)	Hexapole (n = 2)	Octupole (n = 3)
Zeroth (deflection)	*	0	0	0
First (focusing)	*	*	0	0
Second	*	*	*	0
Third	*	*	*	*

Table 7.1 Effects of multipoles to aberrations of zeroth to third order. The i-th order of aberration is found as the sum of all terms of the i-th row. A term abbreviated by an asterisk indicates that the corresponding $2(n+1)$ -pole element has influence on the aberrations of i-th order and that the corresponding term is nonzero. Zero implies that this multipole element can not change the aberration of the indicated order.

The main practical approach to build corrector elements in ion optical systems is:

1) shaping the entrance/exit field boundaries (mainly used for sector magnets, Fig. 7.2a).

2) using surface coils (in sector magnets) or corrector windings (in quadrupole magnets) where the fields will be superimposed (see Fig. 7.2b).

3) using stand alone correctors (see Fig. 7.2c).

7.2 Aberration correction in the Super-FRS

The positions of the corrector elements in the Super-FRS have been determined by the magnitudes of the corresponding coupling coefficients. Due to the much larger

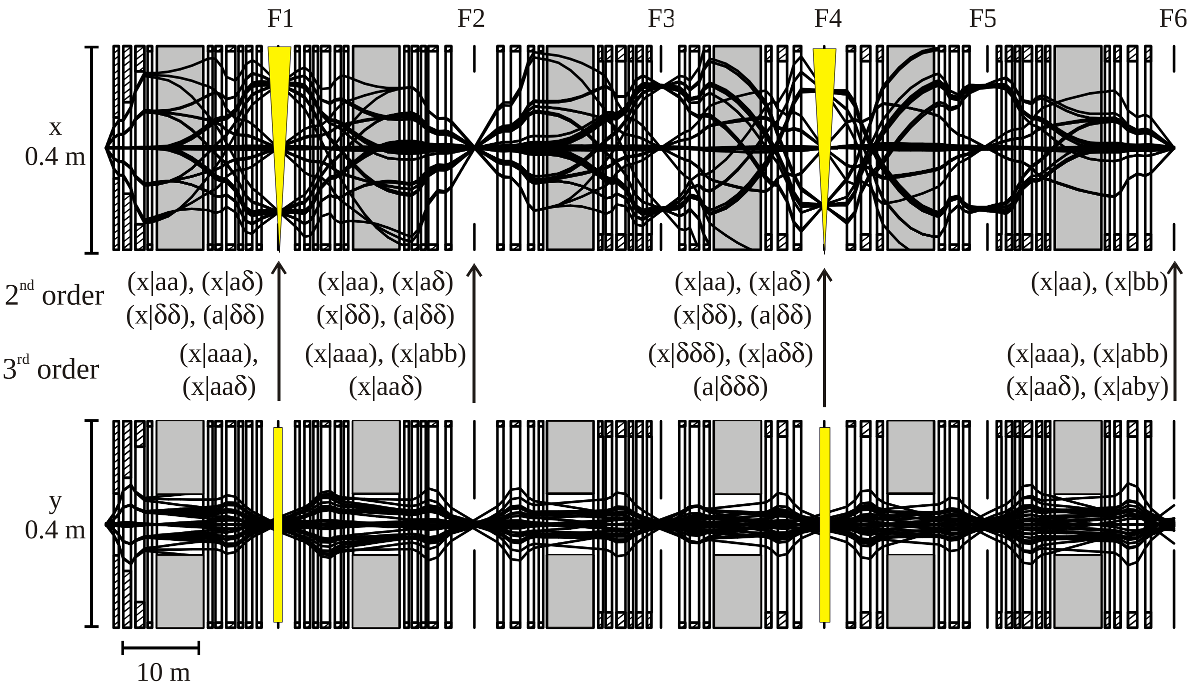

Figure 7.3: The ion optical layout of the Super-FRS (high energy branch) calculated in the third order. The indicated second and the third order transfer matrix coefficients are fitted to be zero.

phase-space acceptance, the optical aberrations in the Super-FRS are much more critical than in the present FRS, where only sextupole correction fields are applied.

2nd order correction scheme

The most considerable 2nd-order aberrations are created by the first stage of the system. In case of no 2nd-order correction, the only important nonvanishing 2nd-order image aberration would be the chromatic aberration (xja±) that is responsible for the tilt of the focal plane at F1and F4 and thus to defocusing of images created by ions with momentum spread. An attempt to correct this aberration with the aid of a hexapole leads to the creation of several other nonvanishing 2nd-order aberrations that also have to be corrected.

In general, it is necessary to provide for correction in the x-direction of four important aberrations: (xjaa), (xja±), (xj±±) and (aj±±). The first two of them are responsible for a beam defocusing at the profile plane F1, and the last two for the position asymmetry of pairs of images created by ions with opposite momentum deviations as well as angular asymmetry of the corresponding pairs of monochromatic beams.

To correct these aberrations four hexapole correctors are needed: one in front of the first dipole magnet, one directly behind it and two others in front and behind the last quadrupole lens in the stage. The first two hexapoles are responsible for the correction of the (xjaa) and (xja±) aberrations and the last two hexapoles for the correction of the (xj±±) and (aj±±) aberrations. To reduce the magnetic flux densities necessary for correction the latter pair of aberrations, the corresponding hexapoles are spatially well separated.

3rd order correction scheme

The third order aberrations in the Super-FRS are relatively small. In the first stage of the system (TA-F1), only two aberrations (xjaaa) and (xjaa±) are to be corrected. This correction can be performed with two octupole correction coils superimposed to the quadrupole lenses surrounding the sector magnet. After this correction is performed in the 2nd stage (F1-F2) only one 3rd order aberration (aj±±±) has to be corrected. This correction is advantageously done with a corrector superimposed with the field of the first quadrupole in the stage. However, with additional weak octupoles superimposed to quadrupole lenses it is possible to eliminate also aberrations (xjaa±) and (xj±±±).

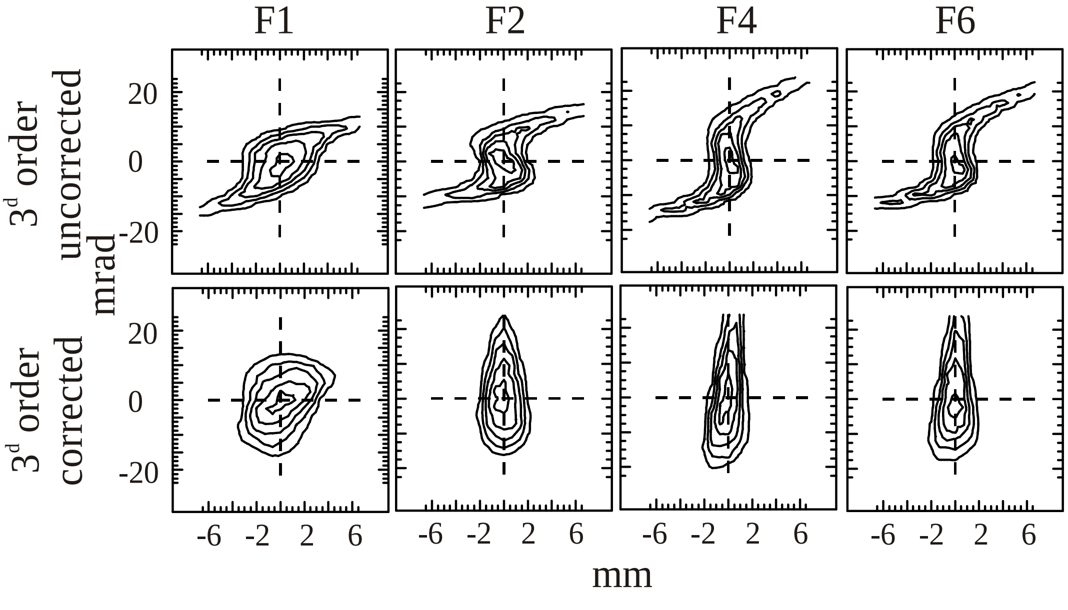

Figure 7.4: The comparison of the beam spot quality for the main focal planes of the Super-FRS calculated in the 3rd order with and without corrections. The second order aberrations are corrected in both cases.

Correction of aberrations in the third stage (F2-F3) of the system can be performed with correctors positioned and excited symmetrically to the correctors in the second stage of the system.

In the 4th stage (F3-F4), two octupole correctors, superimposed to the quadrupole lenses surrounding the dipole magnet, correct the aberrations (xjaaa) and (xjaa±). Besides, it is advantageous to have also octupole correcting coils in the middle quadrupole lens of the last triplet. With this coils the aberrations (xjabb) and (xjaby) are efficiently corrected. This allowed to considerably improve the quality of the beam x-focusing at the final focal plane F6, so that practically no aberrations tails remain in the beam intensity distribution in the x-direction at F6 plane.

The comparison of the beam spot quality with and without 3rd order correctors is shown in the Fig. 7.4 for the main focal planes of the Super-FRS.

7.3 Investigation of the 2nd order aberrations at the FRS

The presented aberration correction scheme for the Super-FRS discussed in the previous sub-chapter is rather complex due to the large angular and momentum acceptance of the device. However, to justify the principle approach the correction scheme was transferred to the FRS and the influence of image aberrations and the possibility to correct them was investigated in an experiment. Since the FRS includes only 2nd order correction elements, i.e. hexapole magnets in front of and behind each dipole magnet, the investigations are restricted to the second order effects. Also the angular acceptance of the FRS is only ' §10 mrad (in x- and y-direction) and the momentum acceptance is only ' §1%. Both values are small compared to the Super-FRS and thus the second order aberrations are mainly restricted to (xja±) and (xjaa).

7.3.1 The experimental setup

During the experiment the FRS was operated in the standard achromatic mode. A uranium beam with an energy of 750 MeV/u was used as a primary beam. A Pb target with a thickness of 2404 mg/cm^2 was used to get two intense charge states of U^{92+} and U^{91+}. Even if there are four hexapole magnets are available in the first two dipole stages upto F2 only the hexapole TS2KS1 and TS2KS3 (see Fig. 7.5) were used in order to simplify and to systemize the correction procedure. All other hexapoles were switched off in the experiment. The beam was monitored using the multiwire proportional chambers MW11,...42 positioned at F1...F4 focal planes (see Fig. 7.5).

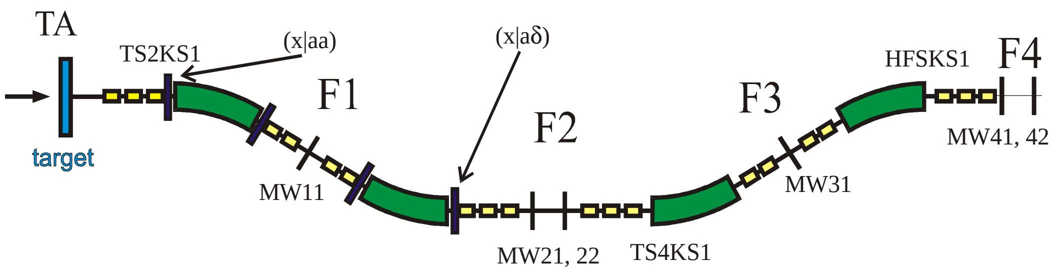

Figure 7.5: Schematic view of the FRS with indicated positions of the used hexapoles and multiwire chambers.

7.3.2 Multiwire proportional chamber

The multiwire proportional chamber (MWPC) developed in the late sixties by Georges Charpak [66], has thereafter been refined and diversified in a large variety of devices exploiting various gas properties and improving on performances. The MWPC allows to achieve high-rate, fully electronic detection and localization of ionizing radiation.

For beam monitoring and for the experiments at the relativistic-heavy ion accelerator SIS/FRS/ESR, this type of wire chamber has been investigated in more detail [67].

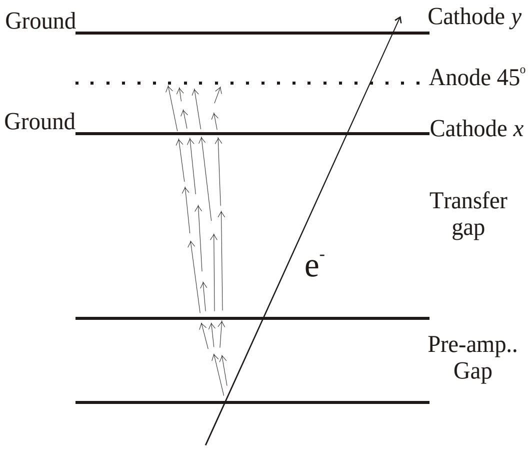

Figure 7.6: Schematic layout of two-stage MWPC

In its basic configuration, the MWPC consists of a set of thin, parallel anode wires stretched between the cathode planes. The schematic layout of a MWPC with a two-stage gas amplification is shown in Fig. 7.6. The wire direction in x and y planes are ortogonal to each other, the wires of anode plane are in diagonal direction. Applying a symmetric potential between anodes and cathodes creates an electric field in the chamber. Electrons released by ionization in the gas drift towards the anodes and experience ionizing collision in the high electric field approaching the thin wires where the field strength goes like $1/r$. The ensuing avalanche multiplication provides a large gain, a factor as large as 10^5 or more (see also Fig. 7.6).

The negative anode signal induces positive signals on the adjacent cathode wires in the x- and y-direction and these signals can be effectively used for the position determination of the incoming ionizing particle. The method which was used to readout the data from MWPC in the experiment is the well-known delay-line technique. Each wire of the planes x and y are connected to a tap of commercially available delay chip. The signal propagates through the left and the right side of the delay line. At the end of delay line the signals are amplified are fed in the STOP of a TDC. The START signal for TDC is derived from the anode. All the anode wires are on one common bus. The time difference between the left and the right side of a delay line gives the position; whereas the sum of left and right should be a constant, namely the total length of the delay line.

7.3.3 Aberration correction scheme and results

The general coordinate vector at the dispersive focal plane F2 of the FRS can be found from the eq.7.1. Taking into account that $(x|a)_{F2} = 0$ (image) and $(a|\delta)_{F2} = 0$ (parallel dispersion curve) it is written up to the second order:

$$x_{F2} = (x|x)x_0 + (x|\delta)\delta_0 + (x|aa)a_0^2 + (x|bb)b_0^2 + (x|a\delta)a_0\delta_0 + \quad (7.2)$$

$$+(x|xa)x_0a_0 + (x|\delta\delta)\delta_0^2 + \ldots \quad (7.3)$$

$$a_{F2} = (a|a)a_0 + 2^{nd} \text{ order terms.} \quad (7.4)$$

For x_{F2} only the most important 2nd order coefficients are taken into account. The general procedure of a 2nd order fit at the FRS is, to minimize the sum of these coefficients by using the four hexapole magnets of the first and the second dipole stage (TS...). This can only be done by the use of ion-optical programs.

The higher order effects in the a-coordinate can be neglected, since each $(a|r_ir_j)$ coefficient is at least a factor 10^2 smaller than $(a|a)$. For the x-coordinate the most important coefficients are $(x|aa)$ and $(x|a\delta)$. Although all other coefficients contribute to the final result (up to 10%) they are neglected in the following in order to get a simlified correction scheme. Thus, eq. 7.2 can be simplified to

$$x_{F2} = (x|x)x_0 + (x|\delta)\delta_0 + (x|aa)a_0^2 + (x|a\delta)a_0\delta_0 \quad (7.5)$$

$$a_{F2} = (a|a)a_0. \quad (7.6)$$

Finally the relationship between x_{S2} and a_{S2} is a second order polynom:

$$x_{F2} = \frac{(x|aa)}{(a|a)^2}a_{F2}^2 + \frac{(x|a\delta)}{(a|a)}\delta_0 a_{F2} + (x|x)x_0 + (x|\delta)\delta_0, \quad (7.7)$$

or

$$x_{F2} = Aa_{F2}^2 + Ba_{F2} + C: \quad (7.8)$$

If all hexapoles are switched off the main contributing 2nd order aberration to the image at F2 is (xja±), created by the initial momentum spread of the beam. It is represented by the slope on the xa-phase space plot as shown in Fig. 7.7

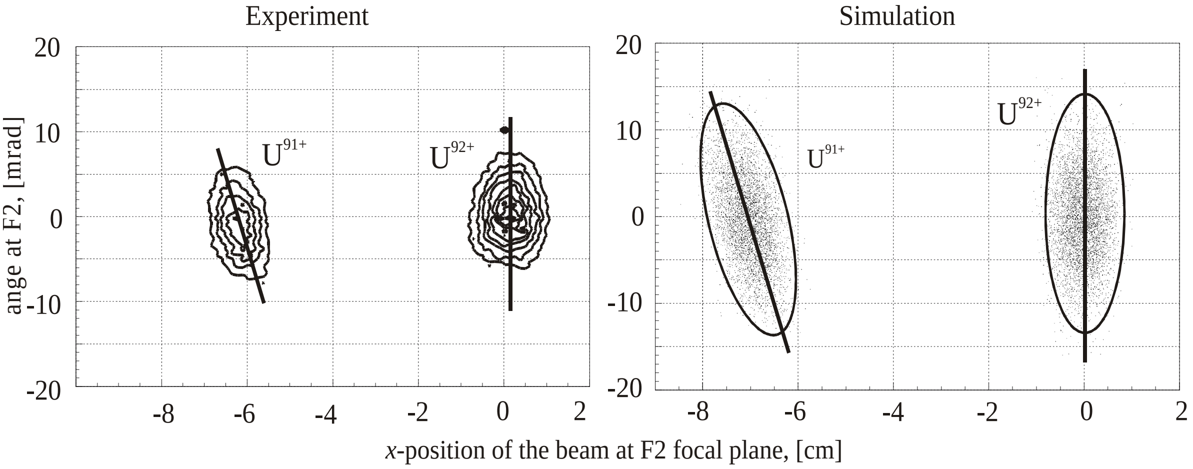

Figure 7.7: The beam phase space at F2 focal plane. All hexapoles are switched off and only one nonzero aberration (xja±) takes place, represented by a slope of uncentered fragment. Left panel: experimental data. Right side: simulation.

The aberration can be corrected by using the hexapole TS2KS3. This hexapole magnet is placed at the most dispersive position and thus, it is the most sensitive hexapole to the (xja±) aberration. However, switching of this hexapole will also introduce the geometrical aberration (xjaa). The effect on the xa-phase space distribution will thus:

1) changing of the inclination of the non-centered fragment slope (responsible is the (xja±) coefficient).

2) changing of the shape of the distribution (responsible is the (xjaa) coefficient).

Fig. 7.8 shows as an example the case, where the hexapole is tuned such, that (xja±) is vanished completely ("upright" fragment shape) and only the (xjaa) aberration remains.

From the xa-phase space distribution the coefficients "A" and "B" (according to the eq. 7.8) were extracted. This was done by fitting a line into the "banana" shaped beam spot connecting the most intensive points (left side of Fig. 7.9). This line gives the second order polynom, from which the coefficients can be extracted (right side of Fig. 7.9).

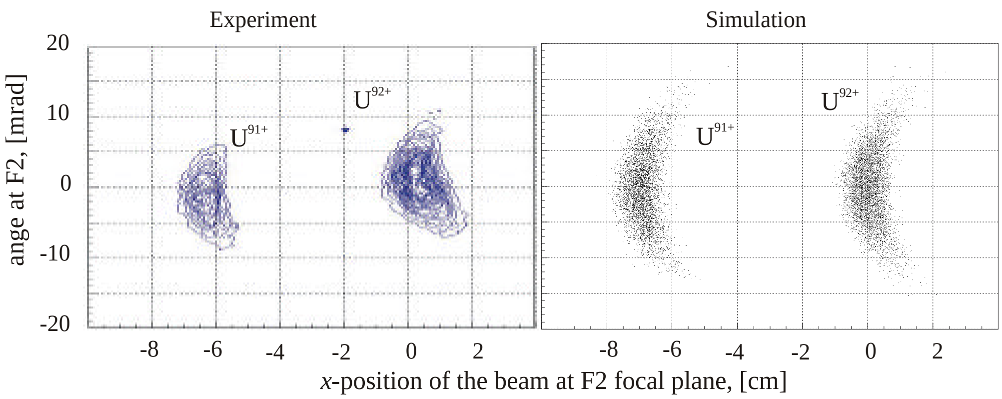

Figure 7.8: xa-phase space plot at the F2 focal plane. Hexapole TS2KS3 is tuned such, that (xja±)=0. The correction of theis aberration introduce at the same time a strong (xjaa) aberration, which is represented by the "banana" shape in the phase space plot.

In Fig. 7.10 the relative deviation of the experimentally determined coefficients A and B compared to simulated one are shown. The coefficient A, which represents the (xjaa) aberration coefficient, stays within an accuracy of approximately 10%. For the coefficient B, which represents the (xja±) coefficient, the accuracy is » 30%. This rather poor value is explained by the fact, that the B coefficient is very sensitive to the position of the peak of the parabola.

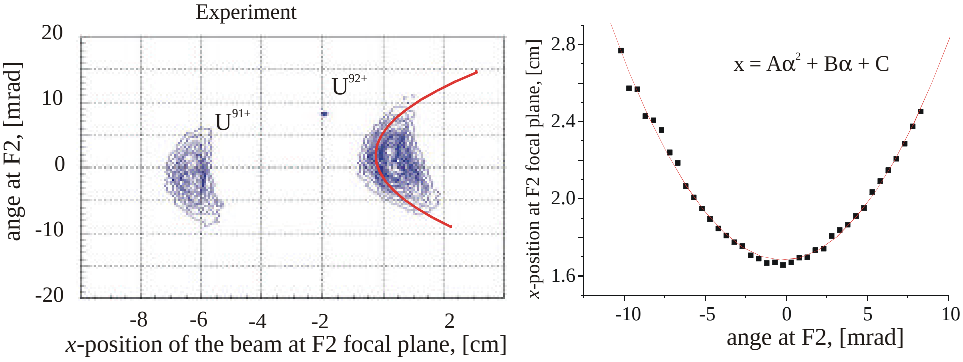

Figure 7.9: Left side: "banana" shaped beam spot size with the corresponding most intensive line for U^{92+} fragment. Right side: fitting of the most intensive line by the second order polinom.

Fig. 7.11 finally shows the xa-phase space plot for the case that both aberrations, (xjaa) as well as (xja±), are corrected by the two hexapole magnets TS2KS1 and

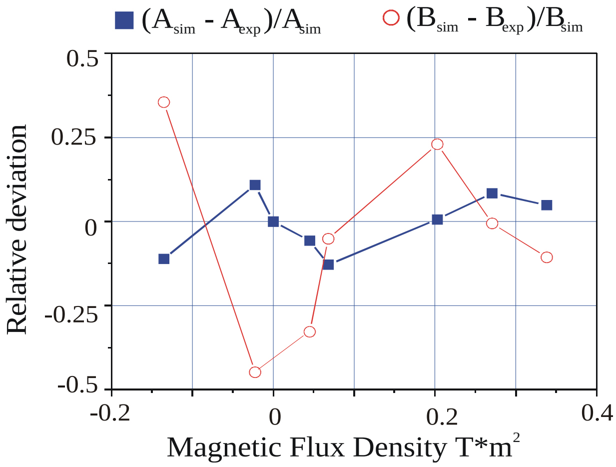

Figure 7.10: Relative deviations for coefficients A and B depending on the magnetic flux density of the TS2KS3 hexapole at F2 focal plane of the FRS.

TS2KS3. In this case only these 2nd order aberrations are present, which were neglected in assumption in the beginning (the most important one of these is the $(x|\delta\delta)$ aberration). The regained resolving power from the first order optics is approximately 15%.

In practice all 4 hexapole magnets of one FRS stage are used and thus also the remaining 2nd order coefficients can be minimized. Table 7.2 lists the most important 2nd order coefficient for the case:

1) all hexapoles are switched off

2) only TS2KS1 and TS2KS3 are used such, that $(x|a\delta)$ and $(x|aa)$ vanish

3) all four hexapole magnets are used such, that the sum of the 2nd order matrix coefficients is minimized.

Coefficient	No hexapoles	TS2KS1 and TS2KS3 are on	4 hexapoles are on
$(x\|aa)$	$5.22\cdot10^{-6}$	$-1.64\cdot10^{-12}$	$-2.45\cdot10^{-5}$
$(x\|a\delta)$	$-4.45\cdot10^{-3}$	$-7.61\cdot10^{-13}$	$-1.94\cdot10^{-6}$
$(x\|\delta\delta)$	$7.11\cdot10^{-4}$	$1.18\cdot10^{-3}$	$1.68\cdot10^{4}$
$(x\|bb)$	$6.52\cdot10^{-5}$	$1.52\cdot10^{-3}$	$-5.25\cdot10^{-5}$
$(x\|xa)$	$1.36\cdot10^{-7}$	$-1.74\cdot10^{-4}$	$-1.52\cdot10^{-4}$

Table 7.2. The most important second order coefficients which have to be minimized in order to not destroy the beam spot quality.

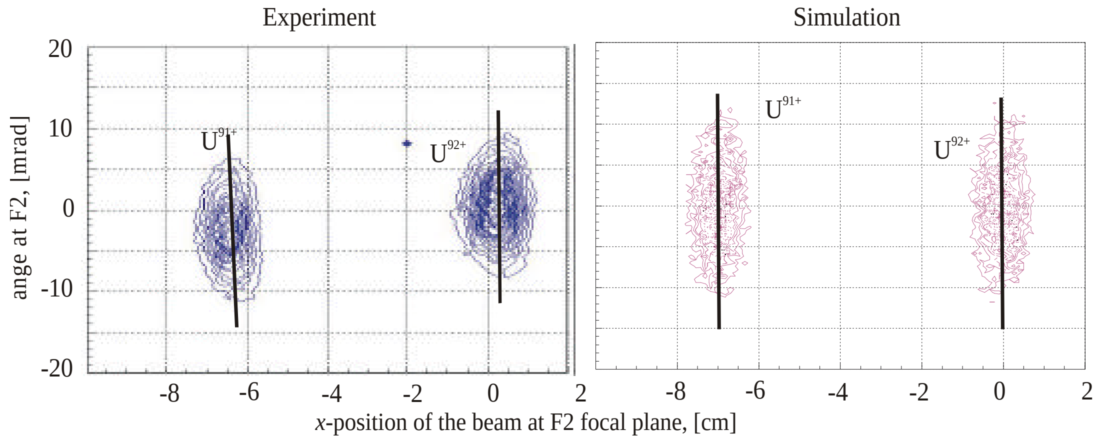

Figure 7.11: xa-phase space plot at F2. The hexapole magnets TS2KS3 and TS2KS1 are tuned such, that (xja±) as well as (xjaa) are corrected. The image size is ¾$_{x}$ = 4:6 mm, and thus the regained resolving power from the first order optics is approximately 15%.

Chapter 8

Outlook

Projects that use exotic nuclear beams have gained much interest due to the vast amount of research and applications, as well as the success at the present facilities. Both ISOL and in-flight facilities have contributed a lot to nuclear and atomic physics as well as nuclear astrophysics. It was clearly demonstrated that in the future both types of facilities will provide complementary contributions based on next-generation developments. This fruitful complementary is realized on many frontiers, for example, in the field of precision experiments with stored exotic nuclei in traps end high-energy storage rings.[68] The next-generation facilities will consist of ISOL and in-flights methods or hybrids of both. In the hybrid scheme, spatially separated nuclear beams from an in-flight facility are stopped in a gas or liquid medium, followed by fast extraction and post-acceleration, thus taking advantage of both ISOL and in-flight methods. Presently many aspects of this scheme are under investigation at several laboratories including GSI. The proposed RIA facility in the USA plans to use this hybrid scenario in combination with a post-accelerator [69].

The in-flight separation method based on high-energy projectile fragmentation and fission is universal and provides all nuclei and elements up to the heaviest projectiles. High energies up to 1500 MeV/u are the basic prerequisite for completely ionized fragments. they allow to do precise reaction studies such as scattering experiments with electrons, as well as with light target nuclei to investigate nuclear structure using inverse kinematic methods. A spacial challenge in this context is the coupling of a high-energy in-flight separator with a storage-cooler ring as proposed with the Super-FRS facility and the RI-factory in RIKEN [70].

Fig. 8.1 compares the rate of ^{132}Sn achievable at RIA, RIKEN and the Super-FRS. ^{132}Sn is produced via ^{238}U fission. The maximum primary beam energy is restricted to 350 MeV/u at RIKEN (using cyclotron) and 400 MeV/u at RIA (using a LINER accelerator), while at GSI the whole energy range up to 1500 MeV/u is accessible. In this study the ion-optical properties of the Super-FRS are applied in the full energy range. A result of this comparison is that the rates of fission fragments of all three

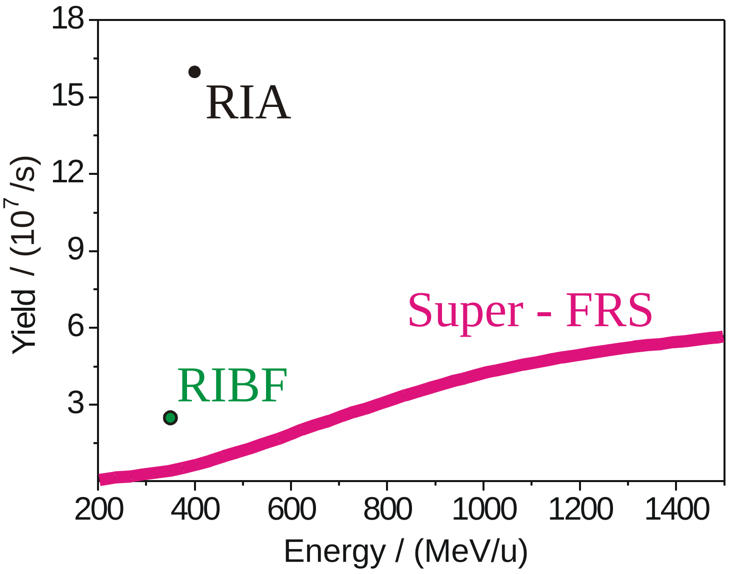

Figure 8.1: Rates for ^{132}Sn fission fragments produced with a primary beam of ^{238}U at different incident energies in a carbon target. The primary beam energy is restricted to 350 MeV/u at RIKEN and 400 MeV/u at RIA [54].

facilities are quite similar although the primary uranium beam intensities differ by more than one order of magnitude. For low energy experiments the RIA project will use fission fragments via the ISOL method.

Bibliography

[1] R.Bennett et. al., NuPECC, Nuclear Physics European Collaboration Committee (2000).

[2] H.Geissel, G.Muenzenberg, Annu. Rev. Nucl. Part. Sci. (1995) 163-203.

[3] An International Accelerator Facility for Beams of Ions and Antiprotons, Conceptial Design Report, GSI (2001).

[4] R.Schneider et. al., Z. Phys. A348 (1994) 241.

[5] C.Engelmann et. al., Z. Phys. A352 (1995) 351.

[6] H.Wollnik, Optics of the charged particles.

[7] D.C.Carey, The Optics of Charged Particles Beams. London: Harwood (1987).

[8] I.Chavet, Nucl. Instr. Meth., Vol.45 (1966) 340.

[9] H.Ewald, H.Hintenberger, Methoden und Anwendungen der Massenspektroskopie, Weinheim: Verlag Chemie, 1953.

[10] E.D.Courant, H.S.Snyder, Ann. Phys.-1958.-Vol.3.-P.48.

[11] A.W.Chao, J. Appl. Phys. 50 (1979).

[12] K.L.Brown, D.C.Carey, and Ch.Iselin, Geneva, CERN Report 80-04 (1980).

[13] S.Kowalski, H.Enge, Proc. Int. Conf. Magnet. Technol. (Brookhaven), (1972) P.181.

[14] H.Geissel, et. al., Nucl. Instr. Meth., B70 (1992) 286-297.

[15] K.-H.Schmidt et al., Nucl. Instr. Meth., A260 (1987) 287.

[16] H.Geissel et. al., Nucl. Instr. Meth., A282-247 (1985).

[17] T.Shimoda et.al., Nucl. Instr. Meth., B70 (1992) 320.

[18] H.Geissel et. al., A Proposal for the SIS-ESR Experimental Programm, GSI, (1987).

[19] J.Lindhard, A.H.Sorensen, Phys. Rev. A53 (1996) 2443.

[20] Th.Schwab, PhD thesis, University Giessen GSI Report 91-10 (1991).

[21] H.L.Ravn et al., Treatise on Heavy-Ion Science, ed. Bromley DA. New-York: Plenum Press (1989) 8-363.

[22] H.L.Ravn et al., Nucl. Instr. and Meth. B88 (1994) 441.

[23] W.L.Talbert, Nucl. Instr. and Meth. B26 (1987).

[24] M.Fujioka et al.(Edts.), Nucl. Instr. and Meth. B70 (1992).

[25] D.Forkel-Wirth, G.Bollen (Edts), ISOLDE - a laboratory portrait, Hyp. Int. 129 (2000).

[26] A.Magel et.al., Nucl. Instr. and Meth. B94, (1994) 548-554.

[27] S.Kox et al., Phis. Lett. 159B (1985) 15.

[28] D.L.Olson et al., Phys. Rev. C24 (1981) 1529.

[29] B.L.Berman, At. Data and Nucl. Data Tables 15 (1975) 319.

[30] A.S.Goldhaber, Phys. Lett. B53 (1974) 306.

[31] D.J. Morrissey, Phis. Rev. C39 (1989) 460.

[32] J.Huefner, Phys. Reports 125 (1985) no.4, and references therein.

[33] C.Wagemans, ed., The Nuclear Fission Process, CRC Press, London, 1991.

[34] H.Geissel, GSI report GSI-93-42 (1993)

[35] U.E.Viola et al., Phys. Rev. C31, (1985) 1550.

[36] D.J.Hinde et. al., Phys. Rev. C45 (1992) 1229.

[37] K.Suemmerer et.al., Phys. Rev. C42 (1990) 2546.

[38] C.A.Bertulani, G.Baur, Phys. Rep. (1988) 163-299.

[39] P.Armbruster, et al., Z. Phys. A (1995).

[40] R.Silberberg, et al., Astrophys. J. Suppl. Ser. (1973) 25-315; (1973) 25-335; (1985) 58-873.

[41] Brosa-Formel, Nucl. Phys. A505 (1989) 423C, 190402 HWE.

[42] William R.Leo, Techniques for Nuclear and Particle Physics Experiment (1984) 26.

[43] The GLOBAL programm is available via anonymous ftp from borsu8.in2p3.fr in the directory /pub/nex/global/pc and /pub/nex/global/vms_unix for PCs and workstations, respectively.

[44] M.Wilson, Superconducting Magnets for Accelerators, GSI, 2001.

[45] H.-D.Betz, Rev. Mod. Phys. 44 (1972) 465.

[46] GSI Accelerator home page: http://www.gsi.de/accelerator/sis.p15.html

[47] G.Li, et al., Rev. Sci. Instr. 71(2), 376, 2000.

[48] M.Winkler, et al. Nucl. Instr. Meth. A334, 455, 1994.

[49] H.Wollnik, B.Hartmann and M.Berz, AIP Conference Proceedings; ed. C.Eminhizer, 177 (1988) 74-85.

[50] M.Berz, Nucl. Instr. Meth., A298 (1990) 473.

[51] H.Wollnik, J.Brezina, M.Berz, Nucl. Instr. Meth., A258 (1987) 408.

[52] B.Franczak, Proc. of the Europhysics Conference on Computing in Accelerator Design and Operation, Berlin (1983).

[53] Th.Schwab, Doctoral Thesis, GSI Report GSI 91-10, Darmstadt (1991).

[54] H.Geissel, et al., Nucl. Instr. Meth., B204 (2003) 71.

[55] A.Zeller et. al., IEEE Trans. Appl. Supercond. 11 (2001) 1725.

[56] A.Zeller et. al., Advances in Cryogenic Engineering, 43 (1998) 245.

[57] H.Geissel et. al. GSI report GSI-2002-23 (2002)

[58] C.Schaerf et al., Nucl. Instr. Meth. 30 (1964) 359.

[59] E.Grorud et al., Rapport LNS/029 (1979).

[60] http://www-land.gsi.de/r3b/docu/rep02-www.pdf

[61] G.Savard et. al., Nucl. Instr. Meth.,V 204 (2002) 582-586.

[62] U.Schaaf, GSI-Report, GSI-91-22 (1991).

[63] M.Hausmann et. al., Nucl. Instr. Meth. A446 (2000) 569-580.

[64] P.Egelhof et.al., STORI02 Conference Prosidings, Uppsala, Sweden, 2002.

[65] AGATA - Technical Proposal, ed. J.Gerl, W.Korten, GSI, 2001.

[66] A.Breskin, G.Charpak et.al., Nucl. Instr. Meth. 161 (1979) 19.

[67] H.Stelzer, Nucl. Instr. Meth. A310, (1991) 103-106.

[68] H. Geissel at. al. Nucl. Instr. and Meth. B126, (1997) 351.

[69] Rare Isotope Accelerator RIA, http://www.nscl.msu.edu/future/ria/index.html, http://www.phy.anl.gov/ria

[70] RIKEN Radioactive Isotope Factory T.Katayama et al., Design Report November 2000, http:/www.rarf.riken.go.jp/ribf/index.html

Acknowledgements

Here I would like to express my gratitude to all those people who contributed to the completion of this work:

Prof. Dr. Hans Geissel for kindly offering me the possibility to work in the fragment separator group at GSI and for willingly and patiently sharing his knowledge and experience.

Here I would like to thank my diploma supervisor, Prof. Dr. A. Kalimov from the S-Petersburg state Technical University for his availability and friendly encouragement.

Dr. Helmut Weick for his efforts helping me and for being a most agreeable company during every experiment.

For the direct supervising of my work I would like to express my very special thanks to Dr. Martin Winkler.

Prof. M. Yavor who has largely contributed to my deeper understanding of ion optics and has been following closely my work. His help as well as his suggestions were crucial to the development of my work.

Thanks to the people who made my life in GSI so enjoyable and helped and encouraged me during all this time:
Yuri, Tania, Sergey, Mauricio, Milan, Günter, Mitya, Enrique, Jens, Torsten.

I'm very thankful to all 'Makarasch' football team.

Specially I would like to thank Michael (Mike) Maier for taking care about my life in Germany from a certain point of view.

I'm grateful to my parents for their love and constant care and for all that I am now.